

La borsa di dottorato è stata cofinanziata con risorse del  
Programma Operativo Nazionale Ricerca e Innovazione 2014-2020 (CCI 2014IT16M2OP005),  
Fondo Sociale Europeo, Azione I.1 "Dottorati Innovativi con caratterizzazione Industriale"



UNIONE EUROPEA  
Fondo Sociale Europeo



## UNIVERSITY OF MESSINA DEPARTMENT OF ENGINEERING

**PhD Course in Engineering and Chemistry of Materials and  
Constructions**

**XXXIII Cycle**

---

**SSD: ING-IND/14  
Mechanical Design and Machine Construction**

*Design and development of a Continuously Variable Transmission  
(CVT) for high efficiency and low weight heavy duty applications*

**PhD Student:**

*Danilo D'ANDREA*

**Tutor:**

*Prof.ssa Gabriella EPASTO*

---

Academic Year 2020





## TABLE OF CONTENTS

<b>Hydro-Mechanical CVT Power Split .....</b>	<b>12</b>
<b>1.1 Definition.....</b>	<b>12</b>
<b>1.2 Different Design Layout .....</b>	<b>13</b>
<b>1.2.1 Input Coupled.....</b>	<b>13</b>
<b>1.2.2 Output Coupled.....</b>	<b>14</b>
<b>1.2.3 Compound Coupled Transmission .....</b>	<b>15</b>
<b>1.2.4 Dual Stage Input Coupled Transmission.....</b>	<b>16</b>
<b>1.3 Hydrostatic Unit .....</b>	<b>17</b>
<b>1.4 Planetary Gear Train .....</b>	<b>20</b>
<b>1.5 Hydro-mechanical CVT Power Split Transmission: operating principle .....</b>	<b>22</b>
<b>1.6 Multiple-mode transmission.....</b>	<b>28</b>
<b>1.7 Energy recovery system in hydro-mechanical transmission .....</b>	<b>29</b>
<b>Design and Simulation .....</b>	<b>34</b>
<b>2.1 Design of CVT power split transmission.....</b>	<b>34</b>
<b>2.2 Design of CVT input coupled .....</b>	<b>36</b>
<b>2.3 Design of hydraulic transmission .....</b>	<b>38</b>
<b>2.4 Design of CVT input coupled with hydraulic starting mode.....</b>	<b>40</b>
<b>Power Split HM CVT simulation model .....</b>	<b>46</b>
<b>3.1 Hydrostatic CVT transmission model.....</b>	<b>46</b>
<b>3.2 Hydraulic unit model.....</b>	<b>47</b>
<b>3.3 Modelling of simple gears and the planetary gear train.....</b>	<b>49</b>
<b>3.4 Modelling of transmission system control.....</b>	<b>50</b>
<b>3.5 Modelling of energy recovery system .....</b>	<b>51</b>
<b>Simulation results.....</b>	<b>55</b>

4.1 Comparison of different design transmission .....	55
4.2 Gear change optimization.....	64
4.3 Constant power simulation.....	66
4.4 WLTC (Worldwide harmonized Light-duty vehicles Test Cycles).....	68
4.5 Simulation of energy recovery system.....	72
<b>Conclusion .....</b>	<b>77</b>
<b>Hydraulic anti-friction coatings .....</b>	<b>79</b>
5.1 Definition.....	79
5.2 Friction and Wear in Hydraulic Axial Piston Pump .....	81
5.2.1 Tilting moment acting on cylinder block.....	82
5.2.2 Reaction force on piston slipper.....	86
5.3 Hydrophobic materials .....	91
<b>Materials and Method.....</b>	<b>95</b>
6.1 Texturing surface analysis .....	95
6.2 Hydrophobic surface analysis.....	102
6.2.1 Dog-bone samples .....	102
6.2.2 Wettability measurements .....	104
6.2.3 Scratch Test .....	104
6.2.4 Tensile Test.....	106
6.2.5 Surface morphology characterization .....	106
<b>Experimental results .....</b>	<b>109</b>
7.1 Texturing experimental results .....	109
7.1.1 Friction and wear .....	109
7.1.2 Effect of dimples diameter .....	111
7.1.3 Effect of dimples density .....	117
7.1.4 Effect of dimples depth.....	122
7.1.5 Wear track.....	125
7.2 Hydrophobic experimental results .....	127

Index

<b>7.2.1 Scratch Damaging</b> .....	133
<b>7.2.2 Tensile Damaging</b> .....	136
<b>Conclusion</b> .....	147
<b>References</b> .....	149



## **Abstract**

The PhD project aims to develop a new type of CVT for application on a street sweeper, using the Jarchow model which involves the use of a multi-range transmission with hydraulic first mode. The further innovative aspects of the transmission concern the simulation of an energy recovery system and the optimization of the hydraulic units efficiency through the study of innovative coatings applicable to rotating groups of pumps and hydraulic motors. As regards the development of the transmission, Simcenter Amesim simulation software was used. The results showed that applying a CVT input coupled with HSM (hydraulic starting mode) allows the use of only 6-7 kW, and therefore decreases the power of the ICE which is initially equal to 25 kW.

As for the innovative coatings, both superhydrophobic coatings and textured coatings were tested in order to evaluate their applicability in the hydraulic field. For the superhydrophobic coatings the mechanical resistance was tested through scratch tests and tensile tests, while for the textured coatings tribological tests were performed to evaluate the CoF.

Very promising results have been obtained from tribological tests on textured coatings, while the poor resistance and durability, shown by the failure analysis, limits the application of superhydrophobic coatings in the hydraulic field.

## Nomenclature

$\beta$  [ $^{\circ}\tau_0$ ] = Transmission ratio

$\omega_n$  [rpm] = Angular speed of last wheel

$\omega_1$  [rpm] = Angular speed of first wheel

$\omega_p$  [rpm] = Angular speed of carrier

CVT = Continuously Variable Transmission

HMT = Hydro-mechanical transmission

FMP = Full Mechanical Point

HSM = Hydraulic starting mode

$P_{ICE}$  [kW] = Engine power

$rpm_{ICE}$  [rpm] = Engine speed

$C_{wheel}$  [Nm] = Maximum wheel torque

$V_{max}$  [km/h] = Maximum vehicle speed

$m$  [kg] = Vehicle mass

$r_{wheel}$  [mm] = Wheel radius

$\Delta p$  [bar] = Max transmission pressure

$rpm_{motor/pump}$  [rpm] = Maximum unit speed

$\tau_{diff}$  = Transmission ratio of differential

$\tau_{cvt}$  = Transmission ratio

$\tau_{1,2,3}$  = Gear ratio

$V_I$  [cc] = Displacement of hydraulic pump

$V_{II}$  [cc] = Displacement of hydraulic motor

$C_{shift}$  [Nm] = Torque at shift speed

$\eta_v$  = Volumetric efficiency

$\eta_{h,m}$  = Hydro-mechanical efficiency

$F_{pb}$  [N] = Pressure force on the cylinder bottom

$A$  [mm<sup>2</sup>] = Area of each piston

## Nomenclature

$F_{rp}$  [N] = Piston friction force

$f_k$  = Friction coefficient

$F_f$  [N] = Axial force

$F_{op}$  [N] = Centrifugal force

$\vartheta$  [°] = Rotation angle of the cylinder block

$M_{tilting}$  [Nm] = Tilting moment

$N$  [N] = Reaction force of slipper pad

$F_a, F_b$  [N] = Reaction force of the piston against the cylinder bore

$M_o$  [Nm] = Moment equilibrium

$P_s$  [bar] = Supply pressure

$B$  [N s/m] = Viscous damping

CoF = Coefficient of friction

$Sq$  [ $\mu\text{m}$ ] = Root mean square height of the surface

$Ssk$  [ $\mu\text{m}$ ] = Skewness of height distribution

$Sku$  [ $\mu\text{m}$ ] = Kurtosis of height distribution

$Sp$  [ $\mu\text{m}$ ] = Maximum height of peaks

$Sv$  [ $\mu\text{m}$ ] = Maximum height of valleys

$Sz$  [ $\mu\text{m}$ ] = Maximum height of the surface

$Sa$  [ $\mu\text{m}$ ] = Arithmetical mean height of the surface

## **INTRODUCTION**

Hydrostatic transmission systems have been used for several years in all hydraulic applications that require fluid energy to perform their functions. They are used in various industrial and automotive applications such as road vehicles, earth-moving machines, agricultural machines and in large part also in industrial machines.

In the overview of hydraulic power transmissions, attention is focused on the CVT (Continuously Variable Transmission), automatic transmissions that achieve a continuously variable transmission ratio within a range of defined values. However, they show some limits, in particular the reduced load capacity and the low global efficiency. To overcome the loss efficiency of the CVT transmission, the Power-split technology has been designed, combining a hydrostatic CVT part with a mechanical transmission, using planetary gear train. This kind of transmission is capable of generating infinite transmission ratios and characterized by a good overall efficiency. This system is connected upstream to an internal combustion engine, which generates the power energy, and is maintained at a constant and controlled rotation speed, so as to limit the specific consumption of fuel.

The PhD project aims to develop a new type of CVT for heavy duty (HD) applications that can reduce energy consumption and allow the recovery of part of the energy during the negative phases of the work cycle. In order to increase the overall efficiency of the transmission, particular attention was paid to the use of innovative materials to reduce friction and wear, which represent one of the causes of energy loss in hydraulic units.

Highly hydrophobic coatings have been mechanically tested at the CERISI laboratories of the University of Messina to evaluate their use in the hydraulic field, while tribological tests have been carried out on textured coatings to assess the reduction of the friction coefficient (CoF) and wear.

## Introduction

As for the design of the CVT Power Split, different architectures were evaluated with and without energy recovery, through kinematic and dynamic simulations using the Simcenter Amesim® software.

The project takes on particular importance in the industrial sector, both because Italy is one of the most important manufacturers in the hydraulic field in the world, and because the increasingly strict rules regarding the environmental impact push the manufacturers of agricultural and earthmoving machinery towards technological solutions that allow to decrease consumption and that promote energy recovery.

The novelty of this study concerns the design of a hydro-mechanical CVT for small size machines, based on the Jarchow model. The design process i.e. referred to a street sweeper. The choice is due to the opportunity of reducing the environmental impact and therefore the CO<sub>2</sub> emissions, considering the constant use of this type of vehicle in the cities environment. Another innovative topic is the assessment of the mechanical performance of nano-structured coatings which allow to increase the overall efficiency of the transmission, acting on the efficiency of the hydraulic units.

The aforementioned PhD project has been eligible for funding in the final ranking of the announcement “*Innovative Doctorate: PON research and innovation 2014-2020*”, which belonged to the initiatives launched by the Ministry of Education, University and Research (MIUR) and addressed to the universities located in underdeveloped regions. The research topic is focused on two specific aspects, aimed at an innovative and efficiency hydro-mechanical transmission design:

- The study of energy recovery solutions, during the passive phases (braking) of the machine working cycle, thorough the using an electromechanical both storage and energy management system.
- The anti-friction coatings applicability, used to reduce friction and wear of sliding parts, realizing with innovative nanostructured materials such as super-oleophobic coatings and laser textured surfaces.

## Introduction

All the aforementioned activities have been carried out in collaboration with the *Hp Hydraulic S.p.A.* company from *Bondioli & Pavesi* Group, which deals with hydraulic pumps and motors design and production, situated in Pieve di Cento (BO), and *LABSON* (Laboratorio de Sistemas Oleohidráulicos y Neumáticos) research center of Polytechnic of Catalunya, which has the study, design and development of hydro mechanical, oleodynamic and pneumatic systems like its primary objective.

## CHAPTER I

### Hydro-Mechanical CVT Power Split

#### 1.1 Definition

Developments in the agricultural and heavy duty industry are due to the increasing demand to reduce fuel consumption and comfort efficiency.

In addition, there is a trend towards higher top speeds in the sector of heavy off road vehicles, where a faster driving speed on roads is desired [1].

The Power Split hydro-mechanical CVT is a kind of transmission that combines the variability of the CVT with the efficiency of a mechanical transmission [2]. It's characterized by a high efficiency mechanical branch and a hydrostatic one, which allows the gear ratio continuous variation between two fixed points. This kind of transmission allows to divide the motor rotation speed with respect to the shaft rotation speed at the transmission output. The main advantage is the optimization of the engine's operating point and the consequent reduction in fuel consumption.

Both mechanical and hydrostatic branch are connected through the use of a planetary gear on one side to the external load, and to the Internal Combustion Engine (ICE) on the other side. In particular, the power from ICE is divided into two aliquots, passes through both mechanical and hydrostatic path, then adds up into planetary gear [3].

In general, the Power Split hydro-mechanical (HM) CVT is a transmission that uses a hydrostatic transmission unit (HSU) to transmit the engine power through the mechanical and hydraulic paths, and can implement continuously variable speed change with the HSU. Power Split HM CVT has a higher power transmission efficiency than hydraulic transmission because it can transmit the power through the mechanical path, which is more efficient than the hydraulic one [4].

Due to these characteristics, many tractor manufacturers have been launching products using their own Power Split HM CVT models, including Vario® from Fendt, SMatic® from Steyr, ECCOM® from ZF, and Auto Power® from John Deere [5].

## 1.2 Different Design Layout

There are many different Power Split HM CVT design layout such as: Input Coupled, Output Coupled, Dual Stage and Compound [1].

Each construction layout has different characteristics, but there isn't the best choice than the others; it depends from the application.

### 1.2.1 Input Coupled

In the input coupled layout (figure 1), one of the two hydraulic units directly connected to the input shaft of the transmission by means of ordinary gears [6]. Its particular name means that the input torque is transmitted in part to the hydrostatic circuit and partly to the mechanical system, and the rotation speed at the output of the system derives from the link between the speed of the hydrostatic part and that of planetary gear.

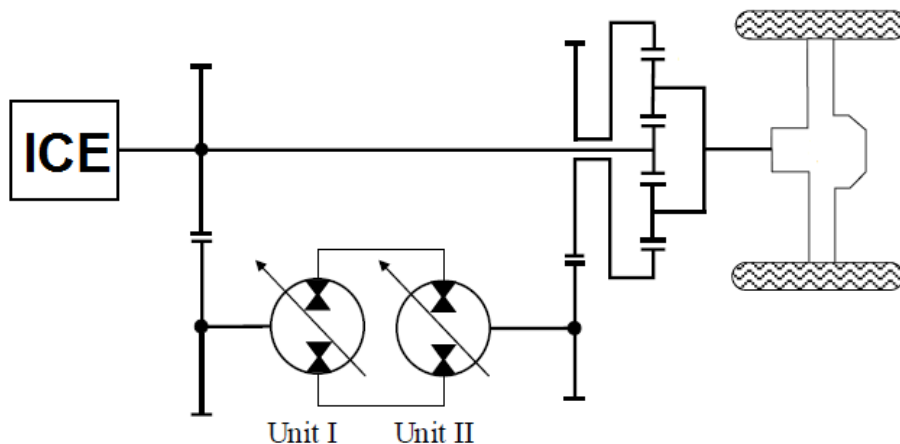


Figure 1 Input Coupled Layout [1]

### 1.2.2 Output Coupled

In the Output coupled layout (figure 2), the internal combustion engine is connected upstream of the planetary gearbox through the sun gear, while the unit I (pump) is connected directly to the crown gear and the unit II (motor) transmits the torque to the output shaft through an ordinary gear [7].

The working principle is similar to the input coupled, but the constructive layout is the opposite.

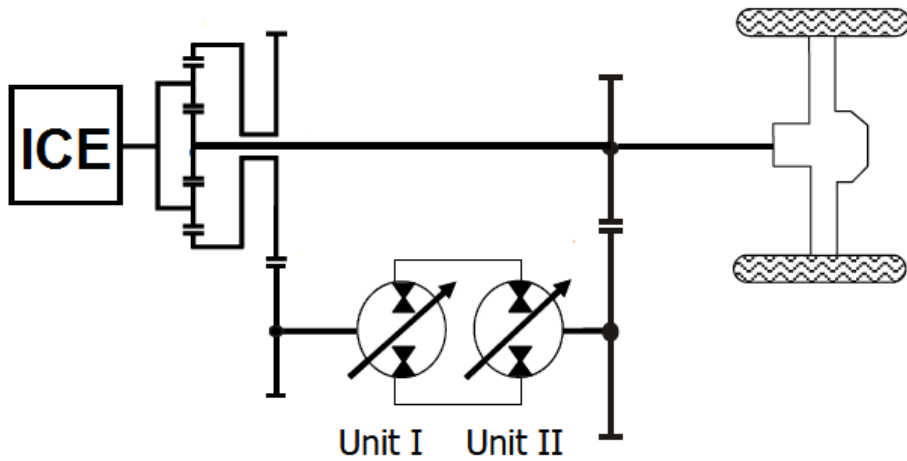


Figure 2 Output Coupled Layout [1]

### 1.2.3 Compound Coupled Transmission

For high power applications it is advantageous to use more advanced structures. This allows the necessary speed and torque requirements to be fulfilled with smaller/less units. The compound coupled transmission utilizes two planetary gear trains.

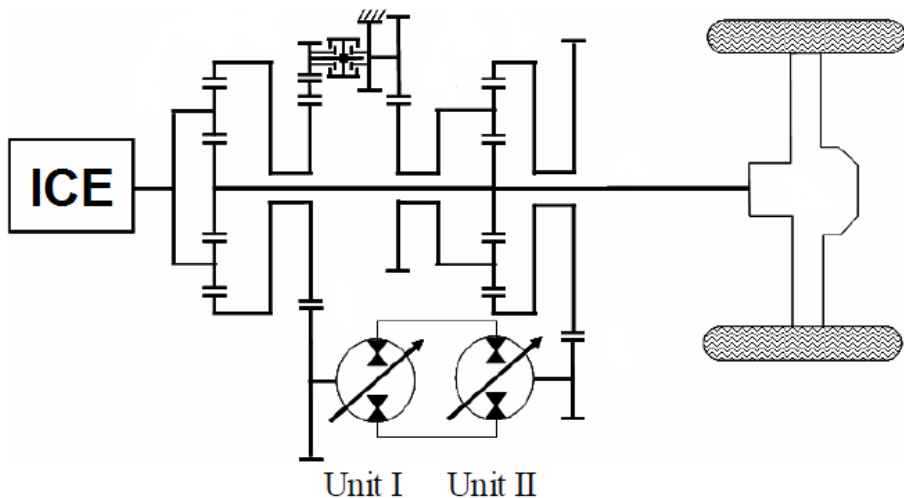


Figure 3 Compound Coupled Transmission [1]

There are a lot of benefits of the compound coupled transmission over the basic output coupled transmission, such as:

- A more efficient mechanical path for the power recirculation mode.
- The use of a second planetary gear allows the achievement of a second FMP, therefore the presence of several high efficiency points [1].

### 1.2.4 Dual Stage Input Coupled Transmission

Like the compound system, for high power applications it is helpful to use more complex architecture. To accomplish this, the dual stage transmission utilizes an advanced planetary gear train as shown in figure 4.

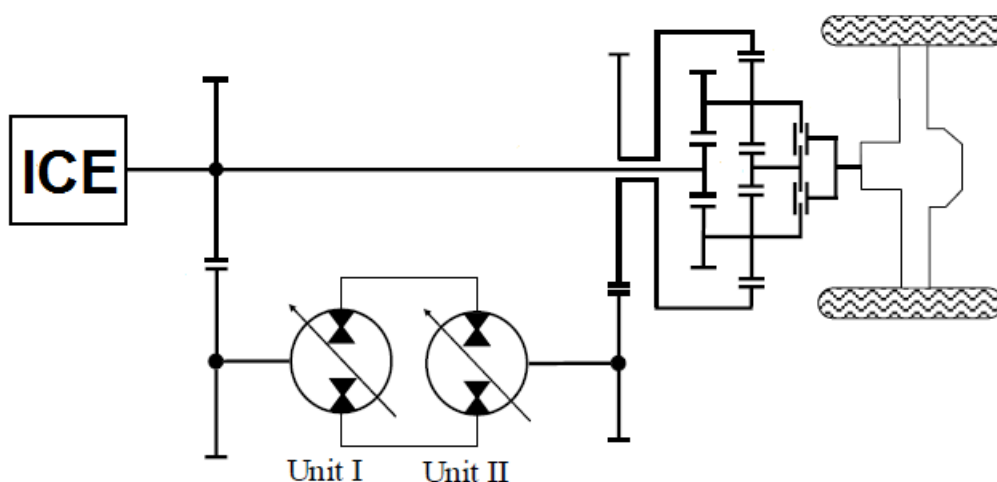
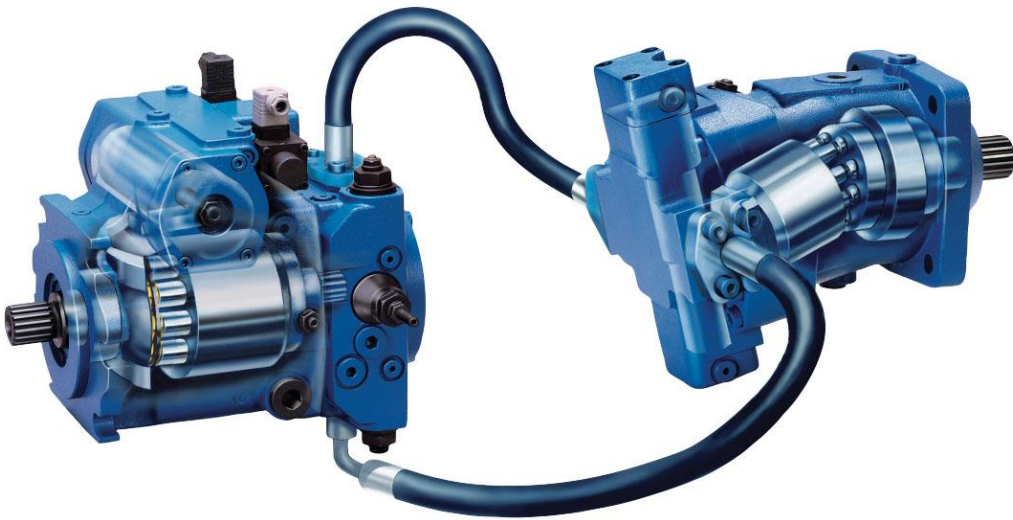


Figure 4 Dual Stage Layout Transmission [1]

In general, the Dual-stage system offers important benefits such as the use of more compact hydraulic units due to the presence of a more complex planetary gear train than the ordinary one. Furthermore, two different full mechanical points are reached, which characterize two high efficiency operating points [8].

## 1.3 Hydrostatic Unit

A hydrostatic transmission (figure5) transmits power through the use of a fluid at high pressures, typically an oil, and consists mainly of a variable displacement hydraulic pump and motor.



*Figure 5 Hydrostatic Unit [9]*

These elements are placed inside a closed hydraulic circuit, in which also secondary components such as tanks, safety valves, check valves, etc. are found (figure 6).

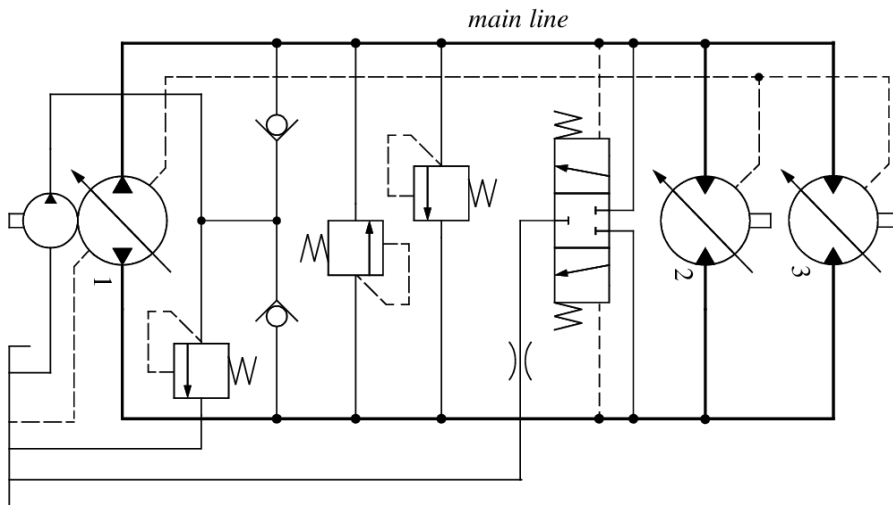


Figure 6 Hydrostatic Closed Circuit [10]

The hydraulic pump has the function to convert the mechanical power, coming from the drive shaft, into hydraulic power of the fluid; the hydraulic motor receiving the fluid from pump, has the function to convert the hydraulic power again into mechanical power, to move the output shaft. Hydrostatic pumps and motors working on displacement principle are designated as displacement machines.

Most of the displacement machines can be used as pumps as well as motors.

Piston pumps are the most commonly used displacement machines. They possess many advantages especially in the region of higher operating pressure.

Axial piston pumps (figure7) are characterized by cylinder bores, in which the piston executes a linear movement. The piston heads are in continuous contact with the fixed swash plate, which is arranged at a particular angle. During one revolution the piston execute a full stroke.

The variation of the  $\beta$  angle allows the changing of the pump displacement.

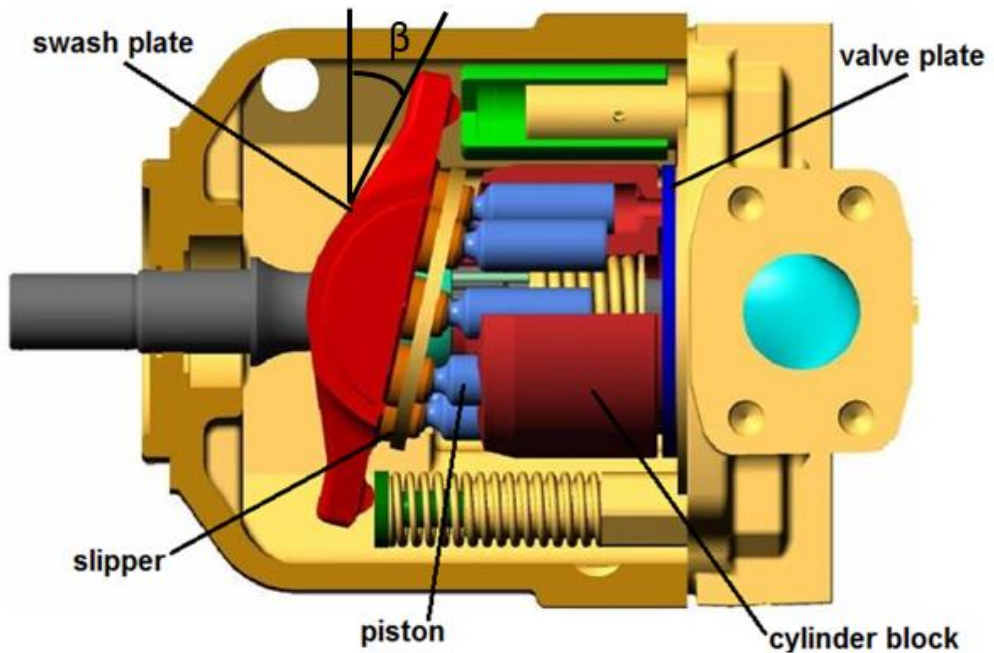


*Figure 7 Sectional view of an axial piston pump [taken from <https://www.forum-macchine.it/forum/lavori-agricoli-e-forestali/macchine-agricole/7896-pompe-a-pistoni-assiali-a-cilindrata-variabile-load-sensing>]*

It is important to highlight that the direction of the pump flow can be reversed by tilting the swash plate through zero to the opposite side, that means the flow direction can be reversed without changing the direction of rotation of the shaft. The connection of the displacement chamber with the suction and pressure ports of the pump is realized through a valve plate [11].

## 1.4 Planetary Gear Train

Planetary gear trains (PGTs) are widely used in various applications including tools, vehicles, motorcycles or turbines and so on. Automatic transmissions with PGTs have long been applied in the automotive industry because of their smaller volume and easier to manipulate compared to the conventional manual transmission. The functions of an automatic transmission are to transmit power from an engine to the drive wheels and keep the rotational speed of the engine within its working range [12]. The planetary gearing represents the mechanical core of a power-split CVT device, allowing the redistribution of the power coming from an input shaft between two different paths. Planetary gears consist of one or more idle gears, or *planet* gears, revolving about a central, or *sun* gear. Typically, the planet gears are mounted on a movable arm or *carrier* which itself may rotate relative to the sun gear. Epicyclical gearing systems also incorporate the use of an outer *ring* gear, which engages with the planet gears. The simple planetary gear train consisting of two central gears, sun gear and ring gear, and one or more planet gears connected with a carrier (figure8).

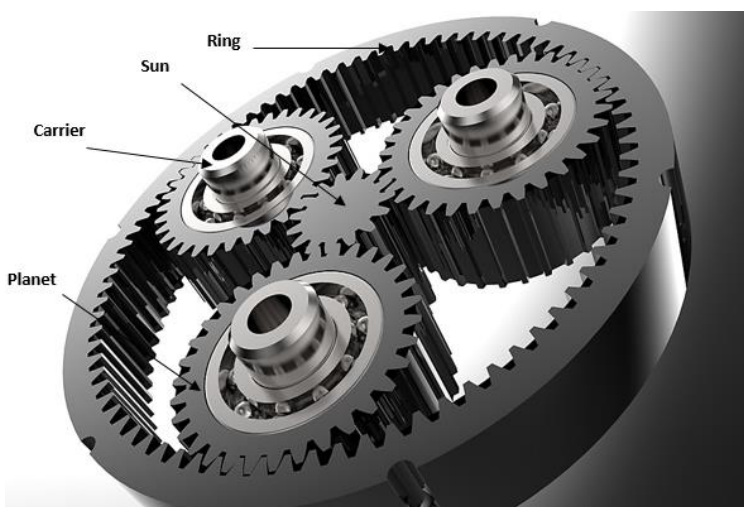


Figure 8 Planetary gears train

## Introduction

Considering an epicyclic gearing with  $n$  gears, the transmission ratio  $\tau_0$  is indicated as the ratio between the difference in the angular speed of the last wheel ( $\omega_n$ ) and the carrier ( $\omega_p$ ), and the difference between the angular speed of the first wheel ( $\omega_1$ ) and the angular speed of the carrier ( $\omega_p$ ), as shown in the following expression (1.1):

$$\tau_0 = \frac{\omega_n - \omega_p}{\omega_1 - \omega_p} \quad (1.1)$$

This expression is known as Willis' formula.

It is necessary to consider the rotation directions of the first and last wheels of ordinary gear: if the directions are in agreement,  $\tau_0$  must be assumed positive; otherwise, it must be assumed negative.

Willis' formula can be written in different ways, and in particular there are three cases: that wheel 1 is fixed, wheel  $n$  is fixed and the system has two degrees of freedom. If the wheel 1 is fixed, i.e.  $\omega_1 = 0$ , the Willis' formula becomes (1.2):

$$1 - \tau_0 = \frac{\omega_n}{\omega_p} \quad (1.2)$$

If the wheel  $n$  is fixed, i.e.  $\omega_n = 0$ , the Willis' formula becomes (1.3):

$$\frac{\tau_0 - 1}{\tau_0} = \frac{\omega_1}{\omega_p} \quad (1.3)$$

When gearing has two degrees of freedom, Willis' formula can be written (1.4):

$$\omega_p = \omega_1 \frac{\tau_0}{\tau_0 - 1} - \omega_n \frac{1}{\tau_0 - 1} \quad (1.4)$$

Advantages of planetary gears over parallel axis gears include high power density, large reduction ratio in a small volume, multiple kinematic combinations and coaxial shafting. Disadvantages include high bearing loads, inaccessibility, and design complexity.

## 1.5 Hydro-mechanical CVT Power Split Transmission: operating principle

The HM CVT is a type of continuous gearbox that uses variable displacement pumps and hydraulic motors. In this type of transmission, the rotary motion of the motor drives a hydrostatic pump on the driver side. The pump converts rotational movement into fluid flow. Then, with a hydrostatic motor positioned on the driven side, the fluid flow is reconverted into a rotating movement (figure 9).

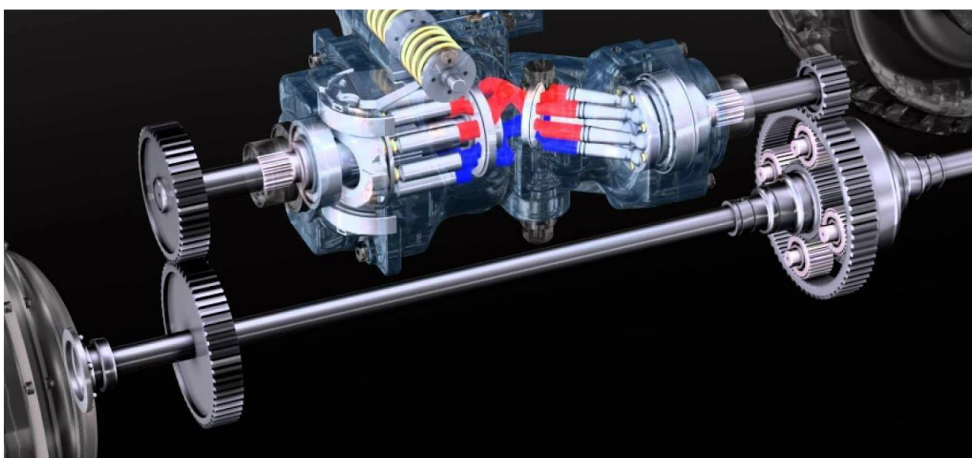


*Figure 9 CVT Power Split Hydro-mechanical [taken from [https://www.youtube.com/watch?v=T5vpqI7SmIc&ab\\_channel=BoschRexroth](https://www.youtube.com/watch?v=T5vpqI7SmIc&ab_channel=BoschRexroth)]*

## Introduction

In the input coupled configuration, the motor is coupled directly with the hydrostatic CVT transmission, while in the output coupled configuration the engine is coupled to the epicyclical reduction gear, present upstream of the hydraulic branch.

By analysing the power flows of the input coupled transmission, three possible operating modes are realized:

- Additive
- Positive circulating
- Negative circulating

In the additive configuration the input power is divided into the two branches, and is re-joined at the output using the planetary gear. In this case the power that circulates in both branches is always less than the entry one. In the positive circulating configuration there is a power recirculation in the mechanical branch with a fixed transmission ratio, this means that there will be a greater power flow circulating in the variable hydrostatic branch.

In the negative circulating configuration, a part of the power is recirculated on the CVT branch using the planetary gear train. The power in the mechanical branch will be greater than that circulating in the hydrostatic transmission, and can exceed the input power. When this situation occurs, that is a greater power circulating in the hydrostatic branch compared to the inlet branch, the overall efficiency of the system decreases heavily, being the worst condition in terms of efficiency.

Starting from the stationary vehicle, it can be observed that the transmission operates first in negative circulating mode, after which it goes into additive mode (figure 10). The transition between the modes is called full mechanical point, and establishes the point at which the power of the hydrostatic branch is zero (since the hydraulic motor has a displacement equal to zero), and all the input power is transferred to the mechanical branch.

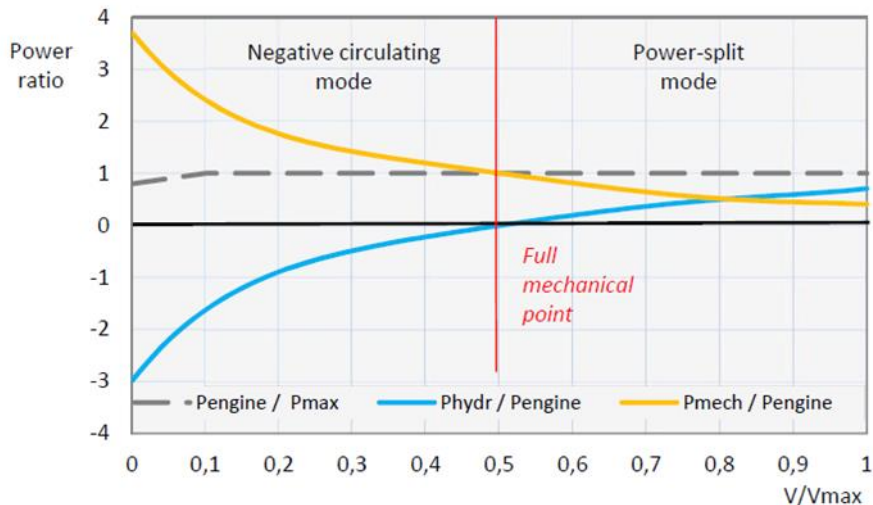


Figure 10 The power ratio in the three operating modes [13]

At low vehicle speeds, or in negative circulating mode, the power that circulate on the hydrostatic branch is very consistent and therefore the transmission efficiency is very low. At high speeds, on the other hand, the transmission operates in Power-split mode, i.e. the additive mode; in this case the input power is shared between the two branches and the power part transmitted on the CVT branch is much more limited. When the transmission enters in the Positive circulating mode, and therefore the recirculation of power involves the mechanical branch, the power transmitted in the hydrostatic branch is very high, therefore the efficiency decreases considerably. In order to achieve reverse in these transmissions, mechanical, hydraulic or electro-hydraulic reversers are generally used.

The operation of the input coupled transmission is now analysed:

In the machine starting phase, the transmission is in a negative circulating condition. The pump (unit P) is in the maximum displacement condition and the power input to the transmission will recirculate entirely on the hydraulic branch (figure11). In this condition the carrier will have almost zero speed, as will the output power of the

Introduction

transmission. it should be noted that in this condition the motor acts as a pump and vice versa.

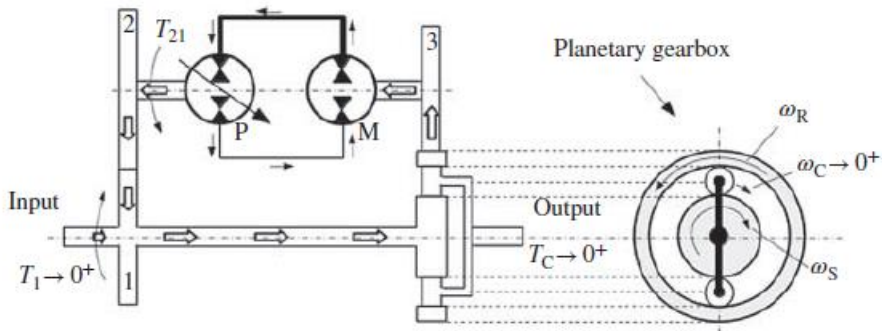


Figure 11 Diagram of the starting phase of the input coupled transmission [14]

To accelerate the vehicle (figure12), the pump varies its displacement and in particular moves from the maximum displacement towards zero displacement. The power coming from the ICE is not completely recirculated in the hydraulic branch and there will be a higher output torque.

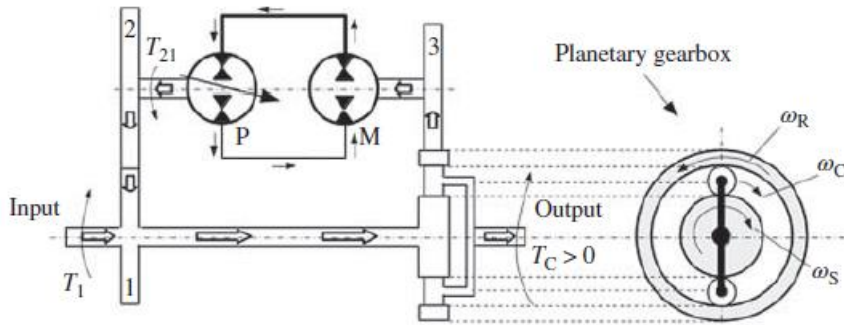


Figure 12 Diagram of the acceleration phase of the input coupled transmission [14]

By continuing to decrease of the pump displacement (figure13), the condition of full mechanical point is reached. In this condition the pump will have zero displacement, the motor will have zero rotation speed as well as the crown gear. In this condition all the input power will be transmitted through the mechanical branch. As already

## Introduction

said, this condition guarantees the greater efficiency of the transmission, since there is no circulating power of the hydraulic branch.

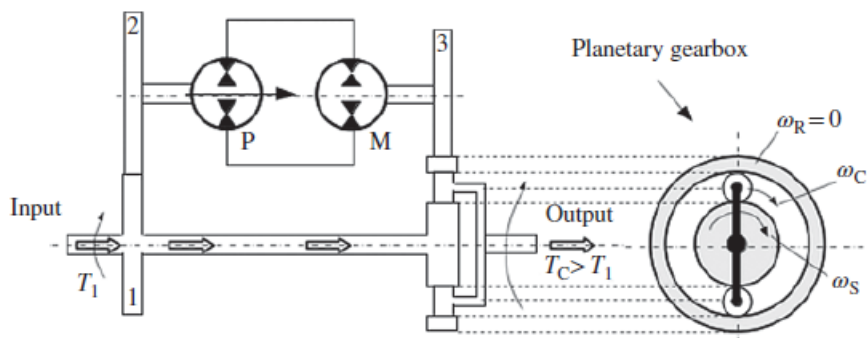


Figure 13 Full Mechanical Point [14]

By inverting the pump displacement, the power split mode is obtained, i.e. the power will be split at the transmission input and is added by means of the planetary gear. It should be noted that in power split mode, the pump (unit P) works as a pump and the motor works as a motor (figure 14).

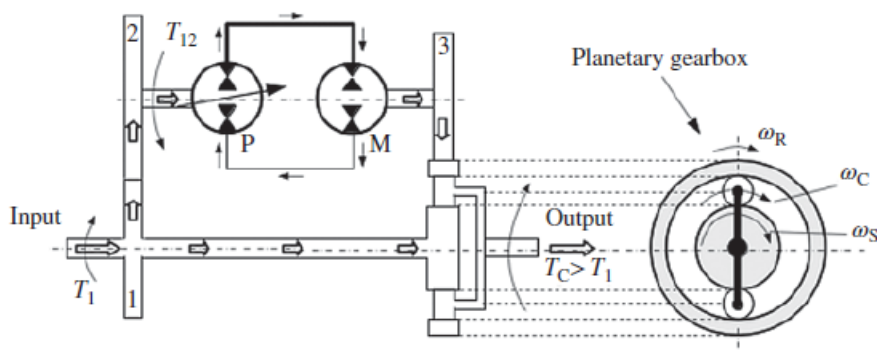
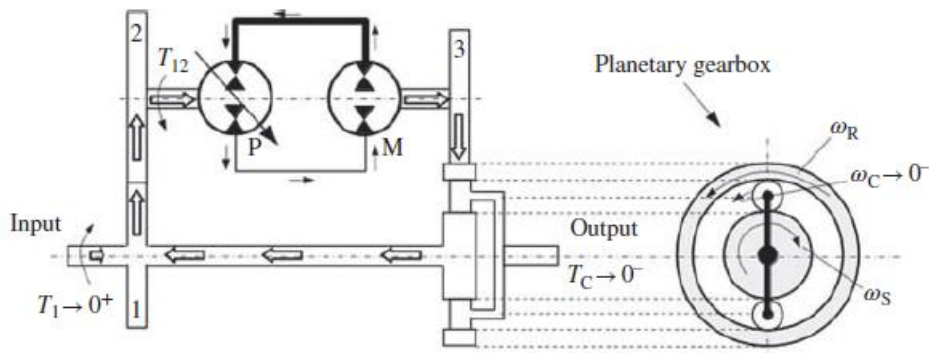


Figure 14 Power Split Mode [14]

## Introduction

Reverse gear coincides with the positive circulating mode (figure15), which is the mode with lower efficiency, due to a high recirculation of power on the hydraulic branch [17].



*Figure 15 Diagram of the phase of positive recirculating mode transmission input coupled [14]*

It is possible to explain the behaviour of the input coupled transmission, analysing the behaviour of the hydraulic units shown in the figure 16. In particular, from the start of the vehicle (negative circulating), the pump varies its displacement (grey curve) from -1 to 0 and the motor decelerates (blue curve) from 3500 rpm to 0. When the pump has zero displacement and the motor has zero speed, the full mechanical point will be reached. Exceeded the point of FMP, the vehicle will be in power split mode, i.e. the pump will increase its displacement from 0 to 1, while the motor will go from 0 to 3500 rpm. During the operation of the input coupled transmission the pump will keep its max speed constant (orange curve) and the motor will not change its displacement (yellow curve).

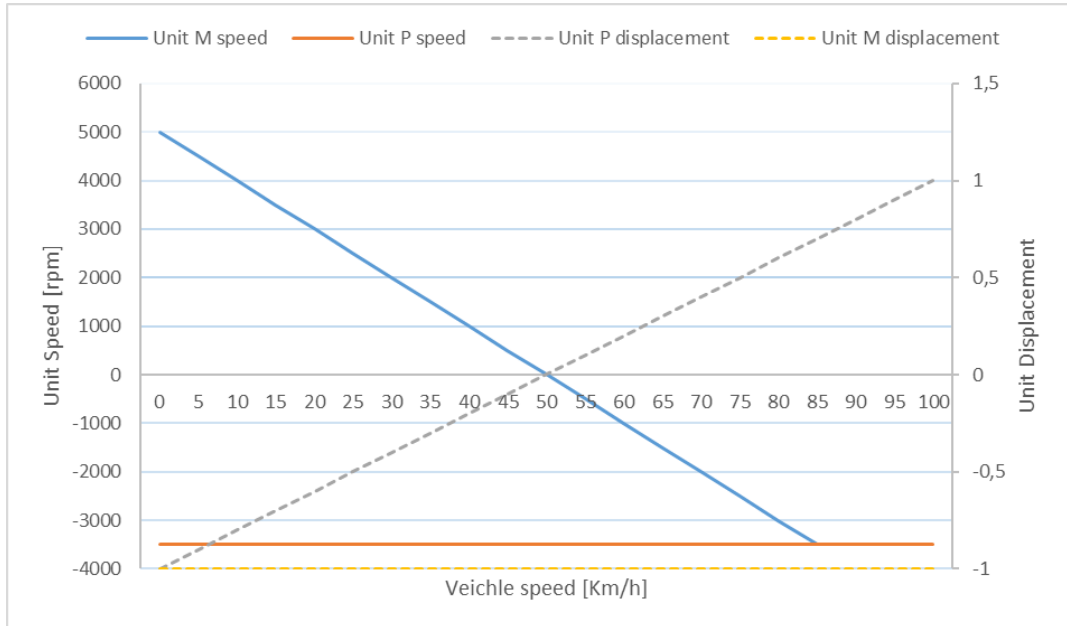


Figure 16 Behaviour of hydraulic units

In general, input coupled systems are suitable for low power applications but they require a more compact functional scheme compared to output coupled transmissions.

## 1.6 Multiple-mode transmission

A multiple-mode hydro-mechanical CVT combines several basic hydro-mechanical transmissions (HMTs) by using clutches. The behaviour of each mode is the same described in section 1.5. By switching between the modes, the total speed ratio is increased as well as the total transmission efficiency. The multiple mode transmission allows a wide conversion range without the use of large displacement hydraulic machines. This represents a fundamental aspect that allows to increase the total transmission efficiency, keeping the overall dimensions of the hydrostatic units unaltered, and in some cases, also reducing the size. A large number of studies have

been performed over the year, and many multi-range systems have been commercialized. Liu et al [15] have studied a multi-range hydro-mechanical transmission based on dual stage input coupled layout. An example of HTM multi-range is represented by the study of Mistry et al. [16], which show a CVT transmission applied on John Deere tractors.

Another kind of multi-range HMT is based on Jarchow concept [17], and consists of HMT with a hydrostatic starting mode. The first forward mode is purely hydrostatic and is followed by an arbitrary number of input-coupled power-split modes for the forward motion [18], [19].

## **1.7 Energy recovery system in hydro-mechanical transmission**

The decrease in fossil fuel resources and the increase in environmental pollution are nowadays two of the most important issues on the world scene, which have encouraged the development of green technologies, aimed at energy saving and emission reduction. In recent years, the automotive industry has introduced hybrid cars, such as the Honda Insight and the Toyota Prius, which minimize the use of internal combustion engines by integrating them with electric motors [20].

Also in the field of agricultural and earthmoving machinery, which from a technological point of view turns out to be 10/15 years behind the automotive industry, numerous scientific studies are underway in order to apply a hybrid transmission, which can allow energy saving and consequently the reduction of CO<sub>2</sub> emissions [21]–[23]. Agricultural and earth-moving machines are characterized by low energy efficiency, especially in the acceleration, braking and movement of devices they are equipped (bucket).

Energy recovery systems can be divided into three categories [24]:

## Introduction

- Electric storage systems
- Hydraulic storage systems
- Mechanical accumulation systems

An electric storage system (figure17) adopts a battery, ultra-capacitor (UC), or both as the storage unit. Two electric motors are adopted in this system. One electric motor is coupled with the hydraulic motor to form an energy recovery unit that recovers potential energy during boom-lowering or swing-braking of the platform.

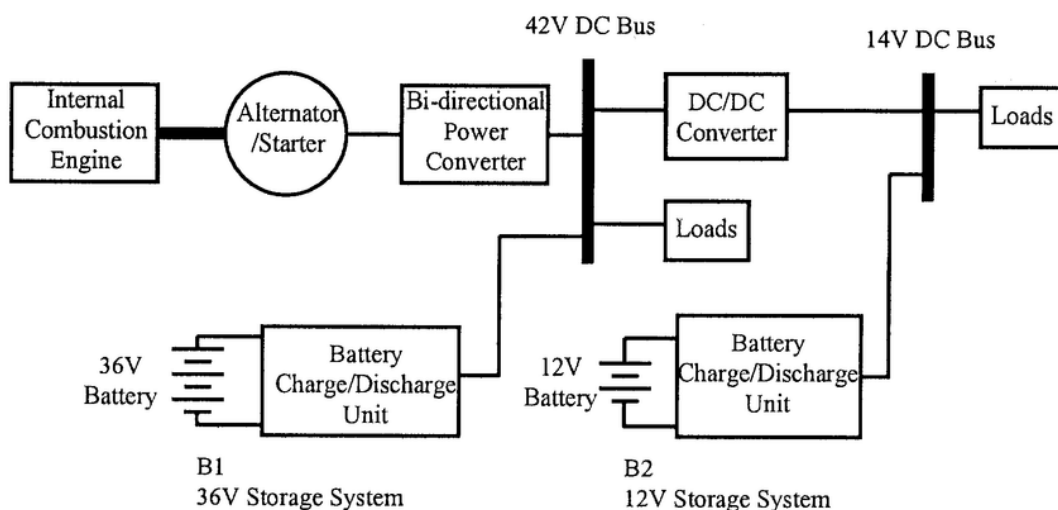


Figure 17 Scheme of electric storage system [25]

In a hydraulic recovery system, a hydraulic accumulator with compressed nitrogen serves as the storage unit, which absorbs recoverable energy from the hydraulic actuator (figure 18). Under the recovery condition, pressure oil discharged from the actuator is charged into the hydraulic accumulator. Under the energy regeneration condition, charged oil is released to drive the hydraulic system.

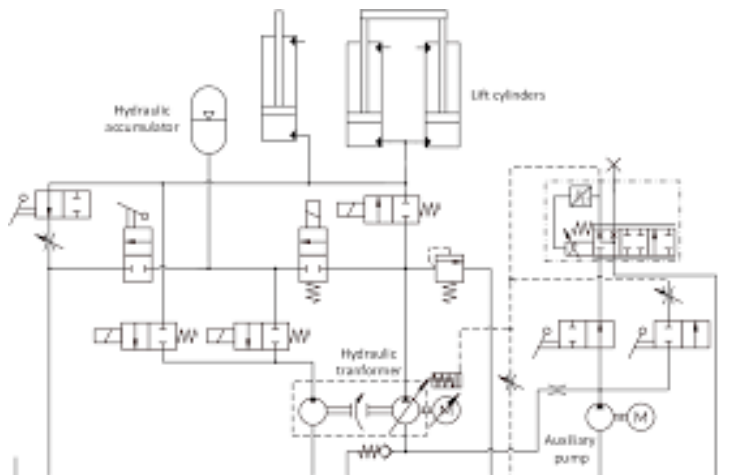


Figure 18 Scheme of hydraulic recovery system [26]

In a mechanical storage system (figure 19), a hydraulic pump/motor is utilized as an energy transfer device between hydraulic and mechanical energy. A flywheel providing energy storage is the main component in this system.

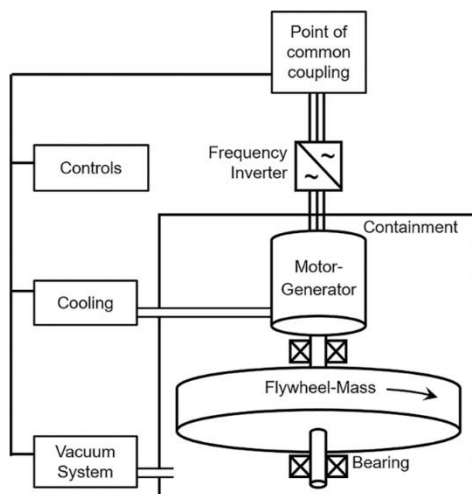


Figure 19 Scheme of mechanical recovery system [27]

The hydraulic hybrid powertrain uses hydraulic pumps and motors for power transmission. The energy from regenerative braking is stored in the form of

pressurized fluid in hydraulic accumulators. Later when the vehicle accelerates, this pressurized fluid can be used to drive the hydraulic motors and thereby power the vehicle. Similar to electric hybrid systems, hydraulic hybrid systems have three main types of architecture i.e. series, parallel and series-parallel or power split. In series hybrids, the primary energy source i.e. the internal combustion engine is connected to a closed circuit hydrostatic transmission with a variable displacement pump connected to a variable displacement motor and a secondary energy source i.e. an accumulator in a high pressure line. The vehicle is capable of storing energy in the secondary energy source through regenerative braking, which can be used either alone or in conjunction with the engine to power the wheels.

In parallel hybrids, a highly efficient mechanical transmission is used between the engine and the wheels, while a variable displacement unit that can operate as both pump and motor is inserted between the secondary energy source i.e. the accumulator and the wheels. Although both the energy sources can provide torque to the wheels at the same time, the engine speed is determined by the vehicle speed and the current transmission ratio.

However, due to multiple sources of torque, the control architecture for parallel hybrids is relatively complex, and the mechanical coupling of the engine to the wheels (for non-CVT transmission) typically limits the power management strategies.

The so-called series-parallel or power-split hybrid uses a continuously variable transmission to combine both the series and parallel configurations. This architecture has the advantage of using the highly efficient mechanical path in steady state driving and the hydraulic path during unsteady driving like speed variations or for power boost.

All the hydraulic hybrid architectures have their advantages and disadvantages. While the series hybrid has the advantage of independent engine speed control, it has a drawback in terms of the overall driving feel. Since, the series hybrid has the

## Introduction

accumulator directly connected to the high pressure line, there is effectively one source of torque to the wheels at all times. In case the accumulator pressure is unable to meet the torque demanded at the wheels, the hydraulic pump has to raise the accumulator pressure in order for the accumulator to supply the required torque. The parallel hybrids allow the speed and torque of the engine to be chosen independently thereby facilitating engine downsizing, however, the transmission control is particularly complex due to multiple sources of torque at the wheel simultaneously. The power split architecture has an advantage due to the direct mechanical linkage between the engine and the wheels, however, they face the same drawbacks as the series and parallel hybrids [28].

## CHAPTER II

### Design and Simulation

#### 2.1 Design of CVT power split transmission

In this chapter is analysed the design and simulation of different architecture of power split CVT transmission. Three transmission models have been proposed, i.e. hydraulic, hydro-mechanical, and hydro-mechanical with hydraulic starting mode CVT. Energy recovery has been designed for each model. The different models thus conceived were then compared with each other, considering the overall transmission efficiency. The comparison among various architectures was performed with the support of Simcenter Amesim®, which allows the creation of a functional transmission scheme using logical connections of mathematical blocks, and through the time variant analysis it calculates the fundamental parameters of the transmission, based on mathematical models proposed in different scientific studies [7], [29]. In order to obtain reliable results from the analyses obtained in this study, it was necessary to accurately model the power losses in the transmission, and in particular volumetric and hydro-mechanical losses in hydraulic machines.

The calculations of the input parameters of the transmission are based on those reported in the paper of the Ivantysynova [1], which makes a comparison between the four main architectures of CVT power split. The different architectures proposed below, have been modelled for a street sweeper machine whose data are shown in table 1

*Table 1 Operating characteristics of the reference vehicle*

<b>Parameter</b>	<b>Value</b>
Engine power ( $P_{ICE}$ )	25 kW
Engine speed ( $rpm_{ICE}$ )	1800 rpm
Maximum wheel torque ( $C_{wheel}$ )	4200 Nm
Maximum vehicle speed ( $V_{max}$ )	30 km/h
Vehicle mass (m)	2400 kg
Wheel radius ( $r_{wheel}$ )	0,3556 m

In addition to the above parameters, it is necessary to consider some parameters that represent constraints for the design of the transmission (table 2).

*Table 2 Hydrostatic and mechanical system parameters*

<b>Parameter</b>	<b>Value</b>
Max transmission pressure ( $\Delta_p$ )	380 bar
Maximum unit speed ( $rpm_{motor/pump}$ )	3500 rpm
Full mechanical point (FMP)	12 km/h
Transmission ratio ( $\tau_{diff}$ )	4
Transmission ratio ( $\tau_0$ )	1/3

The preliminary design of a hydro-mechanical transmission derives mainly from the choice of the standing gear ratio  $\tau_0$  of the planetary gear, the differential gear ratio  $\tau_{diff}$  and the speed at which the transmission will reach the full mechanical point, as shown in table 2.

Starting from these input data it was possible to size the input coupled transmission, the hydraulic transmission and finally the design of the more complex architecture represented by the power split hydro-mechanical CVT with hydraulic starting mode.

## 2.2 Design of CVT input coupled

To design the Input Coupled transmission (figure 20), the first parameter to choose is the vehicle speed at which the full mechanical point (FMP) occurs. Since the FMP is theoretically the point where the maximum efficiency of the transmission occurs, it is advisable to choose the speed at which the FMP occurs as the most used by the vehicle, for example the working speed. By making the point of maximum transmission efficiency to coincide with the speed typically assumed by the vehicle during the work cycle, it is possible to decrease fuel consumption and therefore the environmental impact.

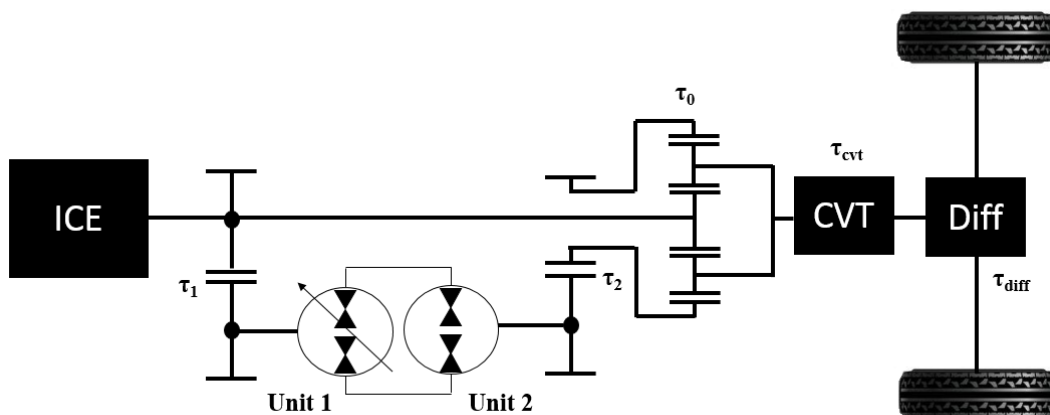


Figure 20 Scheme of input coupled transmission

The FMP occurs when the speed of the planetary crown C is zero, i.e. the speed of the shaft of unit II (hydraulic motor) is zero. The vehicle speed in the FMP depends on the choice of the transmission ratio to the differential  $\tau_{diff}$ , the transmission ratio of the planetary gear when the crown C has zero speed  $\tau_0$ .

Arbitrarily chosen the transmission ratio of the planetary gear  $\tau_0$ , the transmission ratio of the differential gear  $\tau_{diff}$  and defined the speed at which the FMP will occur, through equation (2.0) it is possible to determine the transmission ratio  $\tau_{cvt}$ , which

represents the transmission ratio assumed by the gearing downstream of the planetary gear, and upstream of the differential box:

$$V_{FMP} = \frac{rpm_{ICE}}{(1-\tau_0) \cdot \tau_{diff} \cdot \tau_{cvt}} \cdot r_{wheel} \cdot 3,6 \cdot \frac{\pi}{30} \quad (2.0)$$

The transmission ratio  $\tau_2$  between the shaft of the second unit (hydraulic motor) and the crown of the planetary gear is defined by setting the maximum speed of unit II as the boundary condition, according to expression (2.1):

$$\tau_2 = rpm_{motor} \cdot \tau_o \cdot \left[ \frac{V_{max} \cdot \tau_{diff} \cdot \tau_{cvt}}{r_{wheel} \cdot 3.6} \cdot (\tau_o - 1) \cdot \frac{30}{\pi} + rpm_{max} \right]^{-1} \quad (2.1)$$

The displacement of the second hydraulic unit is determined by imposing the maximum pressure limit  $\Delta p$ , and the maximum wheel torque  $C_{wheel}$ , according to equation (2.2):

$$V_{II} = C_{wheel,max} \cdot \left(1 - \frac{1}{\tau_o}\right)^{-1} \cdot (\Delta p \cdot \tau_2 \cdot \tau_{diff} \cdot \tau_{cvt})^{-1} \cdot 20\pi \quad (2.2)$$

The transmission ratio  $\tau_1$  is determined by the ratio between the speed of the internal combustion engine shaft ( $rpm_{ICE}$ ) and the rotation speed of the pump shaft, imposing the maximum pump speed as the boundary condition, according to the equation (2.3):

$$\tau_1 = \frac{rpm_{ice}}{rpm_{pump}} \quad (2.3)$$

Finally, it is possible to determine the displacement of the first hydraulic unit using equation (2.4):

$$V_I = V_{II} \cdot \tau_1 \cdot \tau_2 \cdot (\tau_0)^{-1} \quad (2.4)$$

The results of design calculations are summarized in the table 3.

*Table 3 CVT input coupled design parameter*

<b>Parameter</b>	<b>Value</b>
Gear ratio ( $\tau_1$ )	0.51
Gear ratio ( $\tau_2$ )	0.43
Displacement ( $V_I$ )	26 cc
Displacement ( $V_{II}$ )	17 cc
Gear ratio ( $\tau_{cvt}$ )	3.77

It should be noted that by carefully choosing the value of the standing gear ratio ( $\tau_0$ ) and the transmission ratio of the differential ( $\tau_{diff}$ ), gear ratio values between 1/6 and 6 are obtained, which represent the range of values that they allow to keep smaller dimensions and lower costs.

## 2.3 Design of hydraulic transmission

Following the same procedure used for the design of the input coupled transmission, a hydraulic transmission was designed starting from the input parameters shown in table 1. As shown in figure 21, the purely hydraulic transmission does not present the complexity due to the use of the planetary gear. However, the use of the hydraulic transmission could lead to low efficiencies especially at high speeds, if compared with the CVT power split.

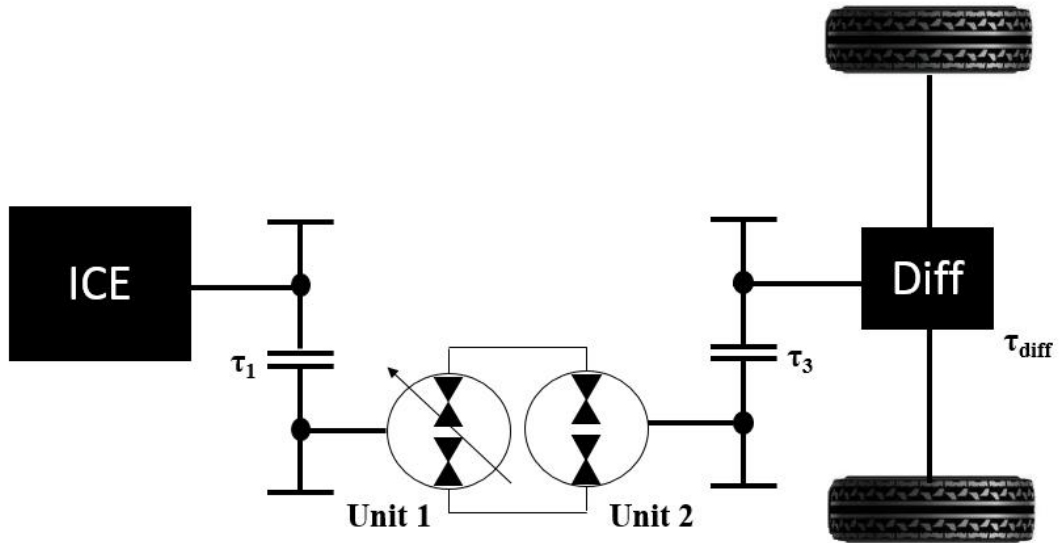


Figure 21 scheme of hydraulic transmission

The transmission ratios are then calculated and the hydraulic units are determined, according to equations (2.5), (2.6) and (2.7).

$$\tau_3 = rpm_{motor} \cdot \left[ \frac{V_{max}}{r_{wheel} \cdot 3.6} \cdot \frac{30}{\pi} \cdot \tau_{diff} \right]^{-1} \quad (2.5)$$

$$V_{II} = C_{wheel,max} \cdot (\Delta p \cdot \tau_3 \cdot \tau_{diff})^{-1} \cdot 20\pi \quad (2.6)$$

$$V_I = V_{II} \cdot \tau_1 \cdot \tau_2 \quad (2.7)$$

The results of design calculations are summarized in the table 4.

Table 4 hydraulic transmission design parameter

Parameter	Value
Gear ratio ( $\tau_1$ )	0.51

Gear ratio ( $\tau_3$ )	3.91
Displacement ( $V_I$ )	90 cc
Displacement ( $V_{II}$ )	45 cc
Transmission ratio ( $\tau_{diff}$ )	4

as shown in table 4, the choice to use a hydraulic transmission involves a substantial increase in the displacements of the hydraulic units, and therefore an increase in terms of dimensions.

The gear ratio  $\tau_3$  indicates the overall transmission ratio of the hydraulic branch, upstream of the differential.

The choice to use a fully hydraulic transmission could be justified, as will be discussed later, by the possibility of being able to recover energy along the entire speed range of the vehicle. However, this same behaviour cannot be adopted by the CVT input coupled, which cannot recover energy in the negative circulating mode phase.

In the next paragraph will be evaluated the possibility of combining the advantages of the Power Split CVT with the hydraulic transmission, designing a multi-stage transmission equipped with a hydraulic starting mode.

## 2.4 Design of CVT input coupled with hydraulic starting mode

As previously mentioned, resorting to a multi-range hydro-mechanical transmission involves, from a certain point of view, an increase in complexity due to the introduction of the clutches and the vehicle control system. However, a transmission with gear change could guarantee an increase in the overall efficiency of the transmission, and in particular the use of the first hydraulic gear could allow to have a vehicle that simultaneously exploits the advantages of the hydraulic

transmission at low speeds (where more power is required) and the advantages of input coupled transmission at high speeds.

Figure 22 shows the scheme of the input coupled transmission with hydraulic starting mode.

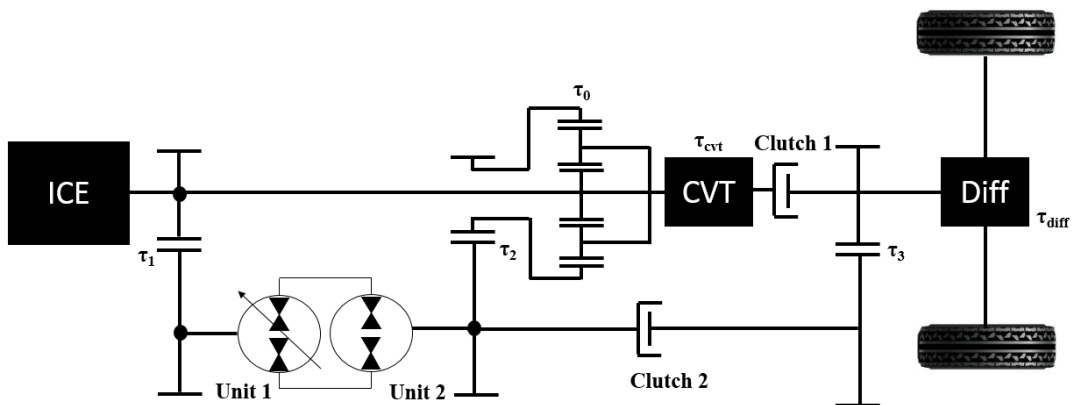


Figure 22 scheme of CVT input coupled with hydraulic starting mode

To achieve the change from the first hydraulic gear to the CVT, a synchronous gear change was used, that is, for the gear change to take place, the rotation speed of the two shafts must be the same. So, for the gear change to take place, it is necessary to study the shift speed, i.e. the speed of passage from the hydraulic transmission to the CVT. To determine the shift speed, it is useful to study the hydraulic motor behaviour separately in the two cases.

As shown in figure 23, the rotation speed of the hydraulic motor in a hydraulic transmission increases with the vehicle speed (red curve), while in a CVT power split transmission, in the negative circulating mode phase, it decelerates until zero speed at the point by Full Mechanical Point (blue curve). It is important to underline that it only meant considering the negative circulating mode, as it is the phase where the CVT transmission is least efficient, and coincides with the vehicle starting phase.

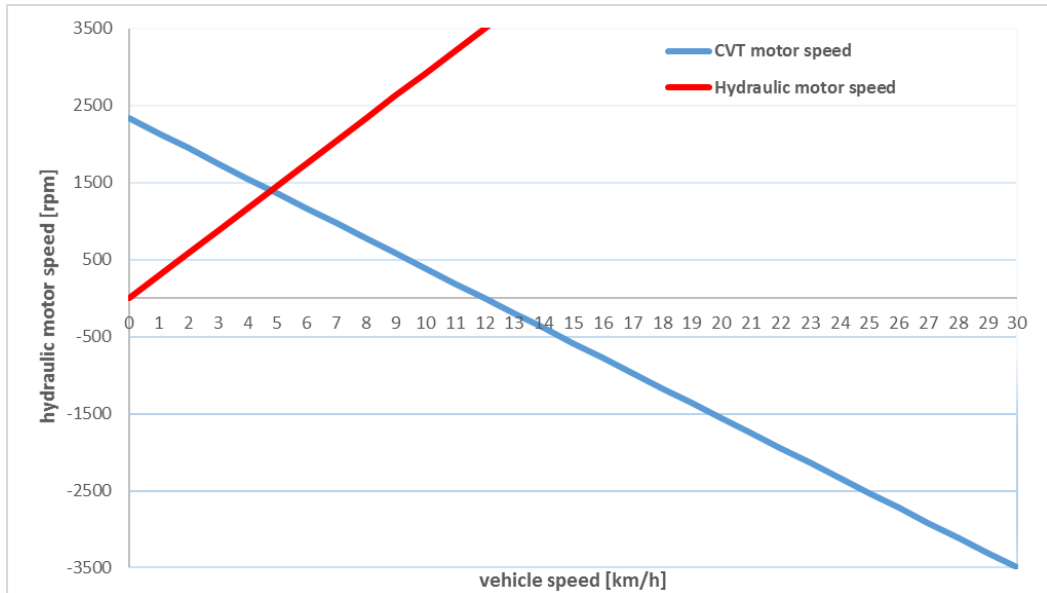


Figure 23 Trend of the rotation speed of the hydraulic motor as the vehicle speed changes

To size the hydro-mechanical transmission with hydraulic starting mode, it is necessary to consider the purely hydraulic transmission at first. This means that no power will be transmitted through clutch 1, which will be disengaged. As seen in the previous paragraph, the gear ratio  $\tau_3$  (equation 2.5) and the hydraulic motor displacement (equation 2.6) are then calculated if the transmission is entirely hydraulic. In equation (2.5) the maximum speed  $V_{max}$  is chosen arbitrarily, for example considering the maximum vehicle speed. Having calculated  $\tau_3$  and  $V_{II\ hydr}$ , it is necessary to determine the transmission ratio  $\tau_{cvt}$  downstream of the planetary gear, through the relationship (2.8) known the speed at the FMP, chosen according to the machine's working cycle.

$$\tau_{cvt} = \frac{rpm_{max}}{(1 - \tau_0) \cdot V_{FMP} \cdot \tau_{diff}} \cdot r_{ruota} \cdot 3,6 \cdot \frac{\pi}{30} \quad (2.8)$$

It is now possible to determine the gear change speed ( $V_{shift}$ ) as an intersection between the curve representing the hydraulic motor speed in the purely hydraulic transmission, and the curve representing the hydraulic motor speed in the continuously variable transmission (CVT), as shown in figure 23. Once determined the  $V_{shift}$ , we proceed to the calculation of the torque at which the gearshift takes place ( $C_{shift}$ ) through equation (2.9).

$$C_{shift} = \frac{P_{ICE}}{\frac{V_{shift}}{r_{wheel*3,6}} \cdot \frac{\pi}{30}} \quad (2.9)$$

Using the torque determined at the gear change speed, it is possible to determine the displacement of the hydraulic motor of the CVT, through equation (2.10).

$$V_{IIcvt} = C_{shift} \cdot \left(1 - \frac{1}{\tau_0}\right)^{-1} \cdot (\Delta p \cdot \tau_2 \cdot \tau_{diff} \cdot \tau_{cvt})^{-1} \cdot 20\pi \quad (2.10)$$

Once the  $V_{II CVT}$  is obtained, a comparison is made between the  $V_{II hydr}$  and the  $V_{II CVT}$ . If the displacements are similar, then the sizing could be considered completed, otherwise the calculation procedure is repeated.

It is interesting to note that, by changing the maximum speed that the purely hydraulic transmission must reach, the slope of the curve changes and the  $V_{shift}$  speed also changes (figure 24).

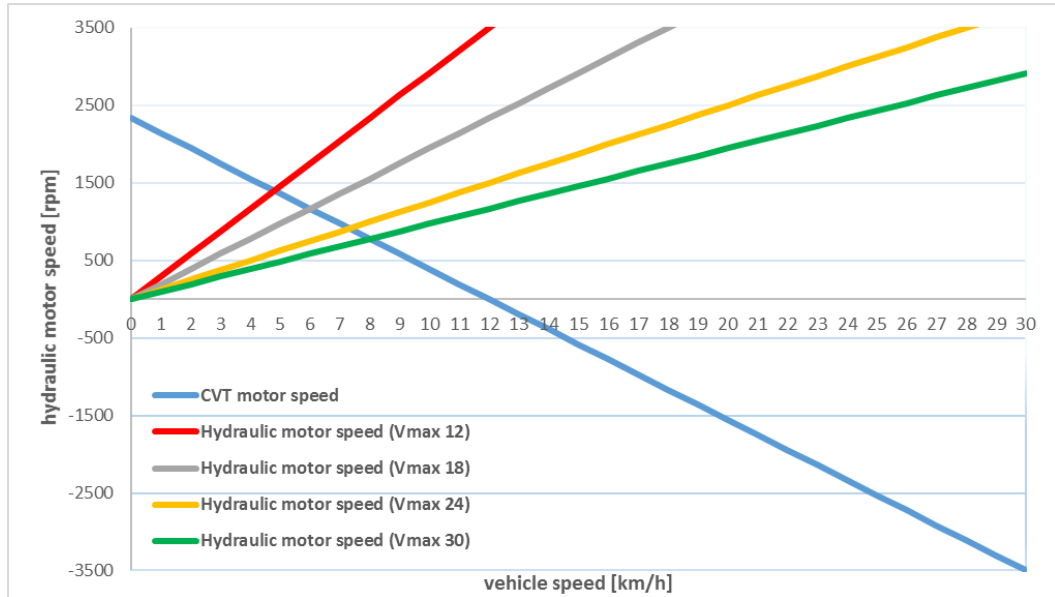


Figure 24 Variation of the gear change point when the hydraulic  $V_{max}$  changes

By varying the shift speed, the displacements of the hydraulic motor also vary, i.e. the demand for power required for the transmission varies during the purely hydraulic phase, or during CVT mode. As we will see later, it is necessary to find a compromise between the displacements of the hydraulic units, the efficiency of the transmission and the gear change point.

Table 5 shows the design parameters of the hydro-mechanical transmission with hydraulic starting mode.

*Table 5 hydro-mechanical transmission with hydraulic starting mode design parameter*

<b>Parameter</b>	<b>Value</b>
Gear ratio ( $\tau_1$ )	0.51
Gear ratio ( $\tau_2$ )	0.43
Gear ratio ( $\tau_3$ )	5.33
Displacement ( $V_I$ )	40 cc
Displacement ( $V_{II}$ )	39 cc
Gear ratio ( $\tau_{cvt}$ )	3.77
Transmission ratio ( $\tau_{diff}$ )	4
Transmission ratio ( $\tau_0$ )	1/3

## CHAPTER III

### **Power Split HM CVT simulation model**

The Simcenter Amesim® kinematic and dynamic modelling software was used to simulate the hydro mechanical CVT Power Split. The software allows simulating a system with complex interaction between multi-domain components and subsystems, through the use of numerous libraries characterized by pre-defined and validated components from different physical domains, such as fluid, thermal, mechanical, electromechanical, powertrain and many others.

In the case treated in this thesis, the hydraulic library was used to simulate the hydraulic branch of the transmission, the powertrain library to simulate the mechanical branch and the transmission gears, and the signal library to simulate the transmission control

#### **3.1 Hydrostatic CVT transmission model**

The scheme of the hydrostatic branch of the Power Split HM CVT transmission used in the simulation is shown in figure 25. It is characterized by two bidirectional hydraulic units, that are capable of acting both as motor and pump, one of which with variable displacement (pump) (1), and one with fixed displacement (motor) (2) both connected to a closed loop hydraulic circuit. A fixed displacement load pump is positioned inside the system, which in the case under consideration is equal to 20cc (3), which has the function of replenishing the oil within the hydraulic circuit.

The replenished oil flow rate, according to the operating pressures established in the low and high pressure branch, is discharged into the tank again through a safety valve (6).

There are two safety valves in the circuit (4,5) which put the high and low pressure branches in contact, and which take action to avoid damage to the transmission in the event of excessive overpressure. Depending on the load acting on the second hydraulic unit, the pressures acting on the two branches can be reversed. In this case, the distribution valve (7) comes into action; during its movement, it can be found in its central position, which is the neutral one, which does not allow the fluid to flow out. Also in this case the safety valve (6) acts, which allows the discharge of the flow towards the tank.

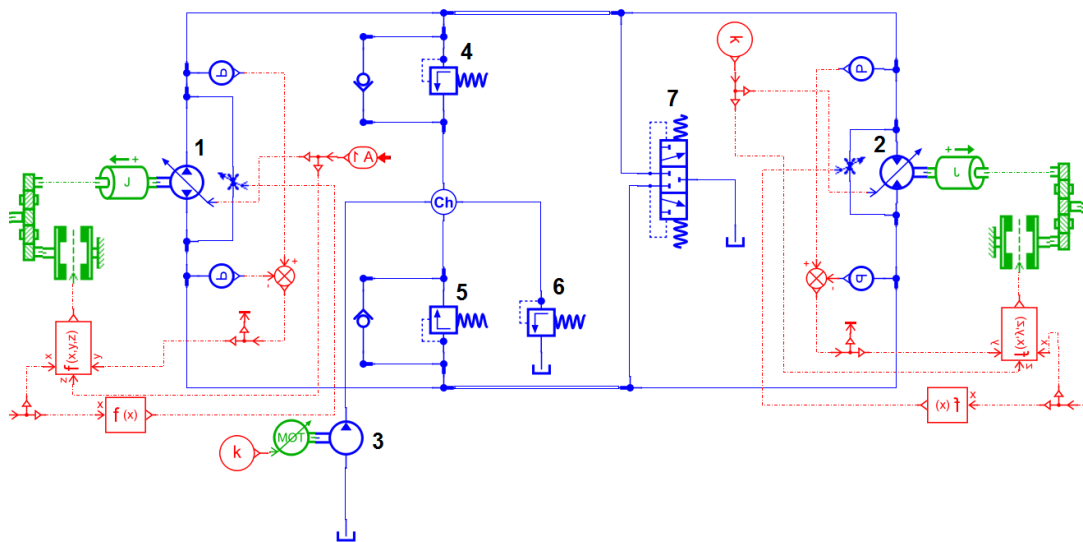


Figure 25 Hydraulic branch scheme of CVT

### 3.2 Hydraulic unit model

The pump and the hydraulic motor considered in the model refer to the axial piston type with variable displacement.

They are characterized by torque and flow values that can be calculated theoretically according to equations (3.0,3.1).

$$T_{ideal} = \frac{\omega V}{2\pi} \quad (3.0)$$

$$F_{ideal} = \frac{\Delta_p V}{2\pi} \quad (3.1)$$

To model the two real hydraulic units correctly it is necessary to introduce the hydro mechanical and volumetric efficiency, i.e. those parameters that allow to quantify the torque losses (hydro mechanical efficiency) and the losses due to the leakage of the fluid (volumetric efficiency) respectively.

Both the hydro-mechanical efficiency (3.2) and the volumetric efficiency (3.3) are a function of the displacement ( $\alpha$ ), the angular speed ( $\omega$ ) and the pressure ( $\Delta_p$ ).

$$\eta_v = f(\alpha, \omega, \Delta_p) \quad (3.2)$$

$$\eta_{h,m} = f(\alpha, \omega, \Delta_p) \quad (3.3)$$

Figure 26 shows the modelling of the losses in the hydraulic units, obtained using the signal and control library.

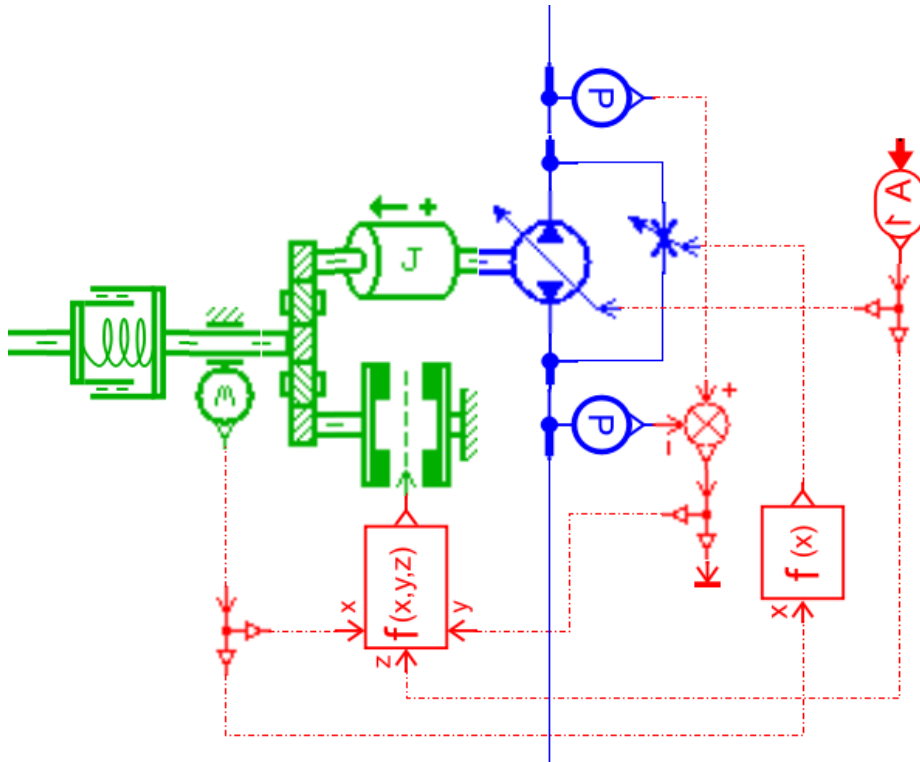


Figure 26 modelling of volumetric and hydro mechanical losses in hydraulic units.

As shown in figure 26 a clutch was used to model the torque losses, while a variable orifice was used to model the volumetric losses.

### 3.3 Modelling of simple gears and the planetary gear train

Figure 27 shows the schematic view of the mechanical branch of the transmission. The motion coming from the rotation of the internal combustion engine shaft is transmitted through branch "1" directly to the solar wheel "s", while the second hydraulic unit (motor) controls the rotation of the outer ring of the planetary gear "c", or transmits motion through shaft 2 during hydraulic starting mode. Both in the starting phase and after the gear change, the motion is transmitted to a "diff" gear which simulates the presence of the differential box.

The powertrain library of the Amesim® software is supplied internally with a logic block that features a simple planetary gearbox and blocks that simulate gear wheels. Figure 27 also shows the two clutches that engage when changing gears. In first gear the motion is transmitted through the hydraulic motor along the shaft 2 to the differential, while in second gear the motion is transmitted by the planetary gear carrier.

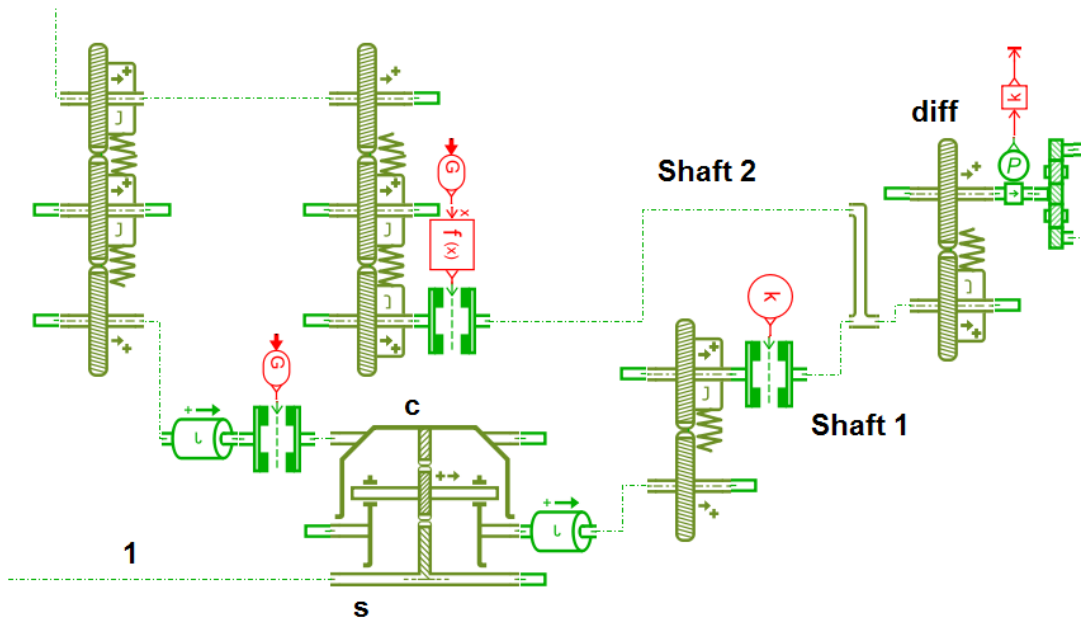


Figure 27 Schematic view of the mechanical branch

### 3.4 Modelling of transmission system control

The most complicated part of simulation concerns the transmission control. In the case in question it was necessary to model both the gear change and the control of the hydraulic units, both dependent on the mission profile of the vehicle. As shown in figure 28 the input of the system, which is the mission profile of the machine is obtained through a table block. The mission profile will then command both the

clutch control and the control of the hydraulic units. In particular, since the hydraulic motor has a fixed displacement, the control concerns only the displacement of the pump. The  $V$  (speed) signal regulates the clutch control and allows the change between the first pure hydraulic gear and the CVT. To control the clutches, a command (0,1) was used by means of a "switch" block set at the gear change speed ( $V_{shift}$ ). Below the gear change speed, the output signal  $G$  will be 0, while when the vehicle speed exceeds the  $V_{shift}$ , the output signal  $G$  will be equal to 1. The signal  $G$  will command a second "switch" block which will allow the passage of the pump displacement reference signal, either in the case of hydraulic start ( $G = 0$ ) or in the case of CVT ( $G = 1$ ). The reference signal will therefore be used for "current" control of the pump displacement.

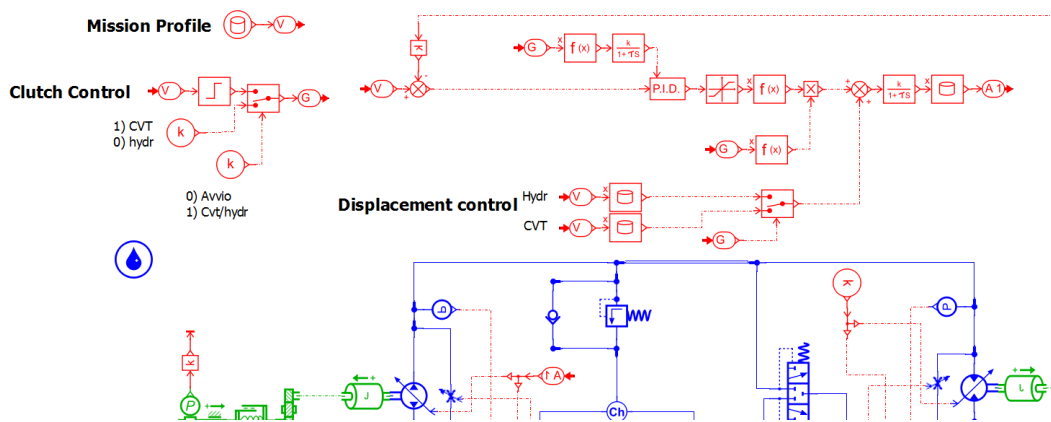


Figure 28 Scheme of hydro-mechanical transmission control

### 3.5 Modelling of energy recovery system

For the simulation of the energy recovery system, a simple system was considered characterized by the addition of a hydraulic pump (figure 29), which operates separately from the hydraulic branch of the transmission [30]. This type of system

allows comparing the energy recovery capacity in the different transmission architectures, without having to make any particular modifications.

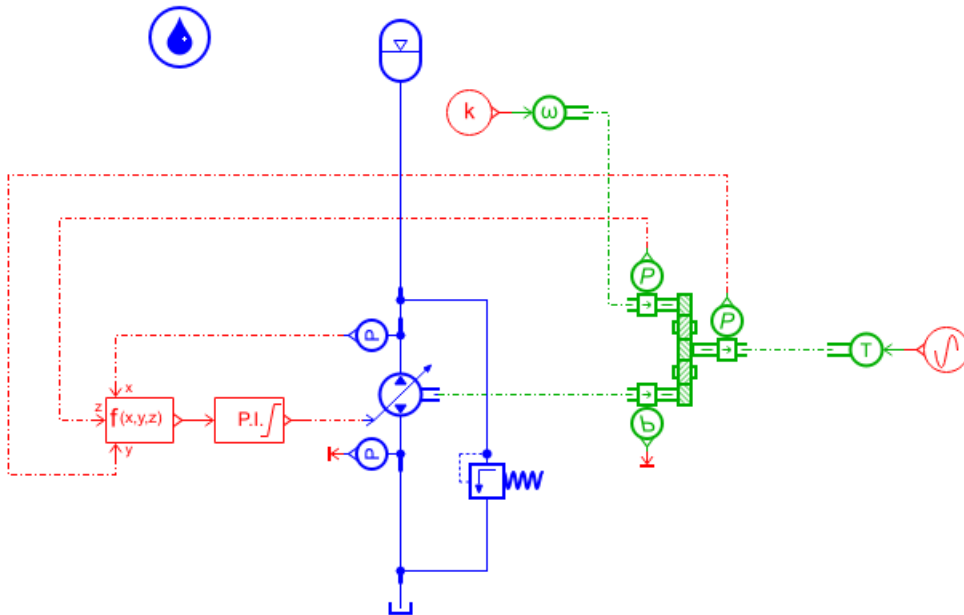


Figure 29 Energy recovery system

For the simulation, an accumulator with a capacity of 100 litres and with gas pre-charge pressure equal to 100 bar was considered.

In this way, a pump displacement control system has been created which allows the pressure to be maintained above 100 bar (a safety limit has been set at 120 bar). At the same time, a pressure relief valve set at 500 bar has been inserted. Considering for example a sinusoidal load, it is possible to evaluate the pressure behaviour of the accumulator by analysing figure 30.

## CVT Power Split HM simulation model

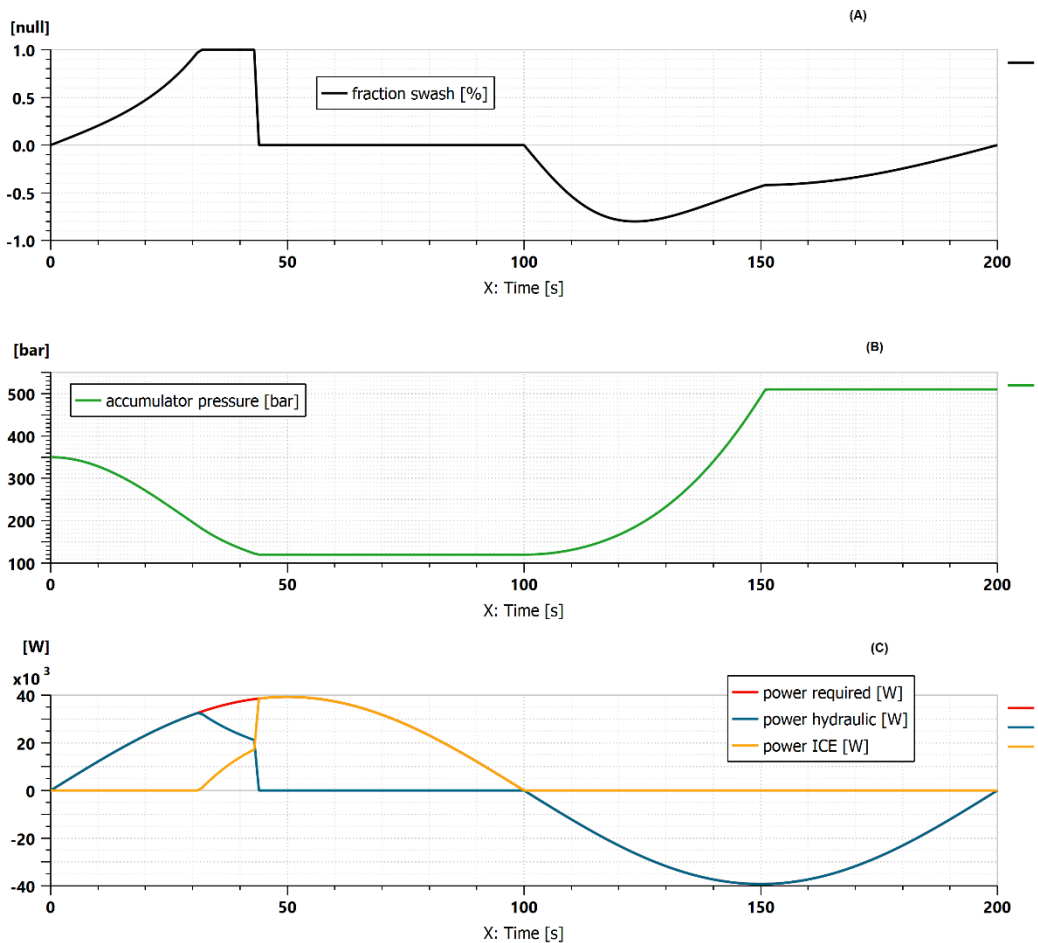


Figure 30 accumulator behaviour: a) variation of pump displacement; b) variation of the pressure of the accumulator; c) trend of the hydraulic power according to the required power.

As can be seen from figure 30, in the first part of the simulation, the required power is satisfied completely hydraulically (blue curve in figure 30 c). In the accumulator discharge phase (figure 30 b), the pump displacement passes from 0 to maximum, until the point where the accumulator pressure reaches 120 bar, which is the set limit pressure. At this moment the pump displacement passes from its maximum to 0, and

the internal combustion engine (ICE) intervenes which satisfies the remaining part of the required power (figure 30 c yellow curve). When the braking phase begins (at 100 s) the pump displacement decreases and the pressure in the accumulator increases until the maximum pressure of 500 bar is reached, pressure beyond which the pressure relief valve opens.

## CHAPTER IV

### Simulation results

#### 4.1 Comparison of different design transmission

The analysis of the different types of layout was carried out in a first approximation considering a "mission test" with a single acceleration phase from 0 to the maximum vehicle speed of 30 km / h.

With this type of mission test (figure 31), it was possible to analyse the transmission behaviour in detail and in particular to evaluate the overall efficiency in the individual operating phases of the transmission, i.e. the negative circulating mode, the full mechanical point and the positive circulating mode.

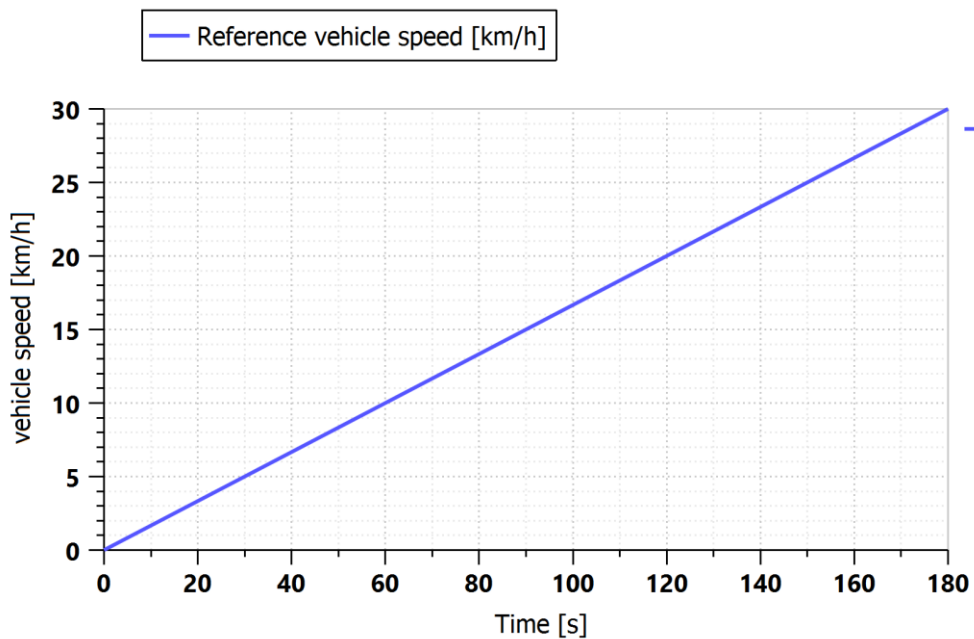


*Figure 31 Mission test*

## Simulation results

Figure 32 shows the total efficiency of the CVT HM with hydraulic starting mode when the vehicle speed changes.

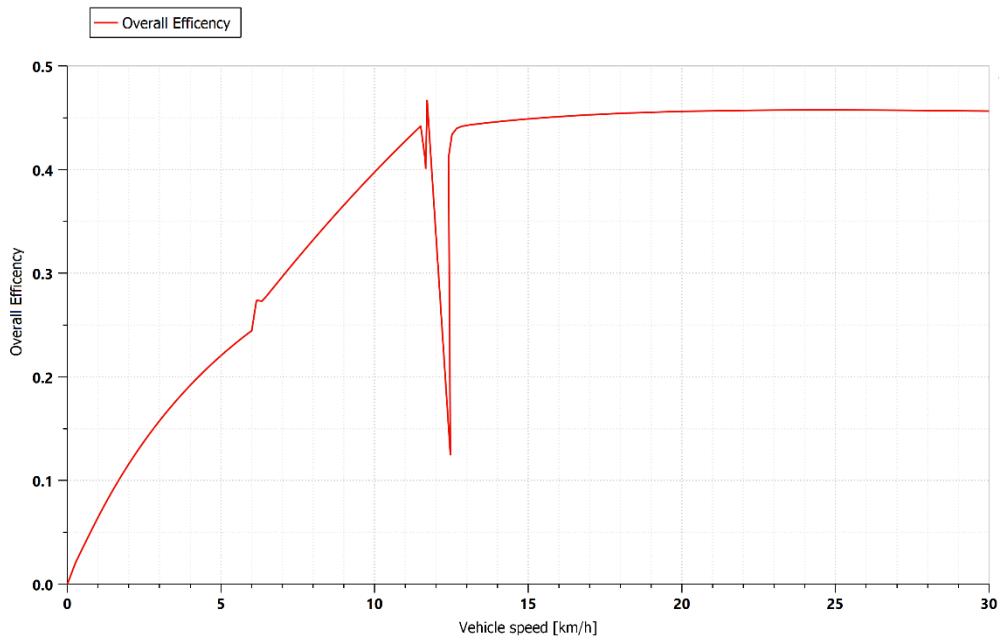


*Figure 32 Overall efficiency of CVT HM with hydraulic starting mode*

By analysing the performance trend, it is possible to highlight the transmission behaviour in the different phases:

- from 0 to 6 km / h the transmission works as if it were a pure hydraulic transmission.
- at 6 km / h there is a gear change. The gear change control opens the clutch on shaft 2 (figure 33 a) which will no longer transmit torque (figure 33 b), and closes the clutch on shaft 1. At this moment the transmission behaves like a CVT input coupled.
- from 6 km / h to 12 km / h the input coupled transmission works in negative circulating mode

## Simulation results

- at 12 km / h there is a Full Mechanical Point, i.e. the area where the transmission reaches maximum efficiency. Figure 32 shows a sudden loss of performance close to the FMP. This is due to the reversal of rotation of the hydraulic motor and the model chosen for the losses in the hydraulic units.
- from 12 km / h to 30 km / h the transmission works in positive circulating mode

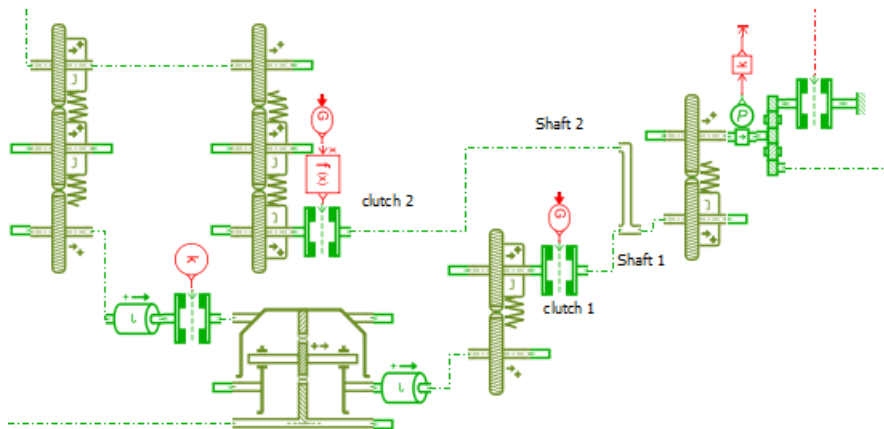


*Figure 33 a) The model shows the shaft 2 with the clutch 2 relative to the pure hydraulic transmission, while the shaft 1 with the clutch 1 are related to the CVT input coupled*

## Simulation results

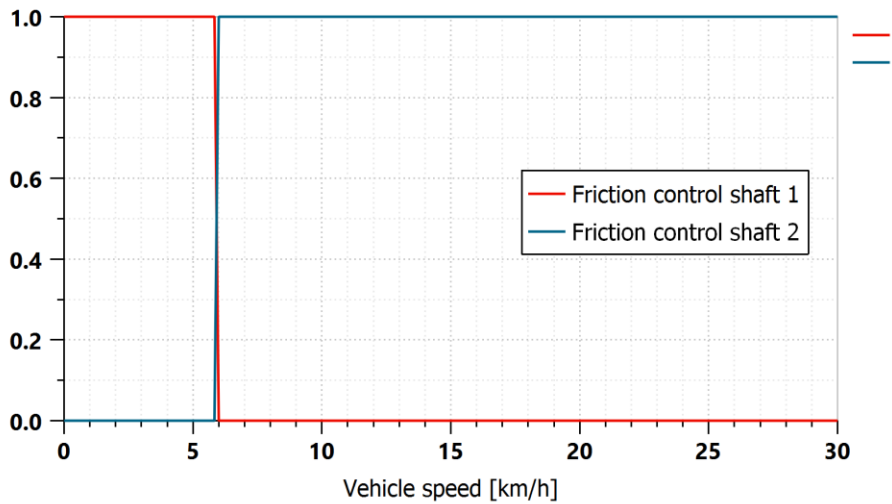


*Figure 33 b) Clutch control signal on shaft 1 and shaft 2 of the transmission*

To evaluate the effectiveness of the transmission model chosen, the CVT HM with hydraulic starting mode was compared first with a fully hydraulic transmission, and then with a CVT input coupled.

Figure 34 compares the total efficiency of the pure hydraulic transmission with the efficiency of the CVT HM with hydraulic starting mode.

## Simulation results

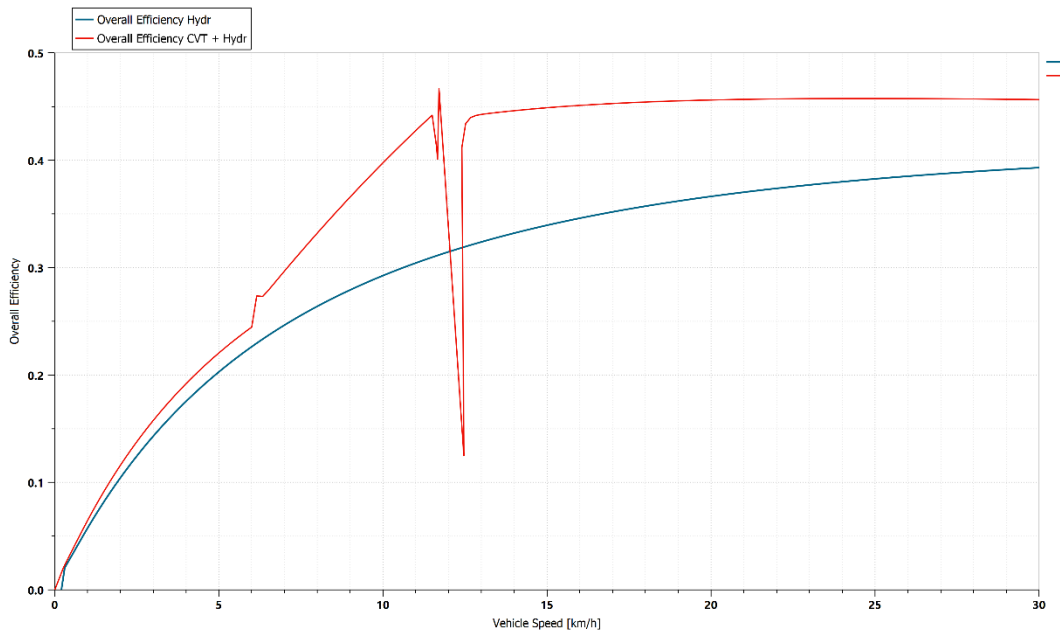


*Figure 34 Comparison of overall efficiency between pure hydraulic transmission and CVT with hydraulic starting mode*

As can be seen from the comparison between the blue curve and the red curve, the CVT with HSM (hydraulic starting mode) transmission has a significantly higher performance, especially after shifting gears. This underlines that simple coupled CVT input has a significantly higher efficiency than pure hydraulic transmission, if high speeds are considered.

So analysing figure 34 it is easy to justify the use of the CVT HM compared to the pure hydraulic transmission, considering that for large stretches of the "mission test", and in particular close to the FMP area there is a greater difference in efficiency by 10%. This difference in performance justifies the use of an input coupled CVT transmission, which from a construction point of view presents greater complexity, especially when considering the use of the planetary gear and the complexity due to the transmission control.

## Simulation results

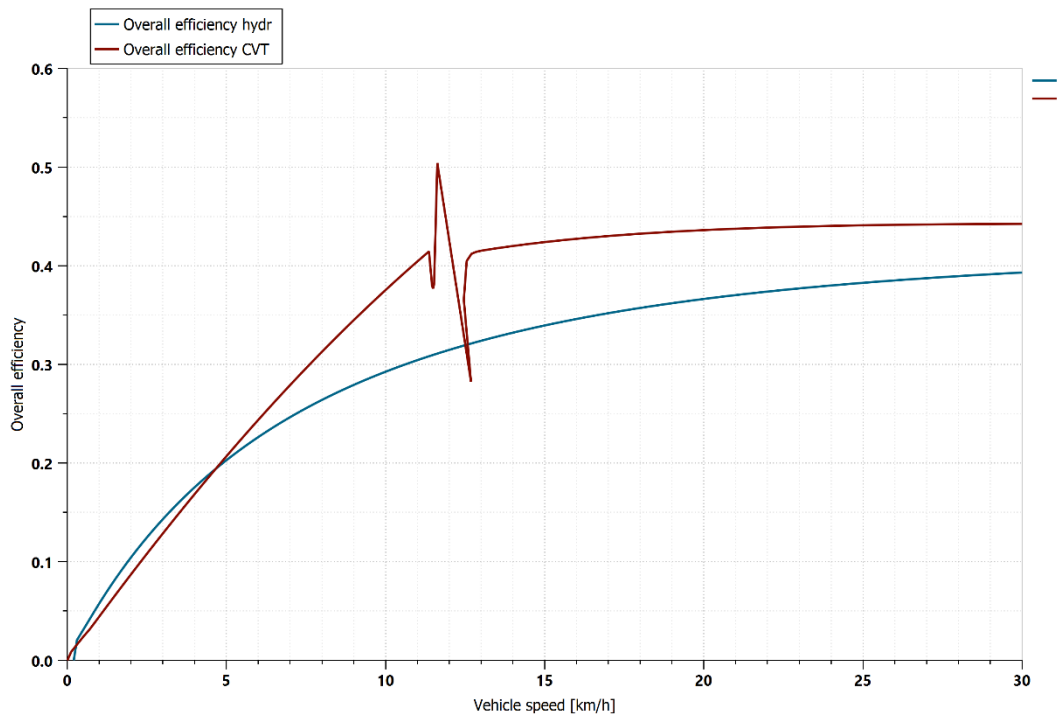


*Figure 35 Comparison of overall efficiency between pure hydraulic transmission and CVT input coupled*

Analysing the trend of the efficiency curves in figure 35, it should be noted that for very low speeds (starting phase), i.e. in the case of negative circulating mode, the CVT input coupled has a lower efficiency than the pure hydraulic transmission. This aspect, which becomes much more interesting if an energy recovery is considered, justifies the use of a multi-range transmission, and in particular in the case examined, the use of a CVT HM with HSM.

Figure 36 shows the comparison between the overall efficiency of the CVT input coupled and the efficiency of the CVT HM with HSM.

## Simulation results

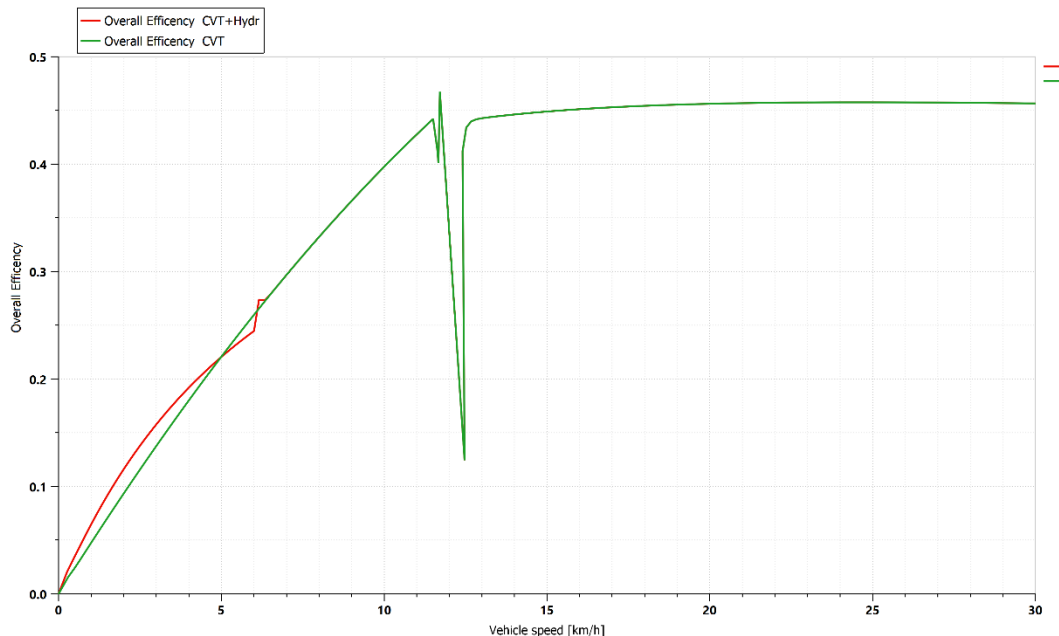


*Figure 36 Comparison of overall efficiency between CVT with HSM and CVT input coupled*

It should be noted that the efficiency of the CVT input coupled, for speeds between 5 km / h and 6 km / h ( $V_{\text{shift}}$ ), has a higher efficiency than the CVT HM with HSM. As mentioned in paragraph 2.4, the choice of the  $V_{\text{shift}}$  was made considering the equality of the displacements of the hydraulic motor obtained from the design calculations. Nonetheless, considering the low displacements of the hydraulic units, it is possible to think of an optimization of the transmission, which can be obtained by changing the  $V_{\text{shift}}$  in order to maintain the efficiency of the CVT HM with HSM always greater than the total efficiency of the CVT input coupled. However, a greater displacement of the hydraulic motor may be required in the transmission starting phase, but this is justified by the improvement of the overall efficiency.

Figures 37 and 38 show the behaviour of the hydraulic units, as a function of the vehicle speed. By observing the fractional displacement of the hydraulic units

## Simulation results

(figure37), as can be expected, is possible to notice that the pump decreases its displacement during the hydraulic starting phase, going from 0 to -0.4, the point where the gear change takes place. In this condition, as already mentioned, the CVT input coupled is engaged, i.e. the transmission will behave like a CVT input coupled. The pump displacement therefore, as for the CVT input coupled, moves from the minimum reached at  $V_{\text{shift}}$  (-0.4) to the zero displacement, the point where the transmission reaches the FMP. Continuing to accelerate, the vehicle goes into power split mode, and the pump displacement moves from zero to its maximum. For this type of transmission, the displacement of the hydraulic motor remains constant throughout its operation.

Analysing the speeds of the hydraulic units (figure 38), it is possible to say that the behaviour between pump and motor is reversed, i.e. the rotation speed of the pump shaft remains constant at the maximum speed of 3500 rpm during transmission operation, while the hydraulic motor accelerates to the  $V_{\text{shift}}$  (gear shift), then decelerates until it reaches zero speed (FMP). At this point when the vehicle accelerates, it switches in power split mode and the hydraulic motor reverses its direction of rotation, reaching the maximum speed of 3500 rpm.

Simulation results

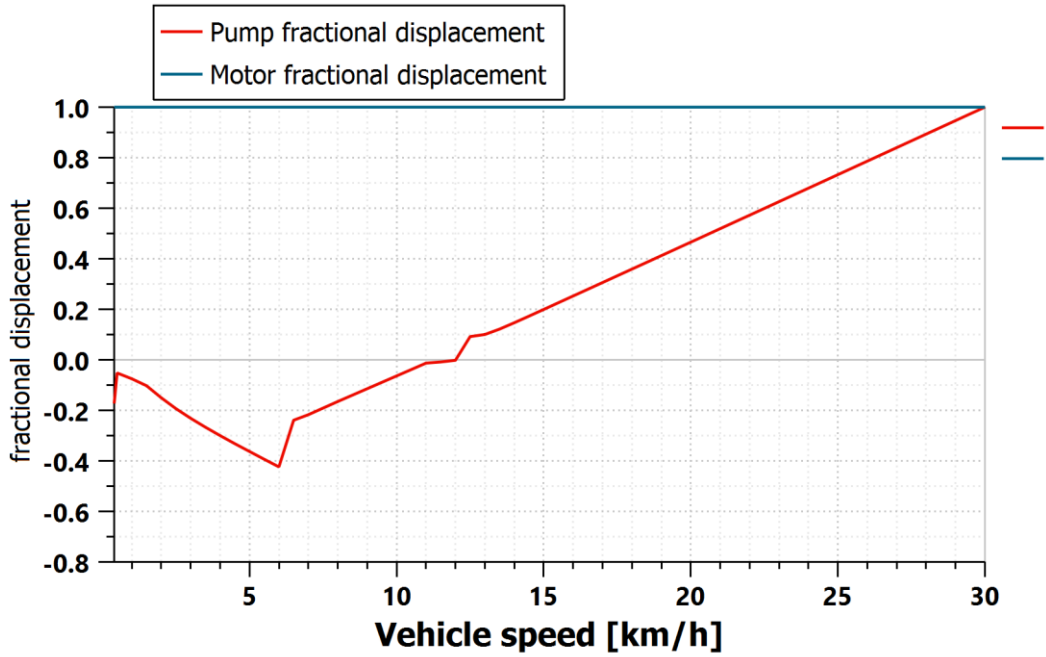


Figure 37 Fractional displacement of hydraulic units

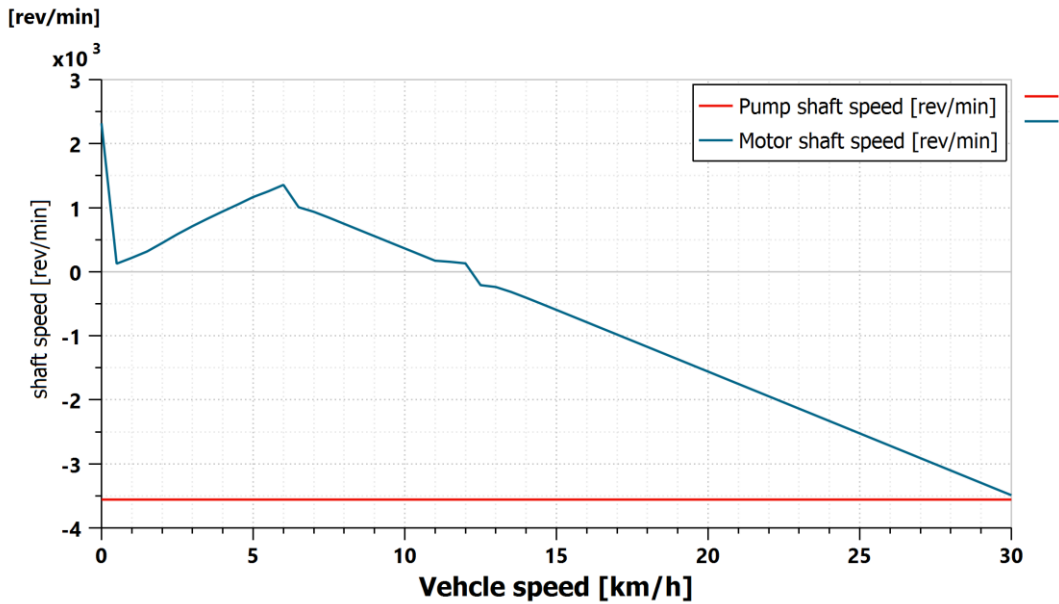
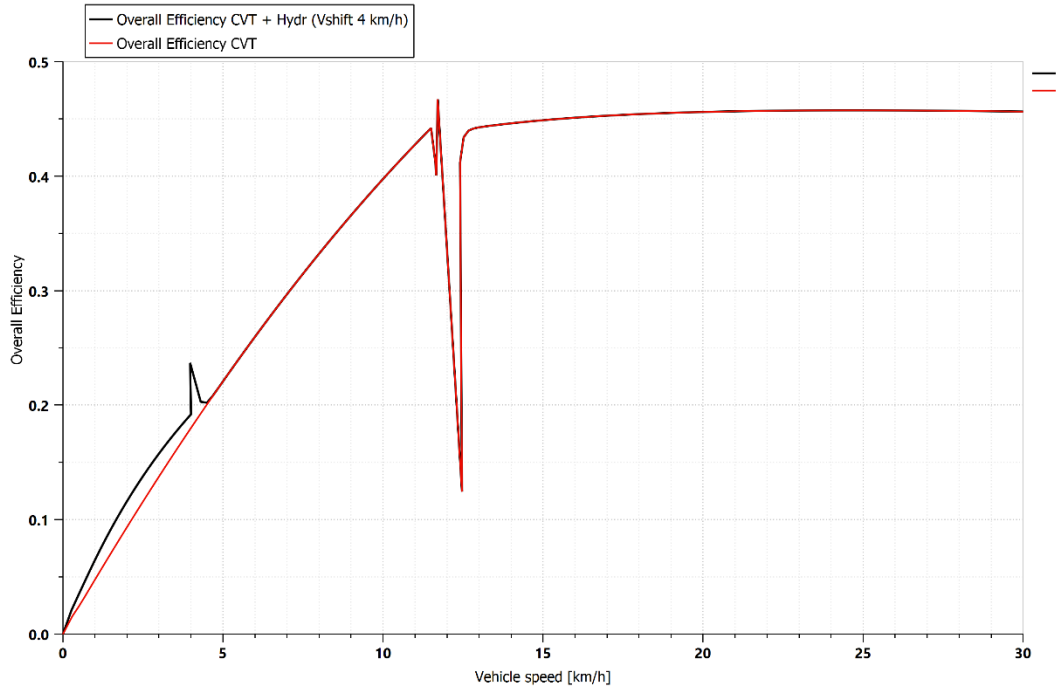


Figure 38 Rotational shaft speed of the hydraulic units

## 4.2 Gear change optimization

As mentioned in the previous paragraph, the variation of the V Shift involves the variation of the displacements of the hydraulic machines and of the transmission ratio of the shaft 2 relative to the pure hydraulic transmission. In particular, decreasing the change speed also decreases the contribution due to the hydraulic motor (considering the pure hydraulic transmission) and therefore the displacement required. However, by decreasing the change speed, the CVT will engage earlier than in the case where  $V_{\text{shift}}$  was equal to 6 km / h. This means that the displacement required by the hydraulic motor in the case of CVT increases considerably. Having to consider the higher displacement, or that required by the CVT, there will be an increase in the displacement of the hydraulic motor of about 10 cc. This however does not represent a worsening in terms of costs and size, if we consider the improvement in the overall efficiency of the transmission, as shown in figure 39.

## Simulation results



*Figure 39 Comparison of overall efficiency between CVT with HSM and CVT input coupled, with Vshift equal to 4 km/h*

Considering figures 39 and 40, obtained respectively for  $V_{\text{shift}}$  equal to 4 km / h and 2 km / h, it is noted that in both cases efficiency has improved. However, choosing a  $V_{\text{shift}}$  equal to 2 km / h means doubling the displacement of the hydraulic motor, and obtaining a speed range in which the efficiency of the CVT HM with HSM is greater than the CVT input coupled, lower than in the case in figure 39.

## Simulation results

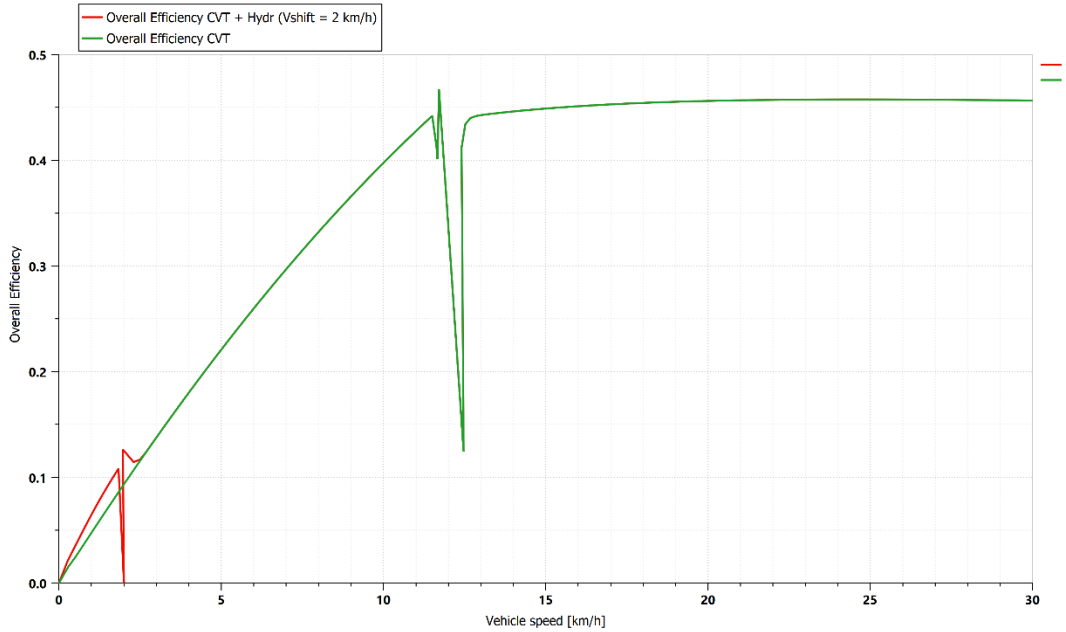


*Figure 40 Comparison of overall efficiency between CVT with HSM and CVT input coupled, with Vshift equal to 2 km/h*

### 4.3 Constant power simulation

By applying a mechanical brake to the transmission (figure 41), it was possible to test the overall efficiency at constant power.

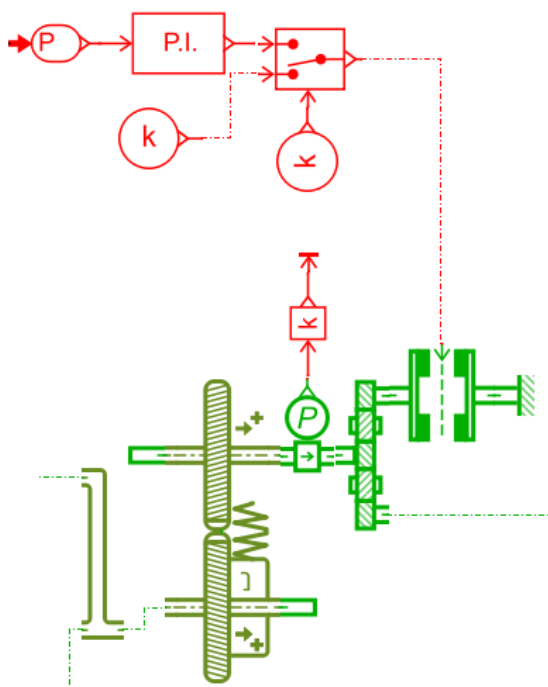
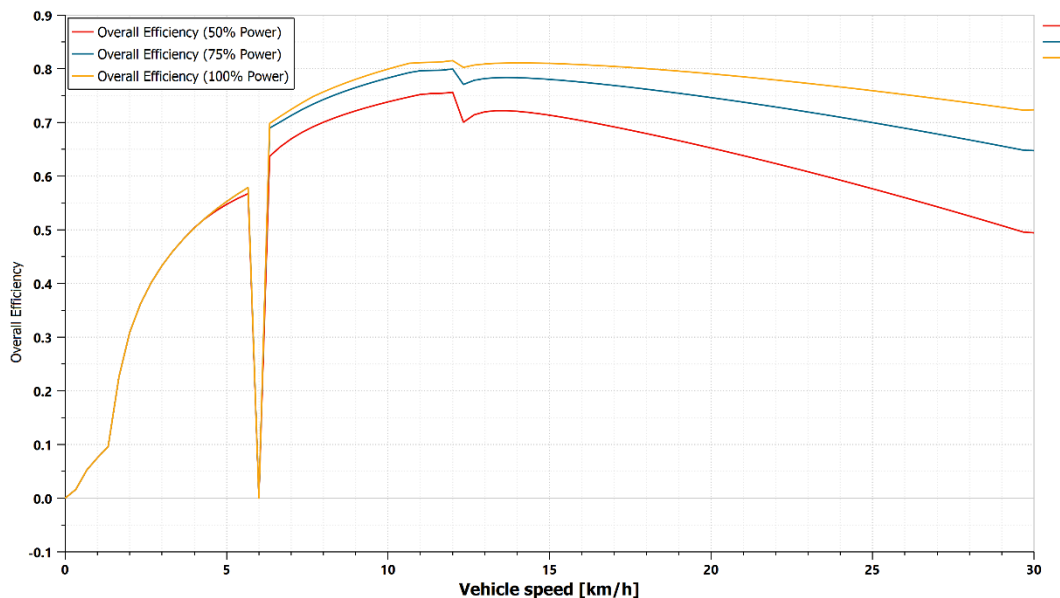


Figure 41 scheme of mechanical brake

As the graph in Figure 42 shows, the efficiency at full load of the transmission reaches a maximum of about 83% at the full mechanical point, and decreases up to 75% which is reached at maximum vehicle speed.

It can be seen that even for partial load, the efficiency remains fairly high. For a partial load of 50% the overall efficiency reaches approximately 75%. However, in this case, analysing the trend of the yellow curve, it is noted that the curve maintains a non-constant trend, losing greater efficiency at maximum speed (50%). This result shows, however, that even for partial load, the CVT HM with HSM transmission maintains overall good efficiency.

## Simulation results



*Figure 42 Overall transmission efficiency with partial load of 50%, 75% and 100%.*

## 4.4 WLTC (Worldwide harmonized Light-duty vehicles Test Cycles)

Not having available data regarding the real work cycle of the street sweeper, in order to evaluate the transmission performance on a real cycle, the WLTC model (figure 43 a) was used, adapting it to the type of vehicle. WLTC is a procedure based on new driving cycles to test the average fuel consumption, CO<sub>2</sub> emissions and pollutant emissions of passenger cars and light commercial vehicles. The WLTC is divided into different classes according to the maximum speed that can be reached by the vehicle. In our case (figure 43 b) the test cycle for class 1 (vehicle up to 60 km / h) has been adapted.

Simulation results



Figure 43 a) WLTC class 1

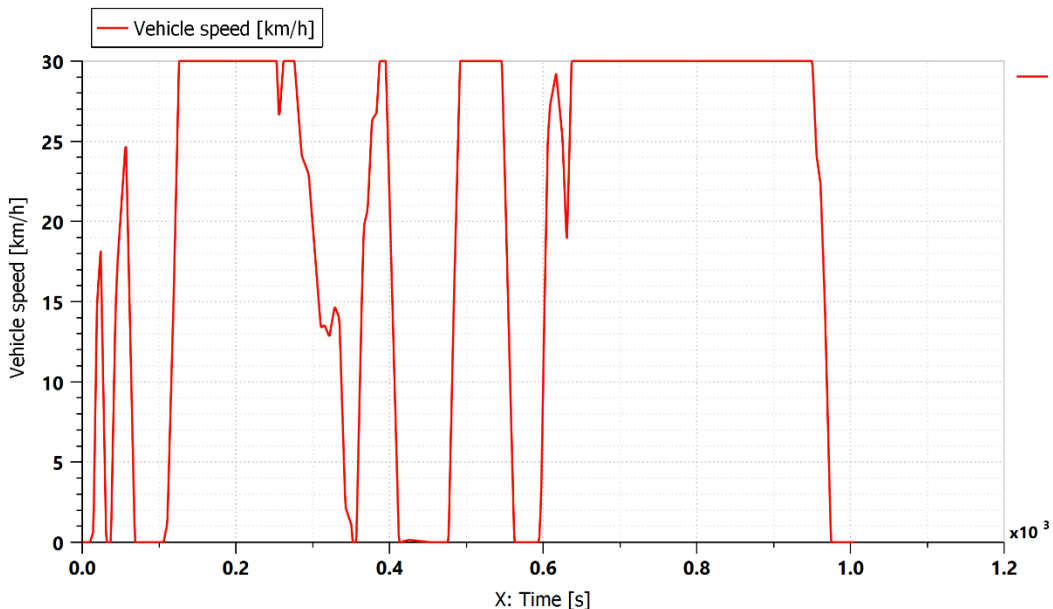
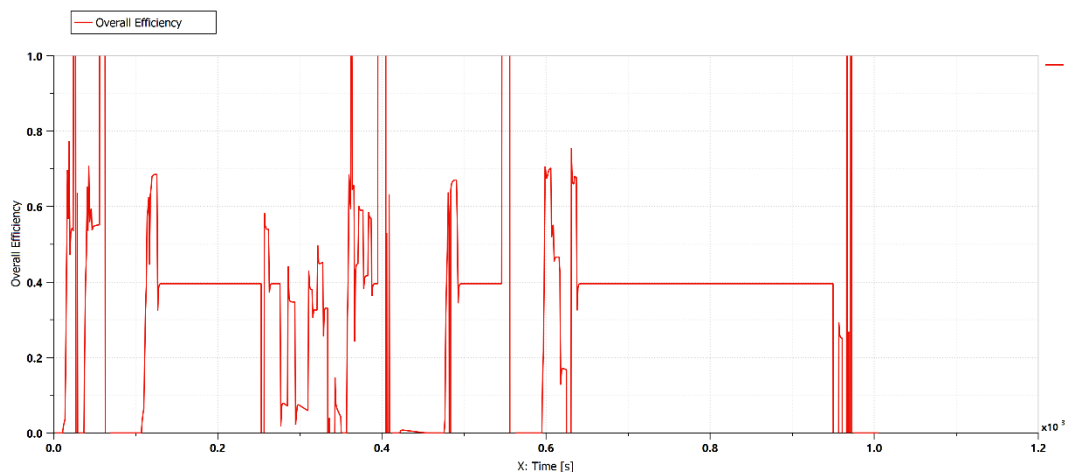


Figure 43 b) Mission profile based on the WLTC, adapted to the characteristics of the street sweeper

## Simulation results

Analysing the transmission efficiency on the mission profile based on the WLTC (figure 44), it should be noted that the average transmission efficiency stands at very low values, around 40% -45%. The peaks that exceed the efficiency are transients due to the gear change, and in particular at the moment in which clutch 1 opens and clutch 2 closes, that weren't modelled in the analysis.



*Figure 44 Overall transmission efficiency during WLTC mission profile*

This behaviour shows that the hydraulic units work at low efficiencies throughout the WLTC cycle, and in particular as can be seen from figure 45 with low hydro-mechanical efficiency.

To better understand the reason behind this behaviour, the amount of power absorbed by the transmission throughout the cycle was analysed.

## Simulation results

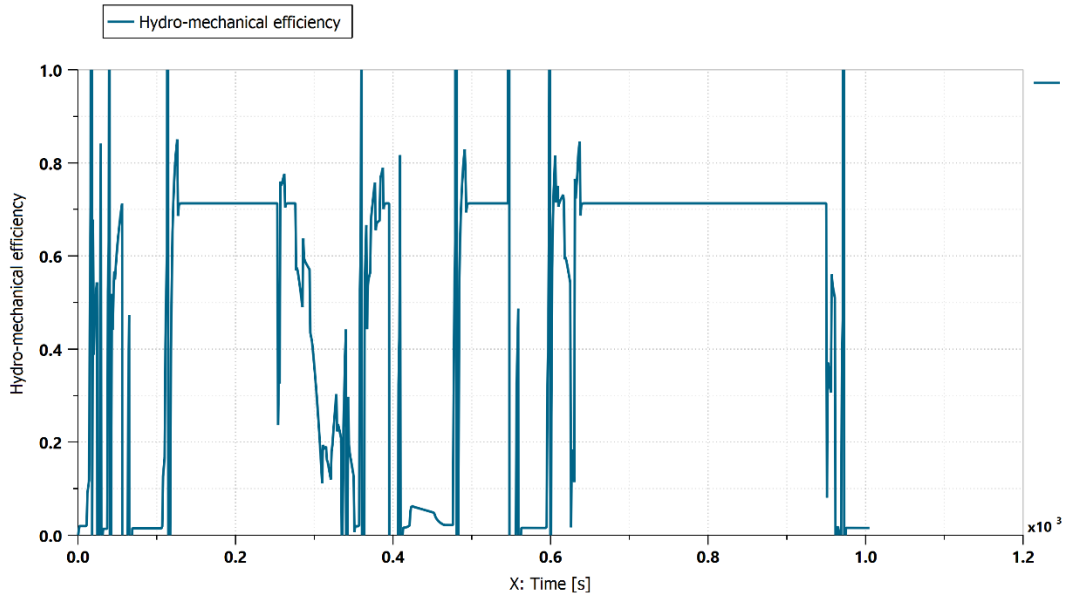


*Figure 45 Hydro-mechanical pump efficiency*

As can be seen from figure 46, the average power absorbed by the transmission during the WLTC cycle is approximately 6-7 kW, much less than the 25 kW potentially deliverable by the ICE. Therefore, working at low power, compared to the one for which the transmission was designed and sized, the hydraulic machines are oversized and therefore work at low efficiency.

## Simulation results

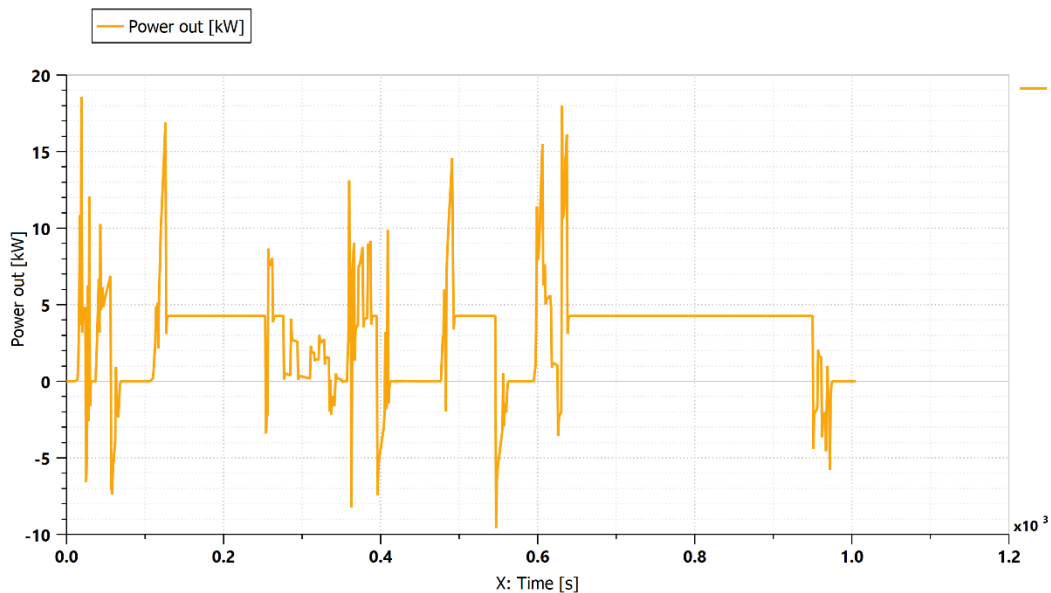


*Figure 46 Power absorbed by CVT HM with HSM during the mission cycle*

A further optimization could be achieved by dimensioning the transmission with 10-12 kW of ICE power, taking into account the part of power absorbed by the secondary users (brushes, etc.).

## 4.5 Simulation of energy recovery system

Figure 47 shows the transmission scheme with the energy recovery system. the ability to recover energy during the braking phase of the vehicle was tested in a class 1 WTLC.

## Simulation results

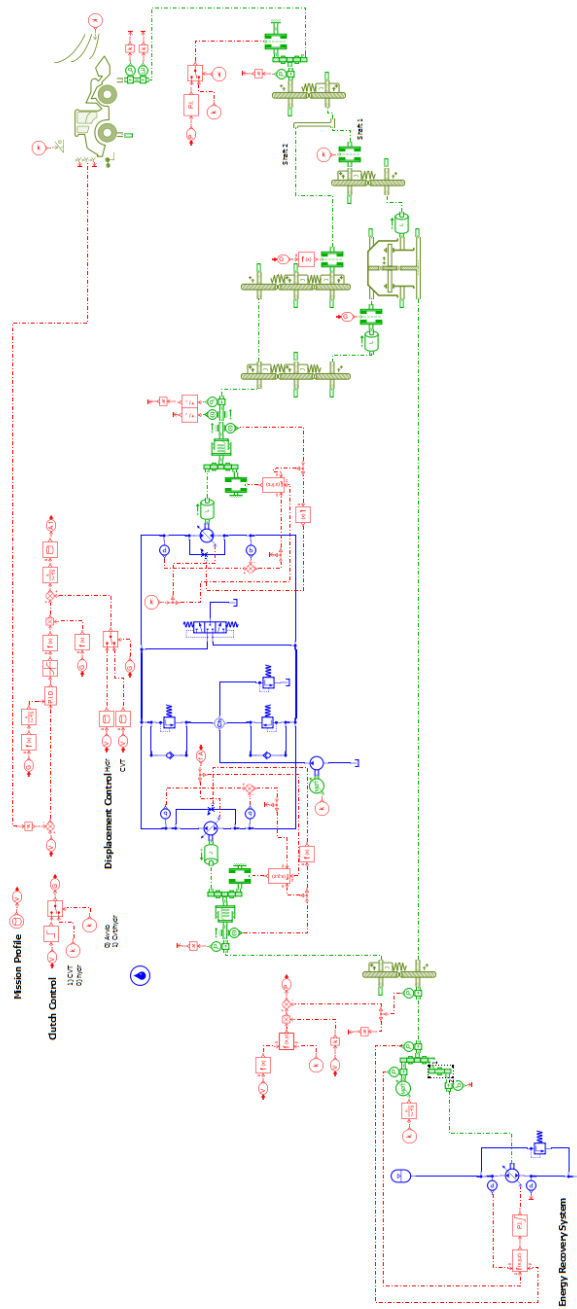


*Figure 47 Scheme of Continuously Variable Hydro-Mechanical Transmission with Hydraulic Starting Mode and Energy Recovery System*

Simulation results

Figure 48 shows the trend of the required power. It's possible to underline that the accumulator, which is considered full when the vehicle is started, manages to deliver hydraulic power only for a first part of the cycle (blue curve) up to a time of about 180 s. At this point the accumulator will be discharged (figure 49) and the power required by the load will be supplied entirely by the ICE (yellow curve).

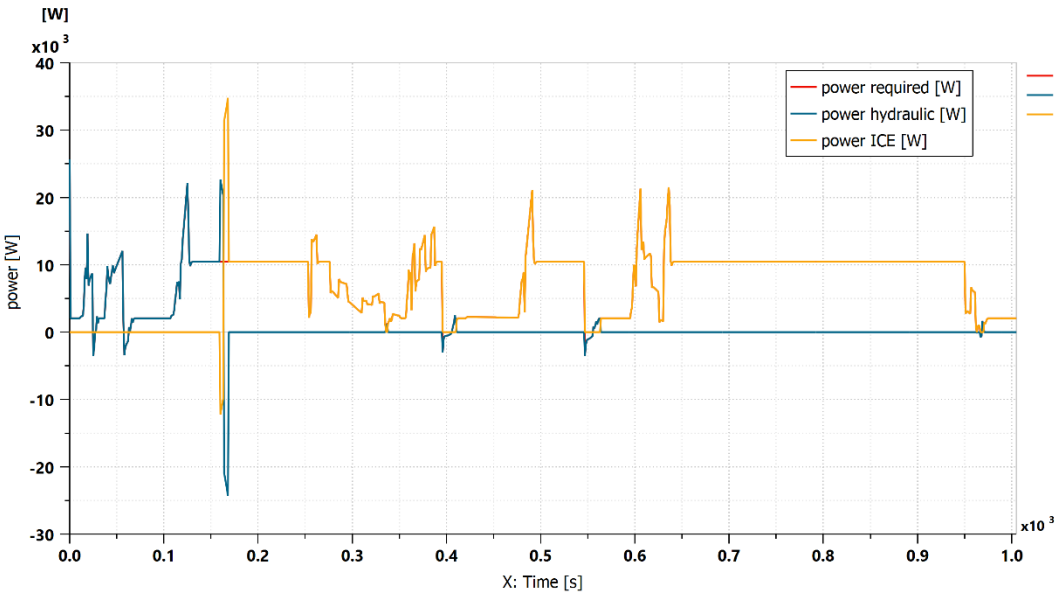
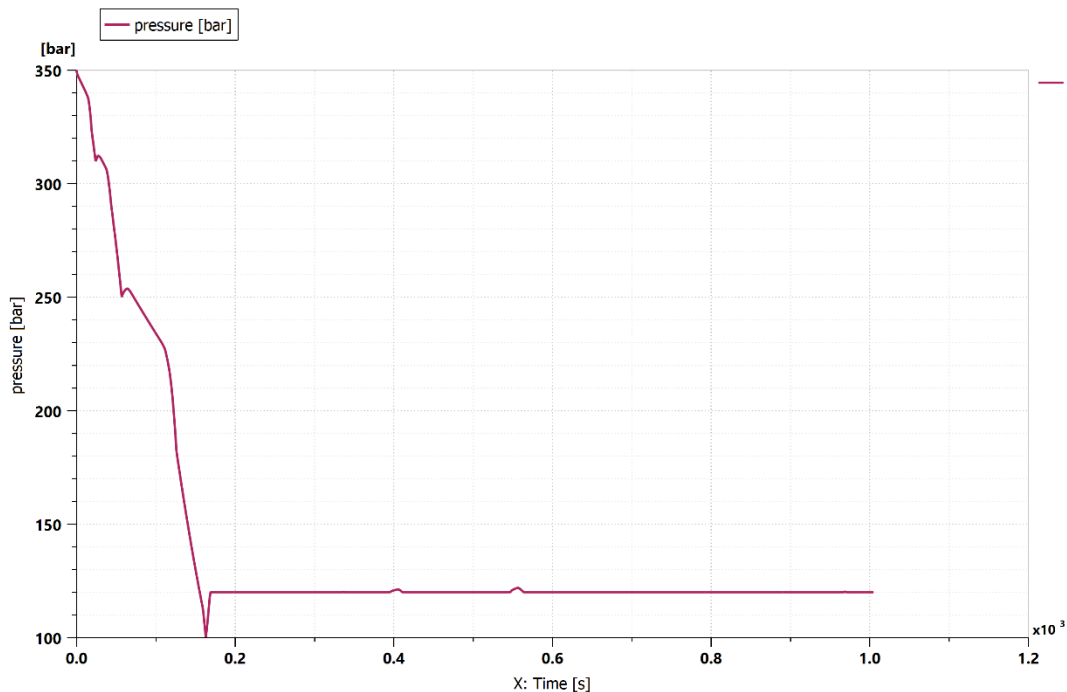


Figure 48 Trend of required power, hydraulic power and ICE power during the test cycle

## Simulation results



*Figure 49 Pressure trend in the accumulator during the WLTC*

It should be noted that the energy recovery system and therefore the pump to support the internal combustion engine no longer attends during the remainder of the cycle. Furthermore, except in a few points, there is no accumulation of energy as shown in figures 48 and 49.

This behaviour shows that a large part of the braking power is dissipated in the gears before reaching the storage system, probably due to the small size of the vehicle, which does not generate enough power when braking to regenerate.

It should also be noted that, despite the poor efficiency of an energy recovery system associated with a vehicle that has a small size and reaches a maximum speed of 30 km/h, the use of an energy recovery system associated with a CVT HM transmission with HSM has an important advantage over the use of an energy recovery system associated with a simple CVT input coupled. In particular, the CVT input coupled

Simulation results

has the possibility of regenerating energy only in power split mode, and cannot regenerate energy in negative circulating mode.

## **Conclusion**

In the first part of this PhD thesis, the application of a hydro-mechanical CVT to a street sweeper was studied. Three different types of transmission were compared:

- a hydraulic transmission
- a CVT input coupled
- a CVT input coupled with hydraulic starting mode.

It has been shown how the application of a HM CVT with HSM allows reaching higher efficiency than the input coupled CVT, as the pure hydraulic transmission maintains in the vehicle starting phase a greater efficiency than the efficiency of the CVT input coupled when is found in negative circulating mode.

This behaviour could be even more evident on vehicles that require more power. The application of an energy recovery system on a vehicle of this type (street sweeper) does not guarantee the possibility of energy storage during braking, due to the low amount of energy generated during braking by the vehicle.

An energy recovery system could be adopted instead on CVT used in heavy duty machines (cranes, excavators, buses), which having a much higher mass than a street sweeper, allow to recover the energy that is not dissipated by the system as heat. In this case the energy recovery could be exploited both for traction and for the handling of auxiliary users (bucket and so on).

A subsequent activity could be to evaluate the application of this type of transmission on vehicles with greater size and power required, and to evaluate the effect of the application of the first hydraulic gear on different architectures, such as output coupled and compound, in the absence and in the presence of an energy recovery system.

## Conclusion

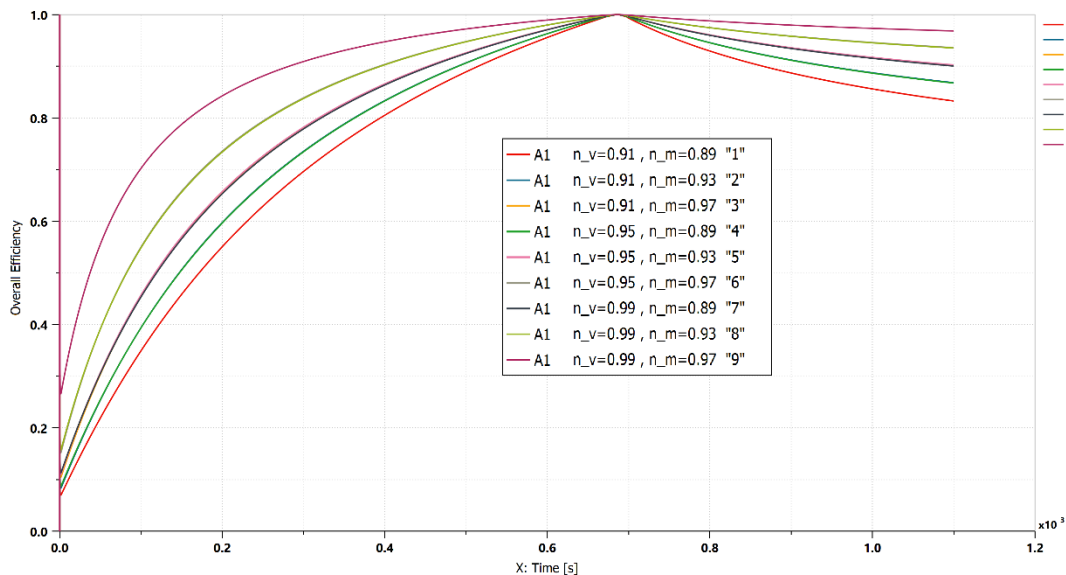


*Figure 50 Trend of the efficiency of an input coupled CVT transmission as a function of the efficiency of hydraulic units*

As has been amply demonstrated in the previous paragraphs, the efficiency of this type of transmission depends almost exclusively on the efficiency of the hydraulic units, having the mechanical part efficiency of about 98-99%. As shown in Figure 50, by varying the volumetric and hydro-mechanical efficiency of the hydraulic units, the overall efficiency of the transmission varies considerably.

Based on these considerations, the second part of the thesis work was focused on the study of innovative coatings applicable in the hydraulic field, with the aim of increasing the volumetric and hydro-mechanical efficiency of the pump and hydraulic motor, and consequently the transmission efficiency as a whole.

## CHAPTER V

### Hydraulic anti-friction coatings

#### 5.1 Definition

As shown in the previous chapters, hydro-mechanical transmissions are subject to a change in efficiency which depends largely on the performance of the hydraulic units. In particular, it has been analysed that the lower efficiency of the transmission occurs when the power recirculates in the hydraulic branch, while the full mechanical point, that is, the point of maximum efficiency, coincides with the moment in which the power passes entirely through the mechanical branch. Since the mechanical efficiency in a transmission is approximately 98-99%, it is clear that it is more important for the designer to concentrate on the efficiency of the hydraulic units, and in particular on the volumetric and hydro-mechanical efficiency of the pump and hydraulic motor.

It is known that one of the main reasons for the hydraulic units' efficiency losses is due to the phenomenon of wear, and in particular in axial piston machines (those used in hydro-mechanical transmissions) wear is generated by the contact that occurs between the cylinder block and the valve plate, and between the slippers and the swash plate.

In particular, as will be analysed in the following paragraphs, the wear is often generated by incorrect lubrication of the rotating parts, due to the starting phase of the vehicle or to phenomenon such as the tilting moment to which the cylinder block is subjected [31]. In order to reduce the efficiency losses due to the friction phenomenon, numerous studies have been carried out in recent years on the coatings adopted on the mechanical parts subjected to wear. Some studies have been carried

out on the analysis of coatings obtained by adding a layer (few  $\mu\text{m}$  or even nm) of material with anti-friction properties on the part to be preserved. Hong et al. [32] have investigated how the surface treatment with TiN plasma coating of the cylinder barrel of axial piston pump, can contribute to the reduction of the friction and wear rate of valve plate in the low speed range. The results showed that the friction torque of the valve plate mated with a TiN-coated cylinder barrel could be reduced to 22% of that with uncoated original one. At the same time, the wear rate of the valve plate could be reduced of 40-50 %.

Korsunsky et al. [33] have studied the evolution of two principal parameters characterising the performance of low friction coatings, namely, the coefficient of friction (COF) and the remnant relative thickness (RT), relating to two types of low friction coatings respectively: conventional thermally sprayed dry film lubricant (DFL) coatings, and novel solid coatings deposited using a mechano-chemical route. Raimondo et al. [34] have presented and analysed the superhydrophobic nanostructured hybrid materials obtained by depositing alumina nanoparticles on copper surfaces via dip coating in  $\text{Al}_2\text{O}_3$  sol.

Other types of coatings include the use of solid lubricating particles, such as lead bronze or the use of bismuth particles; these coatings are very common in the automotive or hydraulic field, even if lead has been partially eliminated due to its toxicity [35].

D'Andrea et al. [36] have analysed the wear behaviour of anti-friction coating made of high-lead bronze on the cylinder block of an axial piston pumps.

Kallio et al. [37] have tested and compared the bronze alloys containing solid lubricants such as bismuth and graphite produced by casting and spray forming. These alloys have been tribologically tested and compared with a lead-bronze alloy. Another kind of anti-friction coating is obtained through surface micro-incisions. Dimples can have different shapes, sizes and arrangements according to the type of

surface characteristics to be obtained, and are made using various techniques such as machining, ion beam texturing, etching techniques and laser texturing [38].

In this thesis work the study of the wear behaviour of a textured bronze lead coating for hydraulic application was addressed, and a study on a highly hydrophobic coating was conducted in order to evaluate the resistance to mechanical loads, maintaining its hydrophobic property.

The novelty of the work consists in the study of the applicability of aforementioned coatings in the hydraulic field in order to improve the performance of the hydro-mechanical CVT.

## 5.2 Friction and Wear in Hydraulic Axial Piston Pump

As previously mentioned, one of the main causes of efficiency loss is due to the phenomena of friction and wear that occur between the moving parts relative to axial piston hydraulic machines. In order to justify the wear due to the contact between the valve plate and the cylinder block [39], and between the slipper and the swash plate [40], it is necessary to analyse the forces and torques acting in an axial piston machine. Basic principle of axial piston pumps is shown in figure 51.

The cylinder bores are arranged on a circle in the cylinder block, where the pistons move in a linear motion. The pistons heads are in continuous contact, through the slippers, with the fixed swash plate, which is arranged at a particular angle  $\alpha$  as shown in figure 51. During one revolution of cylinder block, the pistons execute a full stroke that is a function of swash plate angle  $\alpha$ . The connection of the displacement chamber with the suction and pressure port of the pump is mostly realized through a plane or spherical valve plate. The valve plate has two mostly oval shaped openings, that are connected with the suction and pressure ports of the pump in the housing in which the valve plate is placed.

Axial piston machines are subdivided in two groups according to the principle of the generation of the piston stroke. The piston stroke is generally produced due to the support of the piston on the swash plate. The torque on the cylinder block or on the swash plate emerges according to the design solution of the contact between piston head and the swash plate [11].

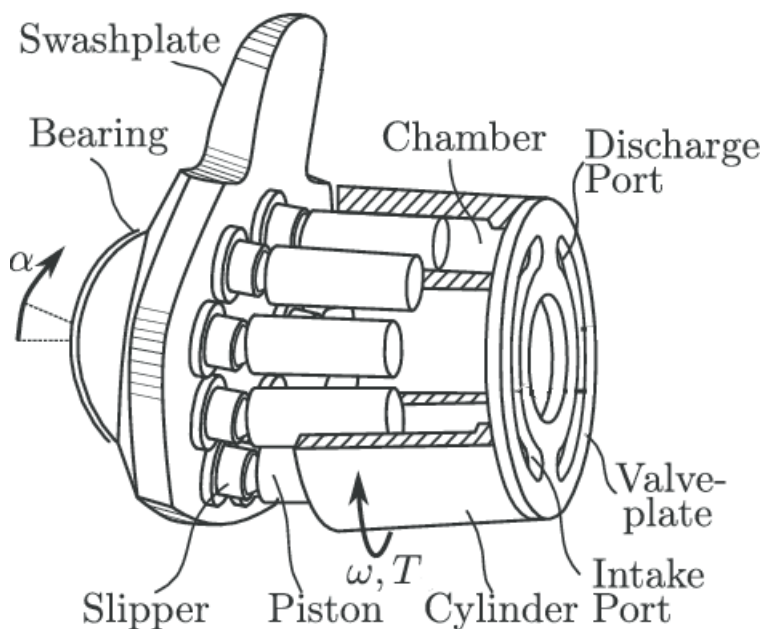


Figure 51 Axial piston pump components [41]

### 5.2.1 Tilting moment acting on cylinder block

Only the forces contributing to the generation of the tilting moment will be considered.

The resultant force acting on the cylinder block is determined from the following forces shown in figure 52:

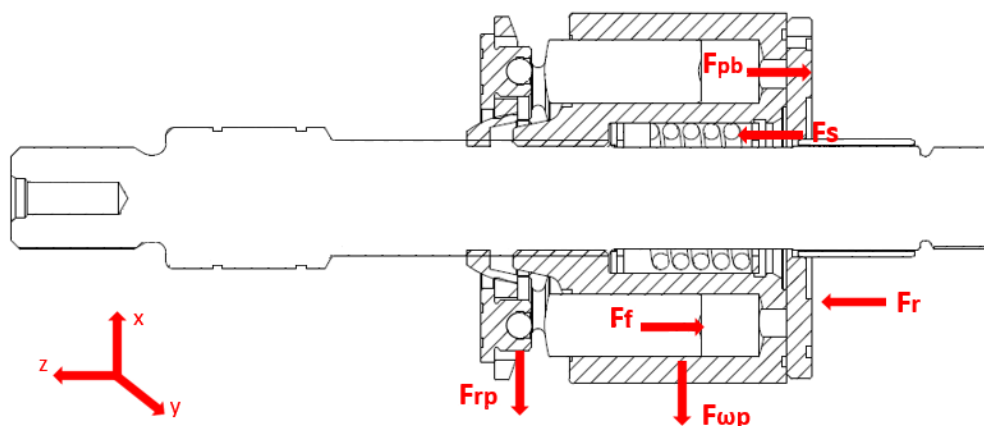


Figure 52 Force exchanged between cylinder block and valve plate

$F_{pbi}$  is the pressure force on the cylinder bottom of the  $i$  th piston:

$$F_{pbi} = -p_i * A_i \quad (5.1)$$

where  $p_i$  is the pressure and  $A_i$  is the area of each piston.

$F_{rp}$  is the piston frictional force transmitted to the cylinder block:

$$F_{rp} = f_k * F_f \quad (5.2)$$

where  $F_f$  is the axial force acting on the head of piston and  $f_k$  is the coefficient of friction.

$F_{\omega p}$  is the centrifugal force of the piston transmitted to the cylinder block:

$$F_{\omega p} = m * a = m * R * \omega^2 \quad (5.3)$$

$F_r$  is the reaction force between the cylinder block and the valve plate to contrast the tipping torque.  $F_s$  is the spring force that acts along the rotational axis of the cylinder

block.  $R$  is the distance between the center of the piston head and the axis of the cylinder block.

These forces acting on the barrel, can be added to a resultant force  $\vec{F} = \sum_{j=1}^n F_j$  and to a resultant moment  $\vec{M} = \sum_{j=1}^n M_j$

In case of simplified computations, the frictional and mass forces can be neglected. The axial force component  $F_z$  of the resultant force acting on the cylinder block is the same as the sum of the pressure forces acting on it.

$$F_z = \sum_{i=1}^n F_{pbi} \quad (5.4)$$

The coordinates of the origin of the force  $F_z$  lying in  $xy$  plane can be determined from the balancing condition between the moment of the resultant force and the sum of the moments of individual forces about the  $x$  and  $y$ -axes.

In case of odd number of pistons there applies in the interval from  $0 < \vartheta < \pi/n$ , where  $\vartheta$  is the rotation angle of the cylinder block:

$$F_z = \sum_{i=1}^{c_1} F_{bpi} = c_1 * F_{bpi} \quad (5.5)$$

where  $c_1 = n/2 + 0,5$  indicates the cylinders on the high pressure side.

In the interval from  $\pi/n \leq 2 * \pi/n$

$$F_z = \sum_{i=1}^{c_2} F_{bpi} = c_2 * F_{bpi} \quad (5.6)$$

where  $c_2 = n/2 - 0,5$  are the number of cylinders on the high pressure side.

## Hydraulic anti-friction coatings

The resultant axial force is a rectangular function and depends on the angular position of the barrel in case of odd number of piston, and changes its origin with the rotation of the cylinder block.

About the expression of the moment, the component  $M_z$  represents the torque, which is the input torque in case of pump operation and output torque in motor operation.

The resultant of the components  $M_x$  and  $M_y$  cause a tilting moment which acts on the barrel influencing the rotating assembly [11].

$$M_{tilting} = \sqrt{M_x^2 + M_y^2} \quad (5.7)$$

This moment  $M_{tilting}$  (figure53) together with the axial force  $F_z$  are mostly balanced by the action of the valve plate, which behaves like an axial hydrostatic-hydrodynamic bearing.

This moment causes a rotation of the cylinder block around the x and y axes during the operation of the pump, and therefore a decrease of the lubricant gap and an increase in the wear [31].

Due to these operating conditions, the use of anti-friction coatings is fundamental to preserve the surface of the block from wear phenomenon.

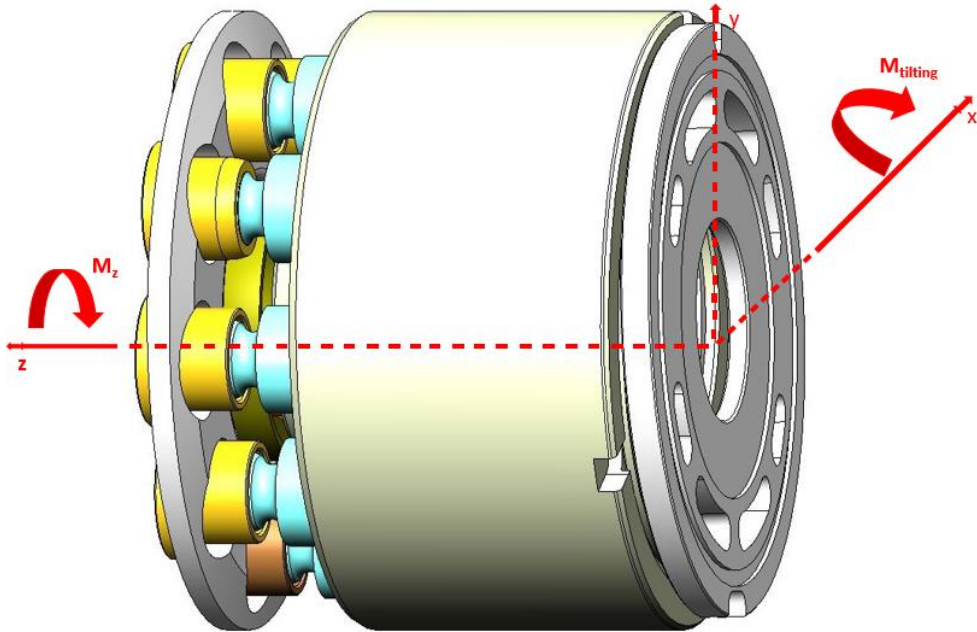


Figure 53 Tipping phenomenon

### 5.2.2 Reaction force on piston slipper

To understand the wear mechanism between slipper and swash plate, it is important to show the forces that act on the slipper (figure 54).

The piston moves into the cylinder bore of the cylinder block, and it is pushed by the high-pressure fluid against the swash plate by means of the slipper pad. Here the reaction force of the slipper pad is given as  $N$ . The supply pressure of the system is assumed to be constant within the high-pressure zone. Viscous damping and friction coefficient for the reciprocation process of the piston are assumed to be identical. The centrifugal force of the piston–slipper assembly is lumped at centroid  $C$ . The normal reaction forces of the piston against the cylinder bore are lumped as  $F_a$  and  $F_b$ , while the relevant friction forces are shown on the contact lines within the cylinder bore as  $f_{Fa}$  and  $f_{Fb}$ , respectively. The total contacting length between the

piston and the cylinder bore is constant during the reciprocation of the piston owing to the special piston profile [40].

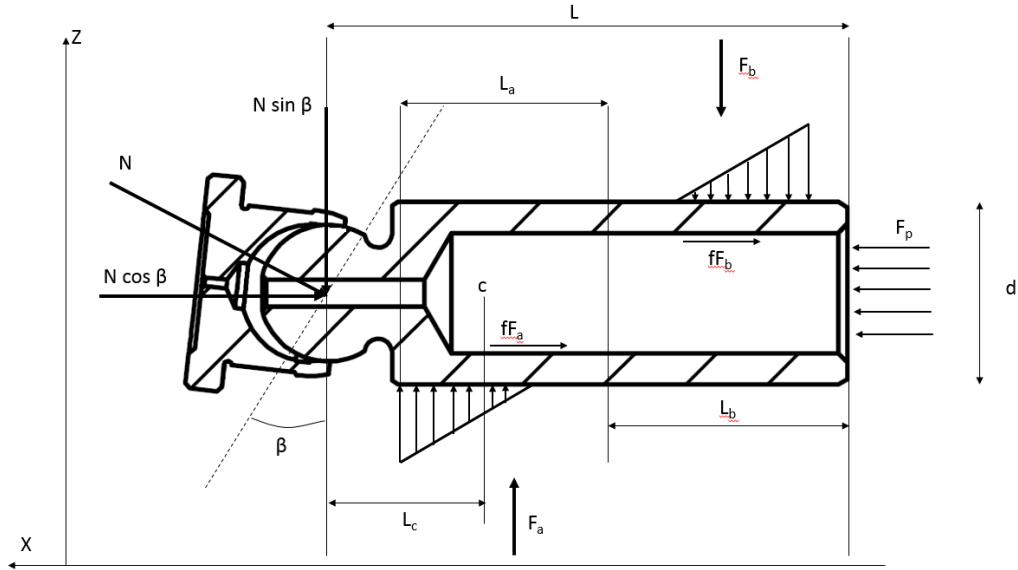


Figure 54 Scheme of force acting on the piston

When the piston draws back the cylinder block completely, we have  $\theta = 0$  (where  $\theta$  is the angular position of the piston) and  $x = 0$ . For the piston inside the high-pressure zone, its position, axial velocity, and axial acceleration can be described as follows:

$$x = R \tan \beta (1 - \cos \theta) \quad (5.8)$$

$$v = R \omega \tan \beta \sin \theta \quad (5.9)$$

$$a = R^2 \omega \tan \beta \cos \theta \quad (5.10)$$

The force equilibrium along the X-axis and the moment equilibrium relative to the centre of the piston joint can be expressed as follows:

$$M_0 = \frac{\pi}{4} d^2 p_s - N \cos \beta - f(F_a + F_b) - Bv \quad (5.11)$$

Where  $p_s$  is a supply pressure,  $B$  is a viscous damping coefficient and  $v$  is the axial velocity of the piston.

$$F_a - F_b - N \sin \beta + mR\omega^2 \cos \theta = 0 \quad (5.12)$$

where  $m$  is the mass of the piston-slipper assembly.

$$F_a \left( L - L_0 + \frac{L_a}{3} \right) - F_b \left( L - \frac{L_b}{3} \right) + mR\omega^2 \cos \beta * L_c + \frac{d}{2} f(F_a - F_b) = 0 \quad (5.13)$$

Furthermore, the two stress-distributing triangles of the piston caused by elasticity deformation are similar to each other:

$$L_a = \frac{3L * L_0 - L_0^2}{6L - 3L_0} \quad (5.14)$$

$$L_b = \frac{3L * L_0 - 2L_0^2}{6L - 3L_0} \quad (5.15)$$

By solving equation (5.8)– (5.15), the reaction force ( $N$ ) of the slipper can be obtained as follows:

$$N = \frac{\frac{\pi}{4} d^2 p_s - mR\omega^2 \tan \beta \cos \theta + fmR\omega^2 \cos \theta * K - BR\omega \tan \beta \sin \theta}{\cos \beta + f \sin \theta * Z} \quad (5.16)$$

## Hydraulic anti-friction coatings

Where K and Z are respectively:

$$K = \frac{3(L - L_c)}{\frac{L_0 + L_a}{L_0 - 2}} \quad (5.17)$$

$$Z = \frac{3L}{\frac{L_0 + L_a}{L_0 - 2}} \quad (5.18)$$

In order to reduce friction and wear in the relative motion parts of the axial piston hydraulic units, the study of textured coatings and hydrophobic coatings was studied, and their possible application in the hydraulic field.

## 5.1 Texturing surface

As said previously, in most engineering applications, and in particular in hydraulic field, the reduction in friction and wear is of great importance to reduce energy losses and to the extension of component life. One of the most studied and applied techniques in recent years to reduce friction and wear is surface texturing. Many techniques can be used for surface texturing including ion beam texturing, etching, laser texturing, and different forms of surface texturing can be realised for this purpose, for example, waves, asperities, and dimples.

Surface Laser Texturing (LST) to produce micro-dimples is the most applied technique, and has been used in this work. Micro-textured surfaces can find application in fluid power systems like seals, pumps, and valves to significantly reduce friction and wear in these systems [42].

Several cases of surface texturing application in hydraulic field are present in literature.

The friction losses of a bent axis type hydraulic piston pump are studied by Hong et al. [43], aiming at finding out which design factors influence its torque efficiency most significantly. It is shown that the viscous friction forces on the valve plate and input shaft bearing are the primary cause of the efficiency losses of the bent axis type pump, while the friction forces and moments on the piston are of little significance. Therefore, if the viscous friction forces on the valve plate are reduced, the torque efficiency can be improved largely.

Patterson et al. [44] have investigated the potential of surface textures to improve the friction at the piston/roller contact in hydraulic motors at low speed and high pressure.

An important feature of the surface texturing technique is that the micro-dimples act as a "reservoir" for lubricant in the cases of starved lubrication condition, but act as a hydrodynamic bearing in the cases of full or mixed lubrication condition [45].

Another fundamental aspect is the "micro-trap" feature, which allows capturing the abrasive particles that can be generated in the presence of abrasive wear.

### 5.3 Hydrophobic materials

Friction and wear depend mainly on roughness, which randomly distributes in surfaces produced by conventional methods. However, many functional biological surfaces have a structured roughness to confer exceptional properties. For example, lotus leaves possess important superhydrophobic properties. Therefore, by functionalising the surfaces of components subject to friction, it is possible to improve the efficiency of the tribological systems.

Bio-inspired surfaces are of interest thank to their particular properties such as self-cleaning, anti-fouling, anti-smudge, anti-fog and oil-water separation.

From the tribological point of view, the most important property to analyse is the wettability of the surfaces, which is the ability of a liquid to adhere to a surface. The wettability depends on the interface interaction between the liquid and the solid, in particular the behaviour of the terminal groups of the surface molecules. It is characterized by the contact angle and the rolling angle (figure55).

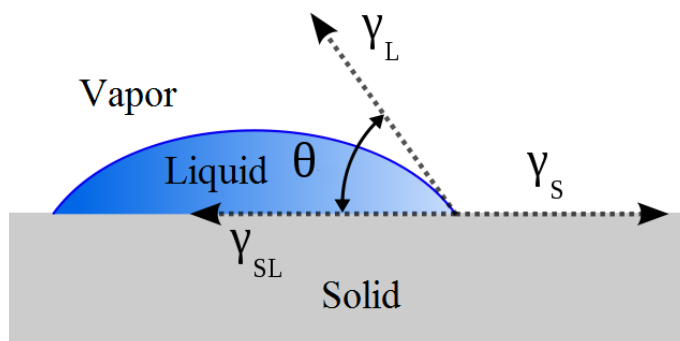


Figure 55 Wetting behaviour of a droplet on the solid surfaces [46]

## Hydraulic anti-friction coatings

The contact angle is the angle between the tangent to the liquid-gas interface and the tangent to the solid surface at the solid-liquid interface. A super-hydrophobic surface minimizes the contact between the drop and the solid, so the value of the contact angle is a measure of the hydrophobicity of the surface: generally, the super-hydrophobic materials have contact angles  $\theta$  greater than  $150^\circ$ .

Therefore, the contact angle provides information on the static equilibrium of the surface.

The rolling angle is the minimum angle whose surface must be inclined to start the motion of the drop, and its value is less than  $10^\circ$  in super-hydrophobic materials.

The rolling angle is linked to the hysteresis of the contact angle, i.e. the difference between the contact angle on the back  $\theta_r$ , and that on the front of the drop  $\theta_f$ , when the surface is inclined (figure 56b).

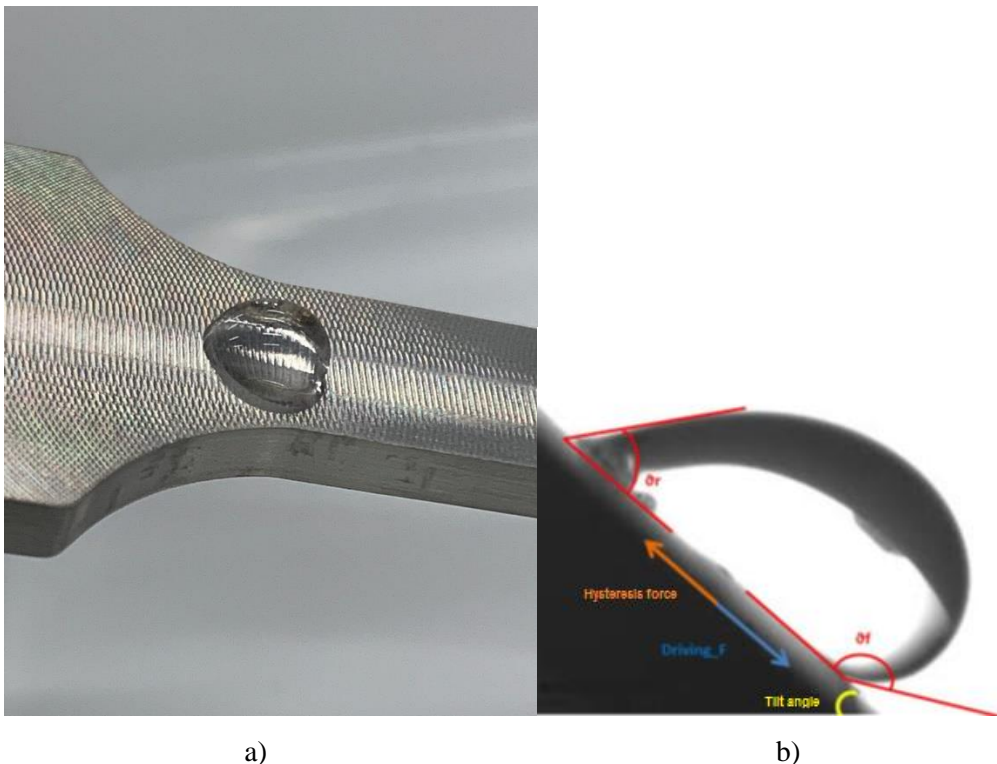


Figure 56 Rolling of the drop on the inclined surface [46]

Chemical compositions of functional polymers determine the surface free energy and it is important role in achieving the desired wettability, and then the property of super-hydrophobicity/ super-oleophobicity. However, super-hydrophobicity can be found in many biological materials surface, such as rose petals, lotus leaves and butterfly wings; the super-oleophobicity is extremely rare, because oils and other organic liquids usually possess lower surface tension compared to water. For this reason, is much more difficult to fabricate super-oleophobic materials than super-hydrophobic ones.

There are many methods for creating bio-inspired surfaces, such as casting, etching, polymerization, pyrolysis, sol-gel etc. In particular, sol-gel technique is one of the most used to realize organic/inorganic nanomaterials. For example, Rao et al. [47] have obtained super-hydrophobic copper substrate, using a sol-gel deposition method. The hydrophobic coating was prepared with methyltriethoxysilane (MTES), methanol (MeOH) and water.

To enhance the anti-friction capacity of the surface, Ou et al. [42] have fabricated a super-hydrophobic coating texturized on copper substrate by combining a two-step surface texturing process. Raimondo et al. [48] have studied the wetting behaviour and durability of amphiphobic aluminium alloy surfaces, obtained by sol-gel route, in a wide range of environmental conditions. Thanks to the appropriate combination of structural modifications and alteration of surface chemistry, has been revealed a high repellence against polar and non-polar liquids. Da Silva et al. [49] have investigated the initial surface treatment conditions on 5052 aluminium alloy, to evaluate their influence on obtaining super-hydrophobic surfaces with anticorrosive properties in saline medium.

Rizzo et al. [50] have shown the experimental results obtained using a nano-coating applied to the slippers of an axial piston pump to reduce the friction losses in order to improve the pump overall efficiency.

A relevant issue that requires further attention is the assessment of the degradation of the hydrophobic properties of the coating during service life due to mechanical stress. The potentially poor mechanical durability of hydrophobic coated surface restricts the wide use of the material in practical applications. Thus, many studies have been carried out to develop hydrophobic coatings with improved mechanical durability [51]–[53].

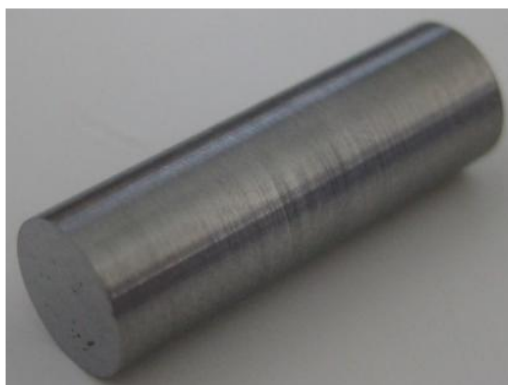
In such a context, the aim of this work is to assess the hydrophobicity stability of fluoro-alkyl silane coating on aluminium substrate, under mechanical tests (e.g. scratch and tensile test). Morphological analysis, performed by confocal optical and scanning electron microscopy was performed to evaluate the damage of the coating at varying stress testing conditions. A relationship between coated surface damaging induced by varying mechanical stresses and wettability behaviour was addressed. Furthermore, the effect of tooling the aluminium substrate was evaluated on the coating wettability performances and stability.

## CHAPTER VI

### Materials and Method

#### 6.1 Texturing surface analysis

The tribological tests were performed by using reciprocating tester. The tribosystem consists of the stationary sample (counter-specimen) pressed at the required load, against the cylinder sample (specimen) performing reciprocating motion. The coefficients of friction and wear were calculated using a tribometer in the configuration pin-on-disc (CETR UMT-3), according to ASTM G99-05 (2010). A cylinder pin (figure57a) of 100Cr6Steel (diameter 6.0 mm, length 20.0 mm) is placed in contact with a known and regulated vertical load (constant) on the surface of the discs (figure57b). From the measurement of the lateral force, it is possible to obtain the coefficient of friction, by the ratio between the lateral and vertical force.



a)



b)

*Figure 57 a) the cylinder pin of Steel 100Cr6 b) bi-metal disk*

The tribometer is shown in figure58

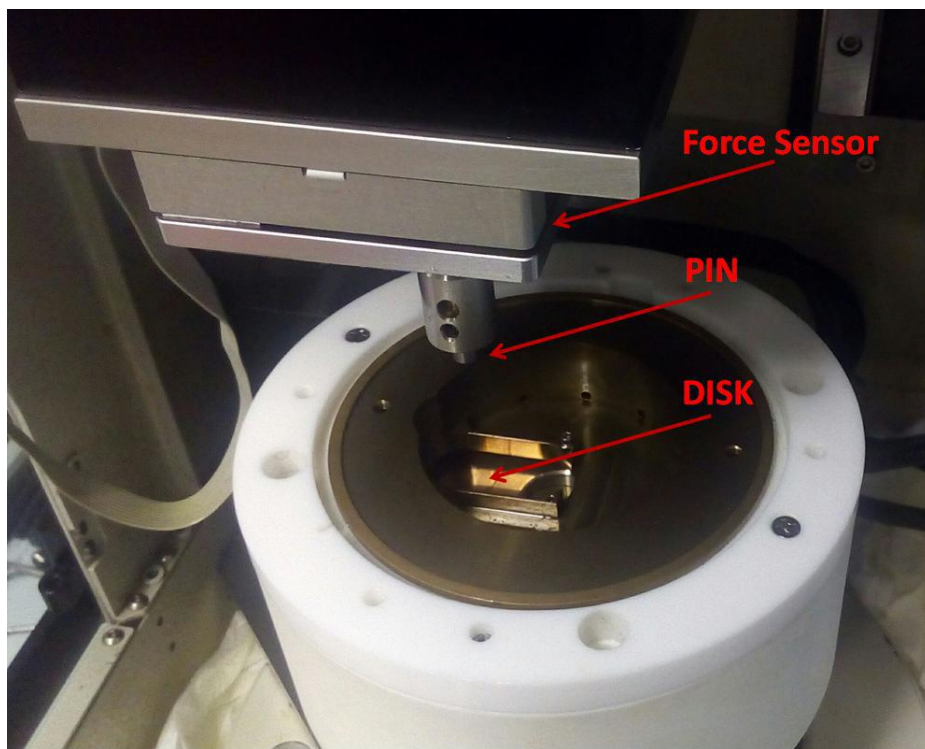


*Figure 58 Tribometer system (CETR UMT-3)*

The tribological tests are performed in the full lubricant bath. The oil lubricant used was the LI-HIV 46 (viscosity index 175). It's used in a hydraulics machine, such as pumps and motors. The table 6 shows the characteristics of the lubricating oil

*Table 6 LI-HIV 46 oil parameters*

Parameters	Value
Density at 20 C °	46 kg/m <sup>3</sup>
Viscosity at 40 C °	46 cSt
Viscosity at 100 C °	9 cSt
Viscosity Index	175
Freezing C°	-35
Flammability C°	210

## Materials and method

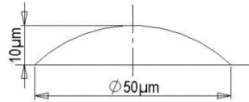
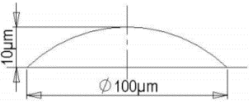
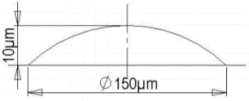
The temperature system is constituted by a thermocouple immersed in the oil bath. The test parameters are shown in table 7.

*Table 7 Tribological test parameters*

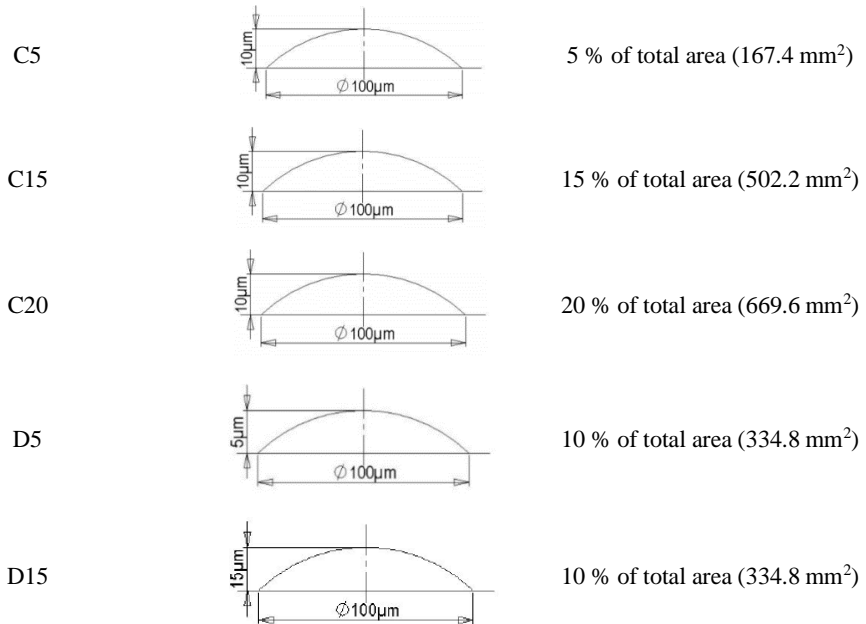
Parameters	Value
Vertical load	706.8 N
Contact pressure	25 MPa
Rotation speed	2000 rpm
Oil temperature	$\cong 70\text{ C}^\circ$
Time	10 min
Lubrication	Full

The micro-structured surface on bi-metal cylinder disk samples have been realised through the use of surface laser texturing technique. Nine typologies of texture, varying diameter, depth, and density of the dimples on the surface have been produced. The specifics of the different kind of samples are reported in table 8.

*Table 8 Specific of texture parameters*

Sample Name	Typology of Texture	Density Area [mm <sup>2</sup> ]
A	As produced	/
B50		10 % of total area (334.8 mm <sup>2</sup> )
B100		10 % of total area (334.8 mm <sup>2</sup> )
B150		10 % of total area (334.8 mm <sup>2</sup> )

## Materials and method



Totally were realised 36 samples that can be classified in four classes denominated with the letters A, B, C, D. As shown in table 8, the samples A is as produced, without any kind of texture; the samples B (Figure 59a-59b-59c) were produced changing the diameter of dimples, keeping fixed depth and density of dimples; samples C (Figure 60a-60b-60c) were made changing the density, keeping unchanged depth and diameter of dimples. The latter kind of samples D (Figure 61a-61b), were produced changed only the depth of the dimples.

The surface laser texturing was realised on lead-bronze (EN CC496K) specimens. This material is typically applied in anti-friction coating used in hydraulic industry. In this case, is used as a coating for valve plate and cylinder block in axial piston pumps.

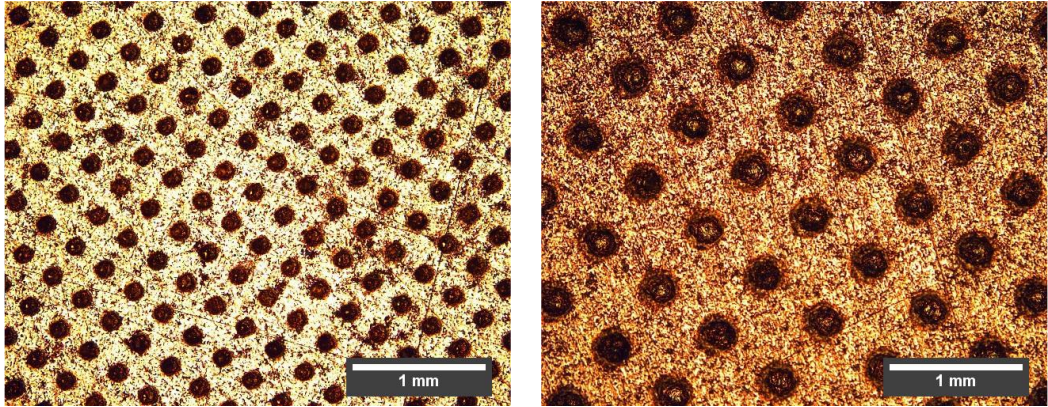


*Figure 59 a) B50 sample; b) B100 sample;*

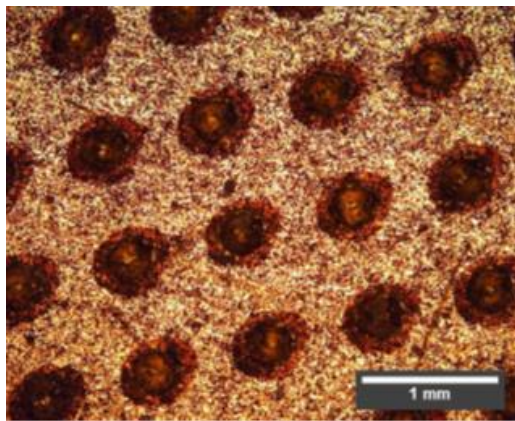


*Figure 59 C) B150 sample*

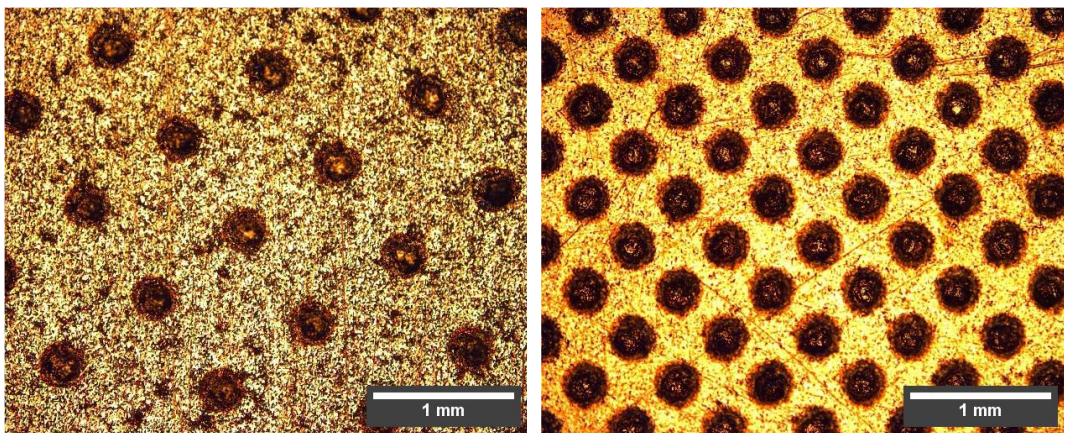


*Figure 60 a) C5 sample; b) C15 sample;*

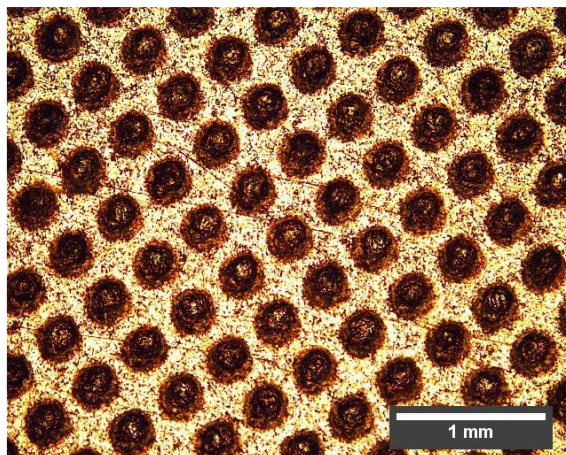


*Figure 60 c) C20 sample*

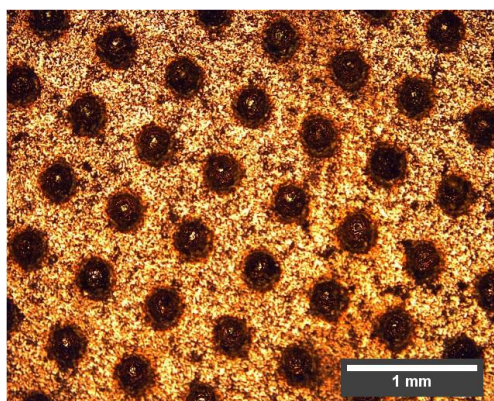
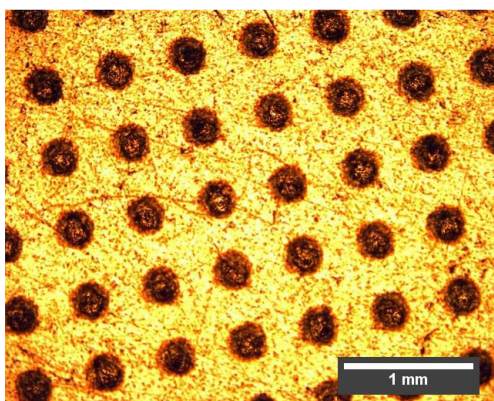


*Figure 61 a) D5 sample; b) D15 sample*

A failure analysis was performed to characterize the behaviour of the dimples and the microstructure of the bronze alloy subjected to tribological test, through the use of optical microscope (OM), scanning electronic microscope (SEM), equipped with an EDS probe, and confocal microscope.

The optical microscopy was carried out by means a LEICA stereomicroscope, while the SEM microscopy was carried out by HITACHI TM3030PLUS. Confocal microscopies were performed with 100X lens whose characteristics are shown in the table 9 and table 10, that reports the set-up parameters used for the confocal scans.

*Table 9 Characteristic parameters of 20x and 100x lenses*

<b>Characteristic parameters</b>				
Objective	NA (numerical aperture)	WD (Working distance)	Pixel size (µm)	Min. range (µm)
100x	0.90	0.27	0.16	4

*Table 10 Set-up parameters of confocal scan*

<b>Set-up parameters</b>									
<b>Untested</b>					<b>Tested</b>				
Name	Objective	Zscan	Speed	Area	Name	Objective	Zscan	Speed	Area
A	Epi 100X-L	20 µm	1x	3,97x1,45 mm <sup>2</sup>	A	Epi 100X-L	40 µm	1x	636,61x 447,25 µm <sup>2</sup>
B50	Epi 100X-L	20 µm	1x	3,97x1,45 mm <sup>2</sup>	B50	Epi 100X-L	40 µm	1x	636,61x 447,25 µm <sup>2</sup>
B100	Epi 100X-L	20 µm	1x	3,02x2,98 mm <sup>2</sup>	B100	Epi 100X-L	40 µm	1x	636,61x 447,25 µm <sup>2</sup>
B150	Epi 100X-L	30 µm	1x	3,02x2,98 mm <sup>2</sup>	B150	Epi 100X-L	100 µm	1x	636,61x 447,25 µm <sup>2</sup>
C5	Epi 100X-L	20 µm	1x	3,02x2,98 mm <sup>2</sup>	C5	Epi 100X-L	40 µm	1x	636,61x 447,25 µm <sup>2</sup>
C15	Epi 100X-L	30 µm	1x	3,02x2,98 mm <sup>2</sup>	C15	Epi 100X-L	40 µm	1x	636,61x 447,25 µm <sup>2</sup>
C20	Epi 100X-L	120 µm	1x	3,02x2,98 mm <sup>2</sup>	C20	Epi 100X-L	40 µm	1x	636,61x 447,25 µm <sup>2</sup>
D5	Epi 100X-L	30 µm	1x	3,02x2,98 mm <sup>2</sup>	D5	Epi 100X-L	40 µm	1x	636,61x 447,25 µm <sup>2</sup>

D15	Epi 100X-L	30 $\mu\text{m}$	1x	3,02x2,98 $\text{mm}^2$	D15	Epi 100X-L	40 $\mu\text{m}$	1x	636,61x 447,25 $\mu\text{m}^2$
-----	------------	------------------	----	----------------------------	-----	------------	---------------------	----	--------------------------------------

## 6.2 Hydrophobic surface analysis

### 6.2.1 Dog-bone samples

Dog-bone aluminium specimens with hydrophobic silane coating were tested. The specimens were differently tooled on both sides (Figure a). One side was kept "as received", while the other side was worked on a lathe, to increase the fixing of the hydrophobic coating. In Figure b, the sample shape and dimensions are drawn.



This suffix is followed by one or two letters. The first one is related to tooling surface: “R” and “W” are referred to as received and worked surface, respectively. Furthermore, possibly a “S” letter can be also present if the surface was silanized. Therefore, the A-AR batch indicates the as received surface without silanization. Analogously, A-WS is referred to a silanized worked surface.

*Table 12 Sample Summary*

Code	Surface	Silanization
A-R	As received	No
A-RS	As received	Yes
A-WS	Worked	Yes

## 6.2.2 Wettability measurements

The surface wettability of the prepared aluminium samples was studied through the static contact angle technique using a sessile drop measurement instrument (optical tensiometer Attension Theta by Biolin Scientific). For this purpose, 3  $\mu\text{l}$  droplets of distilled water were set along a straight longitudinal line on the central part of the tensile specimen surface. All the tests were carried out in atmospheric condition at 25 °C. The drop image was taken by micro CCD camera. Then, this image was automatically analysed by a suitable Attension software with a droplet profile fitting (Young-Laplace) in order to obtain the contact angle between the water droplet and the surface of each sample before and after the scratch or the tensile tests (details concerning these two experimental set-up are reported in 2.3.2 and 2.3.3). At least five replicas for each measurement were carried out.

## 6.2.3 Scratch Test

## Materials and method

To study the stability of the silane coating under stress, scratch and tensile tests on dog-bone samples were performed.

Scratch tests were carried out, in accordance with ASTM D3363, using a pencil hardness tester (Figure 63). The aim of such test was also the evaluation of mechanical response of the coating in a scenario that can happen during on-site application, i.e. hard debris particles coming from wear mechanism or dust, with the contemporary external load due to working conditions.



*Figure 63 Pencil hardness tester*

The scratch tests were performed with 3 different pencil hardness. For each degree of hardness, the test was repeated five times, impressing a track of about 6.5 mm with a constant speed of 1 mm/s. Furthermore, through the additional blocks it was possible to test the coating with a weight of 0,5 kg, 0,75 kg and 1 kg. The scratch tests were summarized in the table 13.

*Table 13 Scratch test conditions*

HV Hardness [GPa]		Load [N]	
≅0.6	≅4.9	≅7.35	≅9.8
≅0.73	≅4.9	≅7.35	≅9.8
≅0.81	≅4.9	≅7.35	≅9.8

## 6.2.4 Tensile Test

Static tensile tests were carried out to analyse the structural stability of the coating, both in elastic and fully plastic field. More in detail, the ability to maintain hydrophobic behaviour was evaluated, despite the structural damage of the silane coating induced by applied strain. To perform the tensile tests, ITALSIGMA servo-hydraulic machine with 25 kN load cell was used. Different tensile tests at varying strain threshold were performed in order to compare the surface properties modification at varying applied strain. In particular, 2 tests in elastic field (0.1 mm and 0.2 mm displacement, respectively) and 3 tests in a plastic field (the tests stopped at 3.0. mm, 7.3 mm and at failure respectively), with a constant speed of 1 mm/min were performed.

## 6.2.5 Surface morphology characterization

The characterization of the microstructure of the silane coating and its damage after mechanical tests, were performed using optical microscope (OM) and scanning electronic microscope (SEM) equipped with an EDS probe.

The optical microscopy was carried out by means a LEICA stereomicroscope, while the confocal microscopy was carried out by LEICA DCM 3D. The Leica DCM 3D, with dual core technology is a confocal microscope designed for a rapid and non-invasive evaluation of micro and nano-structures. It combines confocal technology,

Materials and method

for resolution along the x and y axes, and interferometric, for resolution along the z-axis on a sub-nanometric scale, ensuring a resolution of 0.1 nm. Confocal microscopies were performed with 20X and 100X lens whose characteristics are shown in the Table . Table 15 shows the set-up parameters used for the confocal scans.

Table 14 Characteristic parameters of 20x and 100x lenses

Characteristic parameters				
Objective	NA (numerical aperture)	WD (Working distance)	Pixel size (µm)	Min. range (µm)
20x	0.50	1.27	0.83	20
100x	0.90	0.27	0.16	4

Table 15 Set-up parameters of confocal scan

Set-up parameters									
As-Received					Tooled				
Name	Objective	Z-scan	Speed	resolution	Name	Objective	Z-scan	Speed	resolution
Untested	Epi 100X-L	5.2 µm	1x	768x576	Untested	Epi 100X-L	9.2 µm	1x	768x576
P1		16 µm			P1		16 µm		
P2		16 µm			P2		16 µm		
P4		8 µm			P4		6 µm		

SEM and EDS analyses were carried out by SEM Hitachi TM 3030-PLUS. The EDS system has a SDD detector without nitrogen cooling. The XRF has a 50 kV and 125 µA generator; the SDD detector has a resolution of 175 eV. For comparison purpose,

## Materials and method

surface profile evaluation was carried also on as received and worked surfaces before mechanical tests.

## CHAPTER VII

### Experimental results

#### 7.1 Texturing experimental results

To evaluate the behaviour of the bronze alloy coating subject to texture processing, tribological tests were carried out according to the specifications shown in table 7. It should be noted that very high loads have been specifically chosen, compared to the loads generally used in the literature, to simulate the severe contact conditions to which the rotating parts of the axial piston pumps are subjected in conditions of poor lubrication.

The test temperature is around 70 C °, the typical working temperature of the pumps and axial piston motors. The test time was 10 min. with a speed of 2000 rpm.

##### 7.1.1 Friction and wear

Figure 64 shows the variation of the friction coefficient as a function of time, while in table 16 the averages of the friction coefficients are shown.

## Experimental results

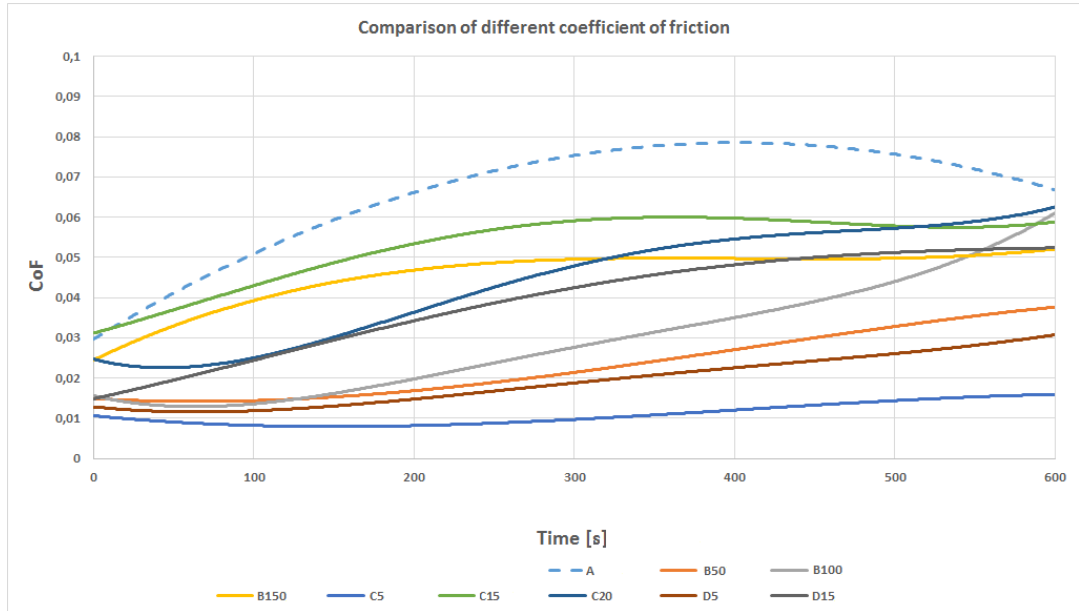


Figure 64 Comparison of the different coefficient of friction

Table 16 Average of coefficient of friction

Average of coefficient of friction								
A	B50	B100	B150	C5	C15	C20	D5	D15
0,066	0,023	0,029	0,045	0,010	0,053	0,043	0,019	0,039

By analysing the trend of the friction coefficient shown in figures 64 it is possible to notice that the non-textured specimen maintains a higher friction coefficient compared to the textured samples, when subjected to a load of 706.8 N. The friction coefficient decreases by producing the dimples on the surface of the samples, however changing the characteristics of the texture, the response of the coating in terms of friction coefficient also changes, which does not always represent an improvement compared to the non-textured surface. In fact, figure 64 shows that at the end of the test for some types of profiler, the friction coefficient increases reaching values similar to the unprocessed specimen. An interesting analysis regards

## Experimental results

the influence assumed by the variation of a single geometric parameter on the friction coefficient.

### 7.1.2 Effect of dimples diameter

In Figure 65 is shown the trend of the friction coefficient as a variation of the diameter of the dimples.

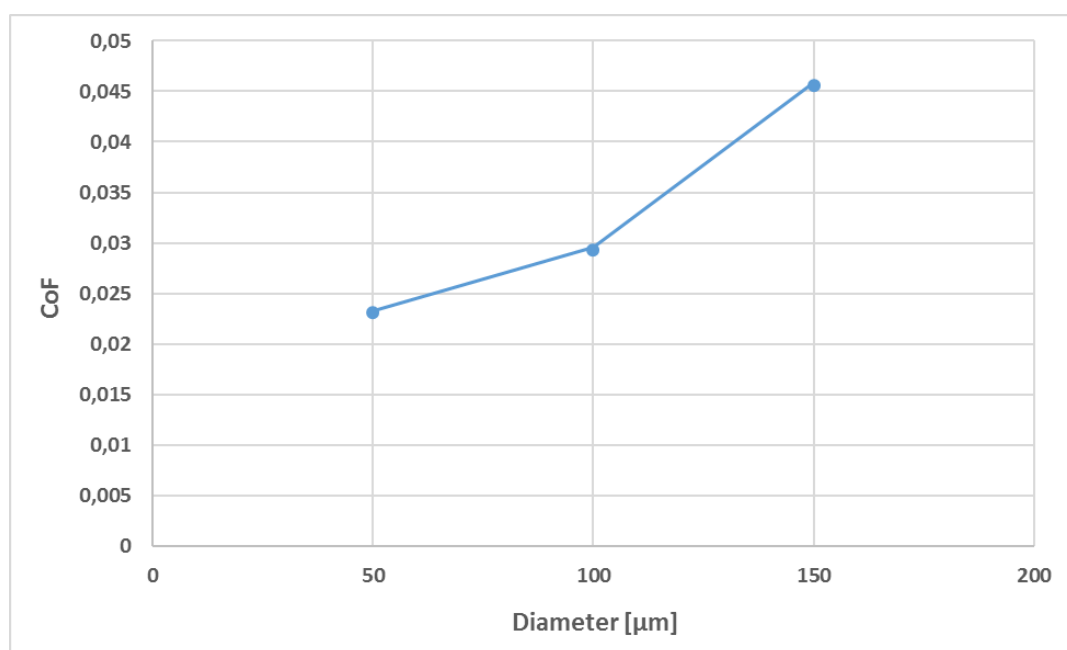


*Figure 65 Variation of the friction coefficient as a function of the dimples diameter*

The curve shows that as the diameter of the dimples increases, the friction coefficient increases. This behaviour of the coating may be due in part to the formation of pile-up, i.e. the accumulations of bronze alloy due to the melting generated by the processing of laser texturing (figure66).

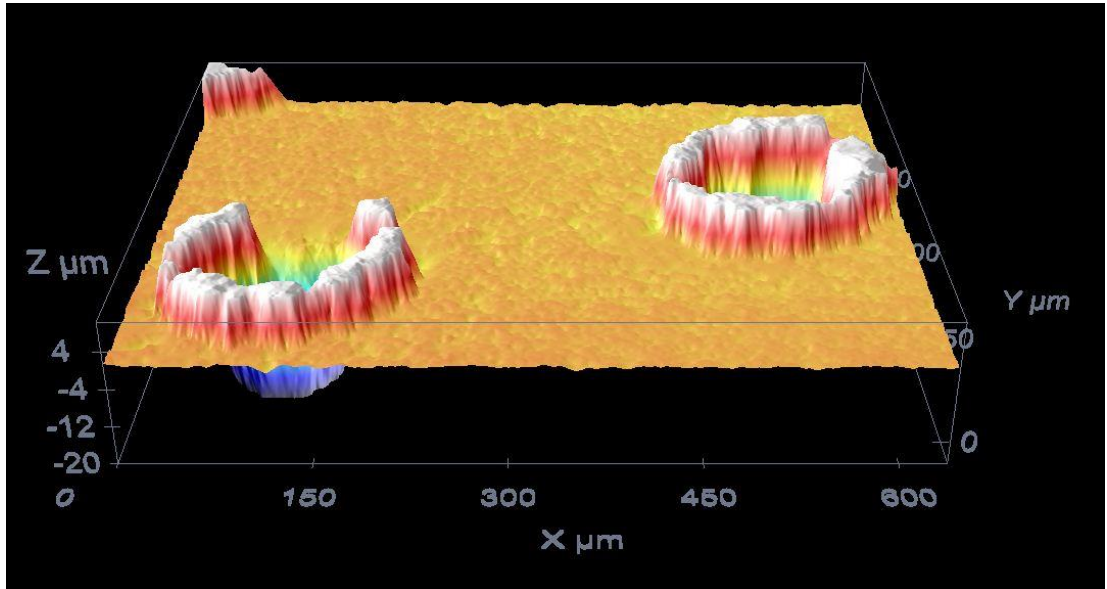


*Figure 66 Confocal analysis of the surface of sample B150, which highlights the presence of pile-up*

The greater the dimples diameter, the greater the height of the pile-up and therefore the greater the friction generated on contact with the counter-specimen. In fact, figure 67 shows the profile of the surface along the x axis. It is possible to notice that the pile-up assumes dimensions of even 20  $\mu\text{m}$ .

## Experimental results

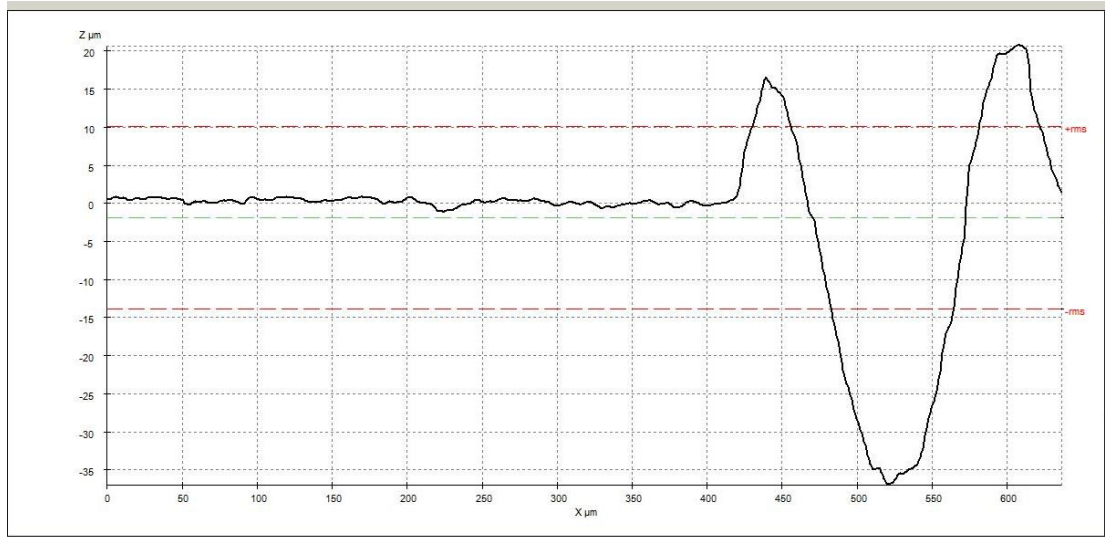


*Figure 67 Profile analysis of specimen B150*

The increase of friction coefficients can also be explained by the decrease in lubrication during the test. In fact, by increasing the size of the dimples, the oleophobicity of the coating decreases and the oil remains trapped inside the dimples.

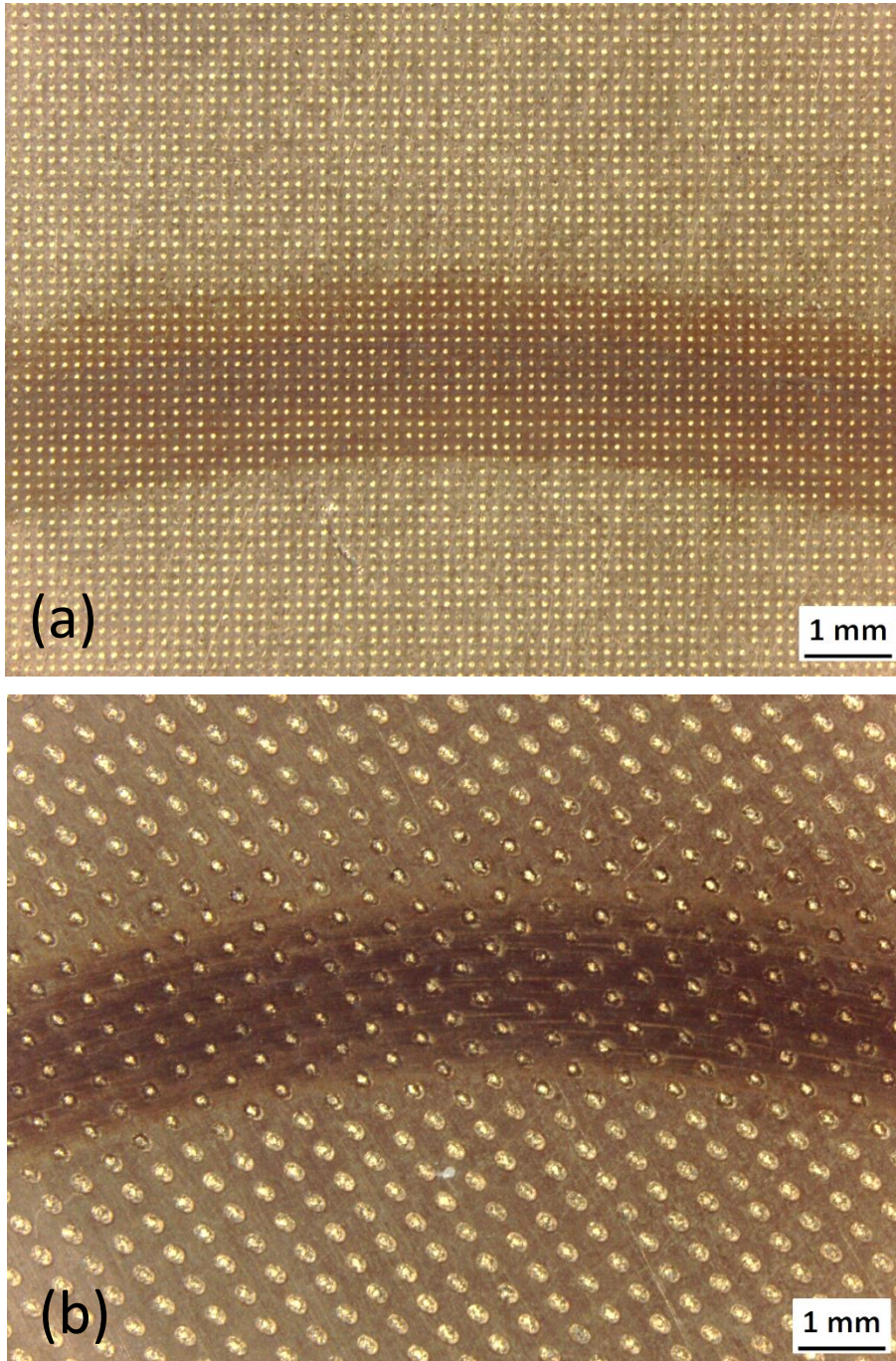
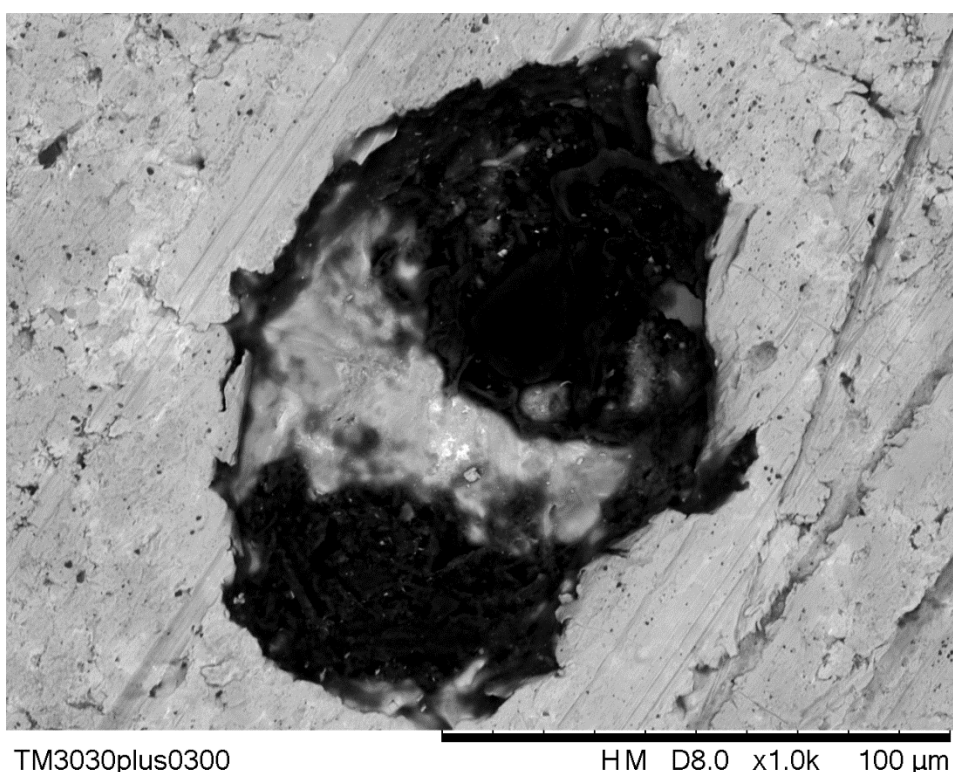


Figure 68 a) Wear track of sample B50; b) wear track of sample B150

## Experimental results

By comparing the wear track in the case of specimen B50 and in the case of specimen B150 (figure 68a, 68b) it can be underlined that in the second case an evident phenomenon of seizure was generated due in part to poor lubrication, in part due to the formation of debris, favoured by the presence of pile-up, as highlighted by the SEM analyses in figures 69. Since the bronze alloy is very malleable, the pile up in contact with the pin (100Cr6) are partially removed with the formation of debris, and partially "spread" on the dimples causing a partial occlusion.



*Figure 69 The SEM image shows the presence of bronze alloy debris inside the dimples*

Another important aspect concerns the influence of temperature on the anti-friction behaviour of the coating. To evaluate the temperature trend, two tests carried out under different conditions were considered. The A1 test carried out on the B150

## Experimental results

sample complies with the test conditions expressed in table 7, while the A2 test on the B150 sample was obtained with a load of 40 N and a speed of 500 rpm. In particular, by comparing the trend of the temperature measured through a thermocouple (figure 70), it can be seen that in the case of the A1 test the high load applied causes a wide variation in temperature during the test, and therefore a degradation of the lubricating oil. The degradation of the lubricating oil and the consequent loss of viscosity generates a decrease in lubrication due to the action of the centrifugal force.

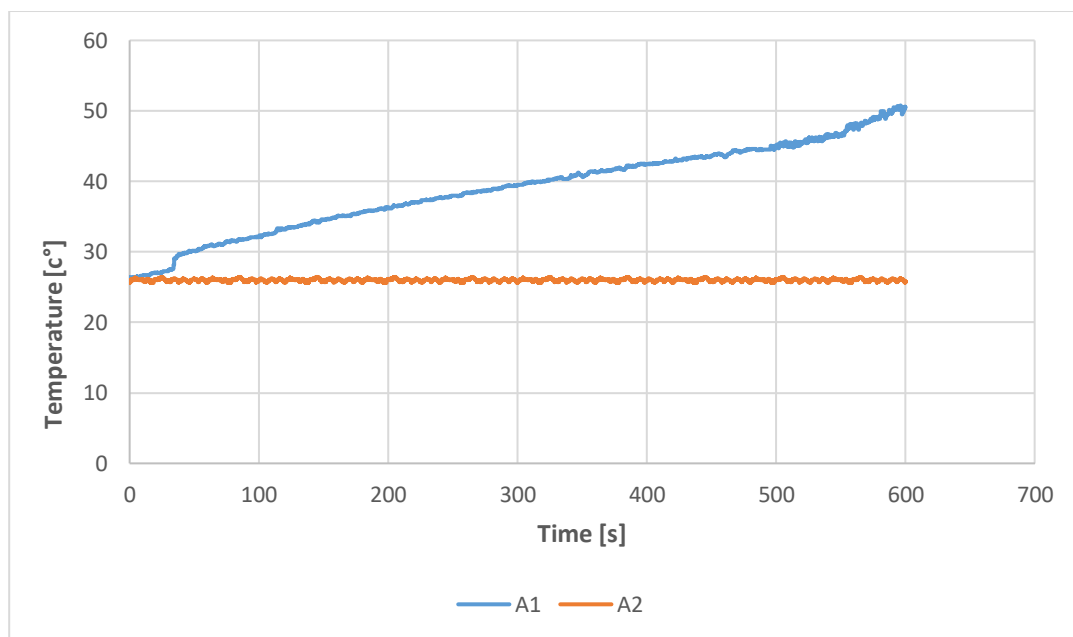


*Figure 70 Oil temperature trend as a function of time*

Therefore, it follows that the increase in temperature leads to an increase in the friction force and consequently a deterioration of the surface as can be seen from the trace in figure 68. The SEM image (figure71) instead shows the trace of the A2 test which has maintained a constant temperature. As can be seen, the absence of pile-

## Experimental results

ups (the sample was lapped before the test) may have contributed to maintaining a constant temperature.

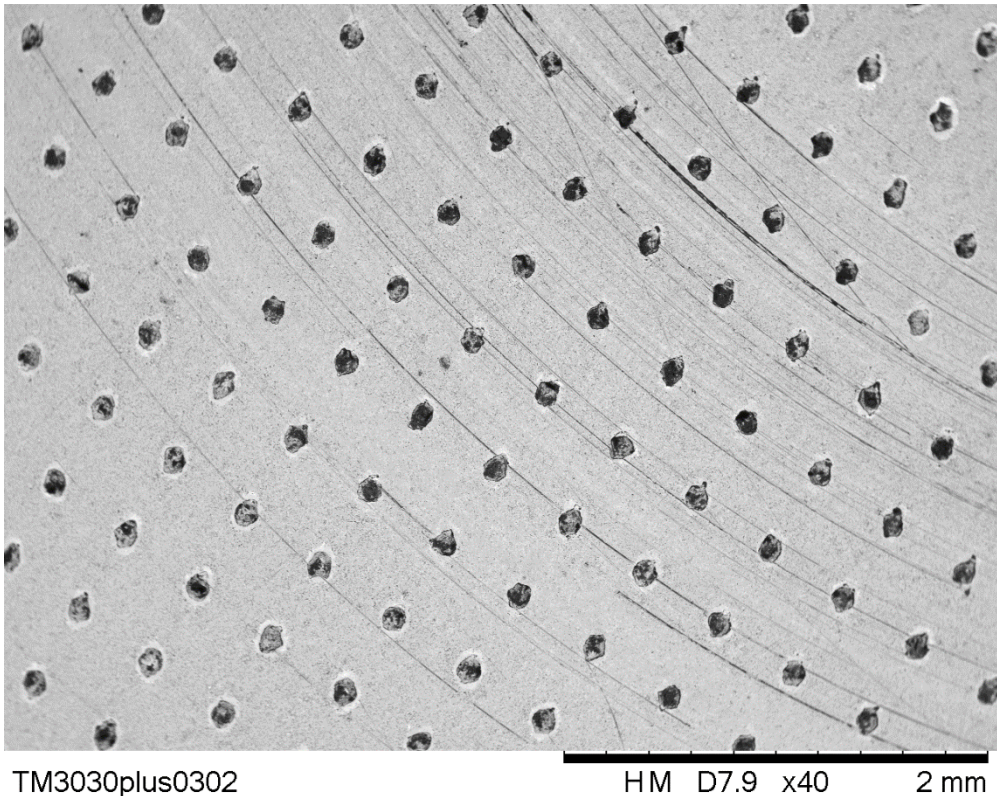


*Figure 71 SEM image at 40x of the pin track on the bronze disc*

### 7.1.3 Effect of dimples density

In Figure 72 is shown the trend of the friction coefficient as a variation of the dimples density.

## Experimental results

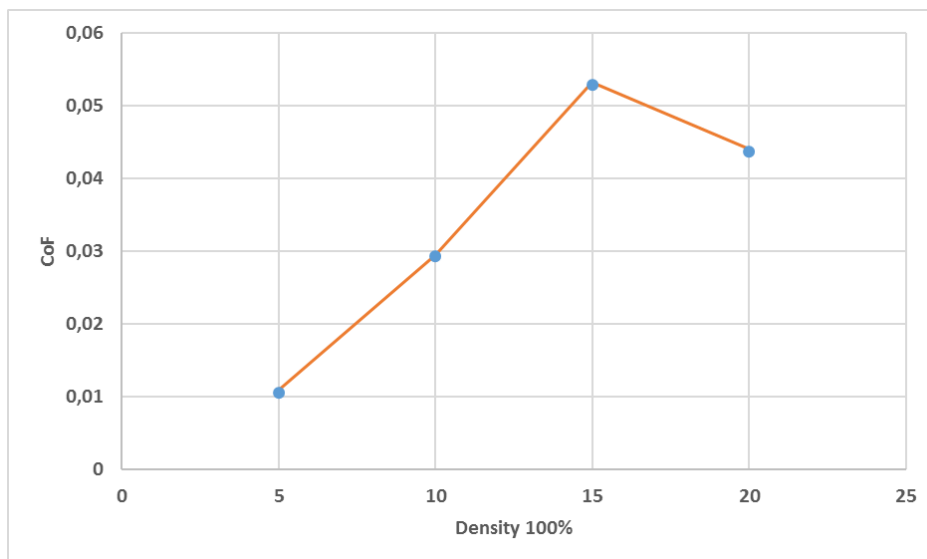
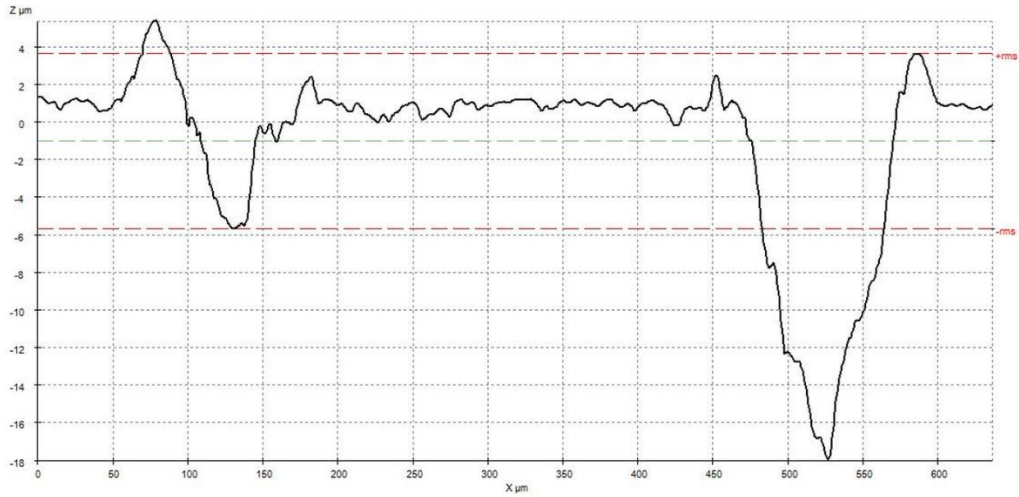


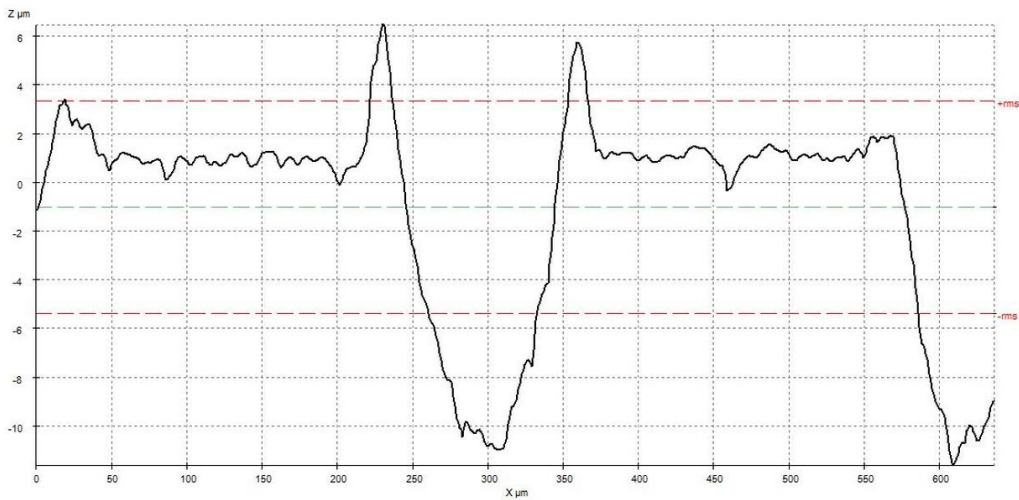
*Figure 72 Variation of the friction coefficient as a function of the dimples density*

As shown by the trend of the orange curve in figure 72, by varying the density of the dimples on the surface of the sample, the friction coefficient also varies. The effect shown by the tribological tests is unexpected with respect to the predicted trend of the CoF. In particular, as the area of the surface occupied by the dimples increases, a decrease in CoF is expected due to the increase in the surface oleo-phobicity, i.e. the contact angle increases as the surface roughness increases. This observation is partly true, but as demonstrated also by [54] et. al, the increase in density can lead to an increase in the friction coefficient, due to an increase in roughness and to the pile up, whose increase is proportional to the quantity of dimples present on the surface. The increase in roughness can be seen in figures 73a), 73b), 73c), which show the roughness profile of samples C5, C15, C20.

## Experimental results

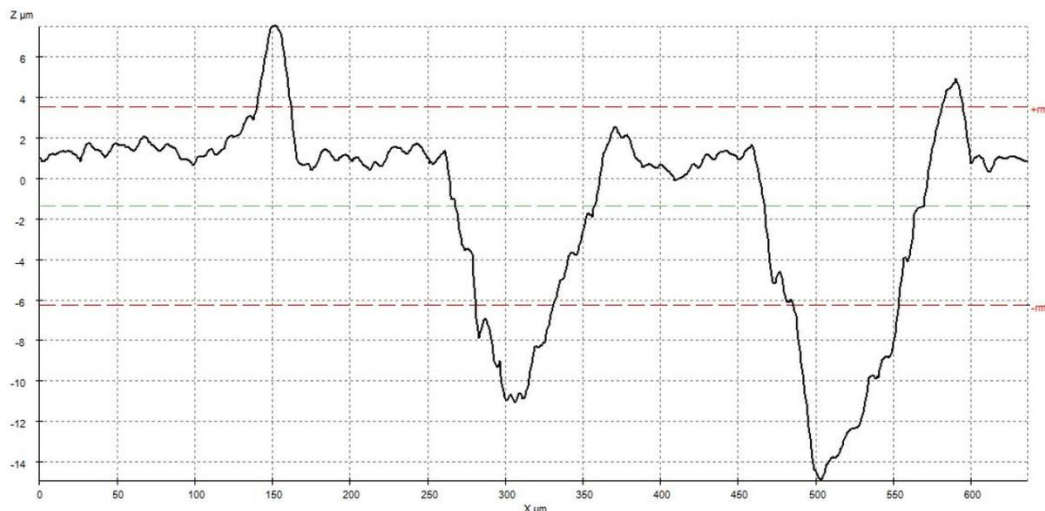


73 a)



73 b)

## Experimental results



73 c)

Figure 73 a) Roughness profile of specimen C5; b) Roughness profile of specimen C15; c) Roughness profile of specimen C20.

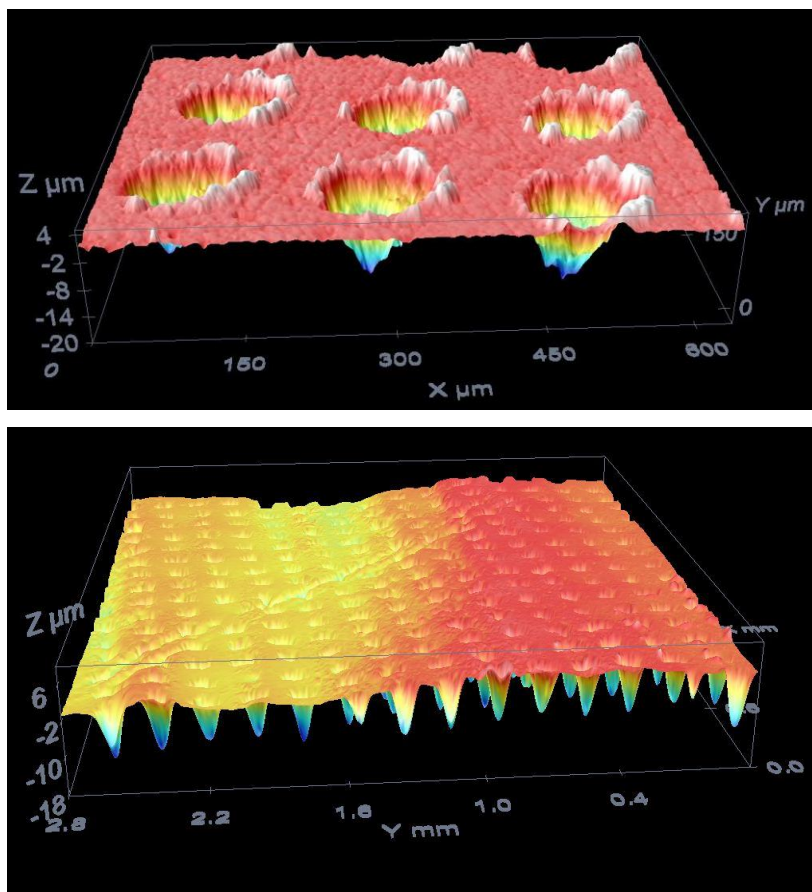
What can be noticed is that the parameter Sa (table 17), which represents the average roughness of the analysed surface, increases with the density of the dimples. In particular, for the C5 specimen with a density of 5% there will be an average roughness Sa equal to 1.0819  $\mu\text{m}$ ; for the C15 specimen with a density of 15% there will be an average roughness Sa equal to 2.1296  $\mu\text{m}$ ; for the C20 specimen with a density of 20% there will be an average roughness Sa equal to 2.5007  $\mu\text{m}$ .

Table 17 Surface parameters obtained with the confocal microscopy

Roughness parameters				
Name	Area	Max	Min	Sa
C5	636x427 $\mu\text{m}^2$	8,4017 $\mu\text{m}$	-19,082 $\mu\text{m}$	1,0819 $\mu\text{m}$
C15	636x427 $\mu\text{m}^2$	8,3067 $\mu\text{m}$	-17,738 $\mu\text{m}$	2,1296 $\mu\text{m}$
C20	636x427 $\mu\text{m}^2$	10,582 $\mu\text{m}$	-17,046 $\mu\text{m}$	2,5007 $\mu\text{m}$

## Experimental results

The surface deterioration due to the tribological test is evident by analysing figure 74a) and 74b), which shows the confocal scans of the C20 specimen before and after the test.



*Figure 74 Confocal scan of C20 specimen untested surface; b) Confocal scan of C20 specimen after the tribological test*

From figure 74b) it can be seen that on the wear track there are microgrooves, which indicate the presence of abrasive particles. In figure 74a) instead the pile ups are very evident, highlighted in white in the image. A more detailed analysis of the wear track was carried out with the SEM microscope and the EDS probe. In table 18 the values

## Experimental results

calculated according ISO 25178 are reported. The mean value of roughness of untested and tested specimen is respectively 2.68  $\mu\text{m}$  and 1.65  $\mu\text{m}$ .

*Table 18 Summary of roughness parameters*

<b>Height parameters</b>		
	<b>Untested</b>	<b>Tested</b>
<b>Sq [<math>\mu\text{m}</math>]</b>	3.70	3.13
<b>Ssk [<math>\mu\text{m}</math>]</b>	-1.42	-3.03
<b>Sku [<math>\mu\text{m}</math>]</b>	5.68	12.70
<b>Sp [<math>\mu\text{m}</math>]</b>	10.38	10.05
<b>Sv [<math>\mu\text{m}</math>]</b>	20.65	18.33
<b>Sz [<math>\mu\text{m}</math>]</b>	31.04	28.38
<b>Sa [<math>\mu\text{m}</math>]</b>	2.68	1.65

### 7.1.4 Effect of dimples depth

In Figure 75 is shown the trend of the friction coefficient as a variation of the dimples depth.

## Experimental results

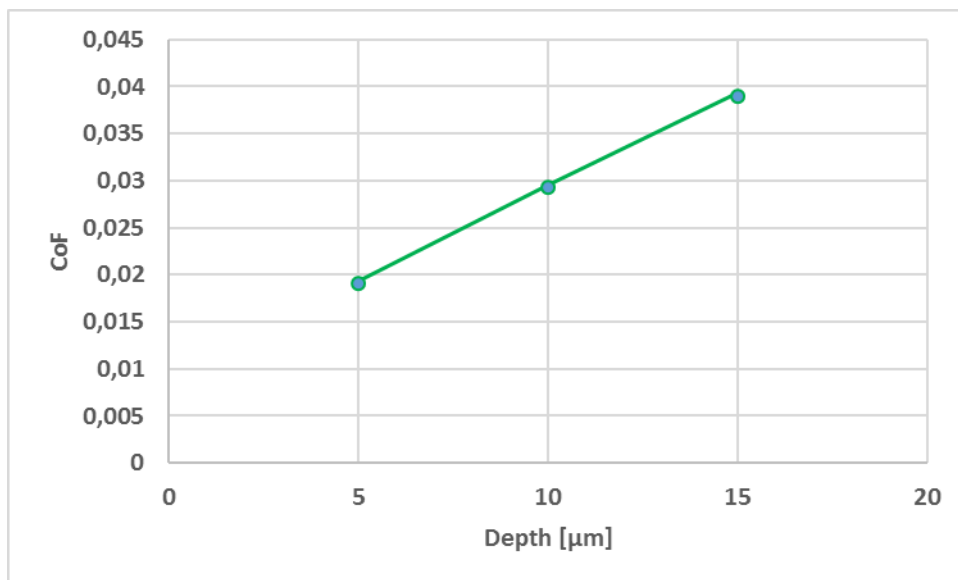


*Figure 75 Variation of the friction coefficient as a function of the dimples depth*

It is possible to highlight in figure 75 that by increasing the depth of the dimples, the friction coefficient increases. This behaviour could be due to an excessive "reservoir" effect of the dimples, which with increasing depth tend to catch the oil and do not allow correct lubrication.

Also in this case, the increase in the depth of the dimples could lead to a decrease in the surface oleophobicity and therefore a poor lubrication.

Another important aspect regards, as mentioned above, the formation of piles up, which are more evident in sample D15 than in sample D5 as shown in figure 76a) and 76b).

## Experimental results

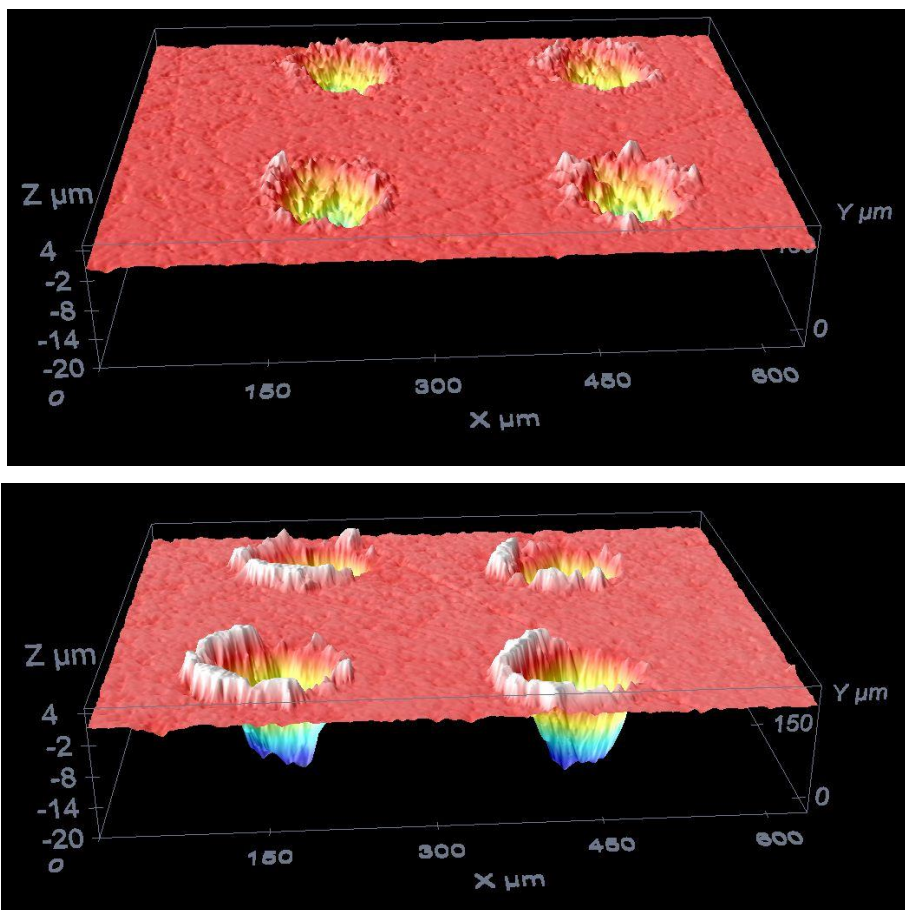


*Figure 76 a) Confocal microscopy of sample D5 with 100x lens b) confocal microscopy of sample D15 with 100x lens*

This is due to the amount of alloy that must be melted by the laser to make the dimples, which is greater in the case of sample D15 with a depth of 15 microns than in sample D5 with a depth of 5 microns. Furthermore, since the bronze alloy is very malleable, it is difficult to carry out lapping operations on the surface after texturing, as it would lead to the closure of part of the dimples.

After separately analysing the effect of the diameter, density and depth of the dimples on the friction coefficient, it is possible to affirm that a lower density associated with

## Experimental results

a lower depth have an improvement effect on the friction coefficient compared to the change in diameter.

### 7.1.5 Wear track

As mentioned in the previous paragraphs, the presence of the pile up can cause abrasive wear, as shown by the microgrooves in figure 74b (previous paragraph).

To analyse the state of the wear track in more detail, microscopies were performed with the aid of the SEM. the B150 was chosen as the specimen to be studied, as shown in figure 77, in which the diameter of the dimples is measured, which is approximately equal to 150 microns, as per specifications in table 8.

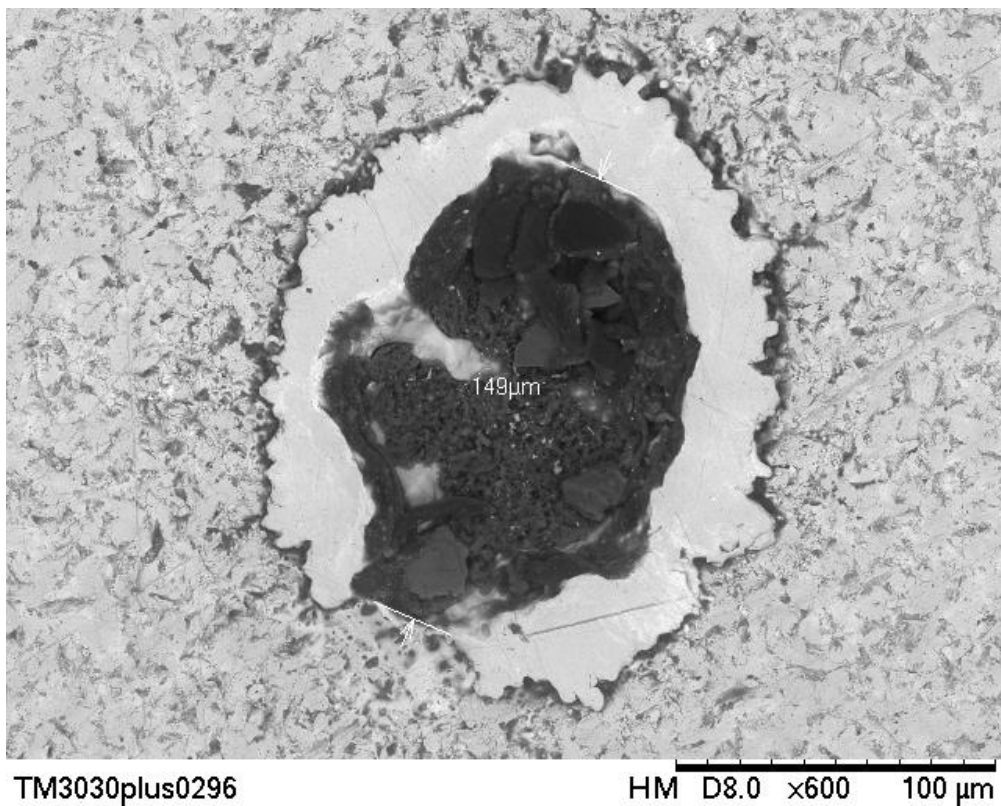


*Figure 77 SEM image at 600x of dimple of B150 specimen*

## Experimental results

Analysing the wear track (figure 78) it should be noted the presence of the microgrooves due to the action of an abrasive particle, which could be due to the action of debris that was formed by detachment of a portion of pile up, or it could be debris due to the deterioration of the pin.

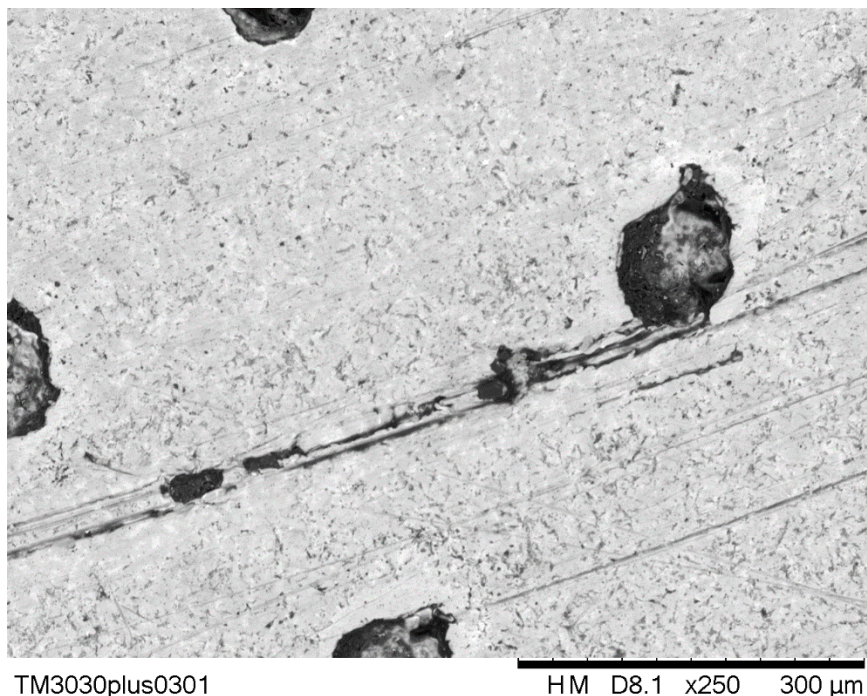


*Figure 78 SEM image at 250 x of microgrooves on bronze alloy surface*

To confirm the nature of the debris, a "point and shot" analysis with the EDS probe was performed. As can be seen in figure 79, the analysis on the debris returns the characteristic peak of Fe at 6.4 keV. Since there is no Fe in the composition of the bronze alloy, the particle that generated the microgrooves certainly comes from the deterioration of the pin.

## Experimental results

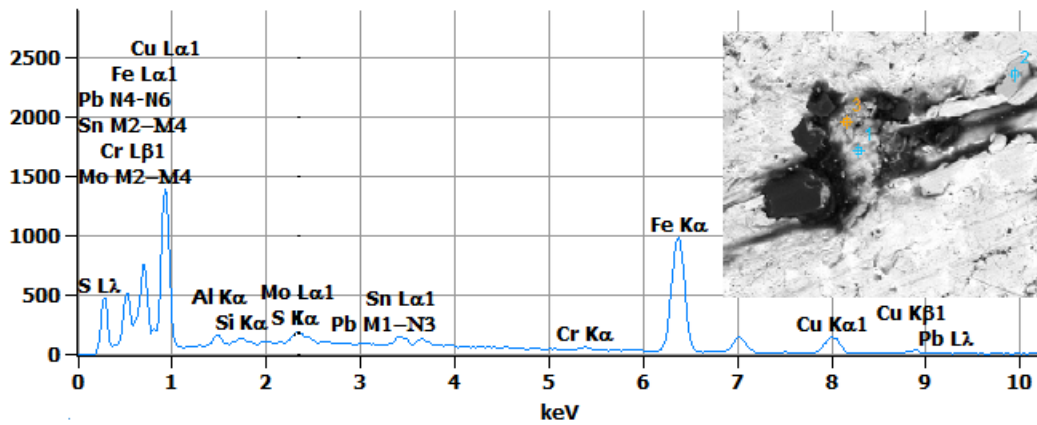
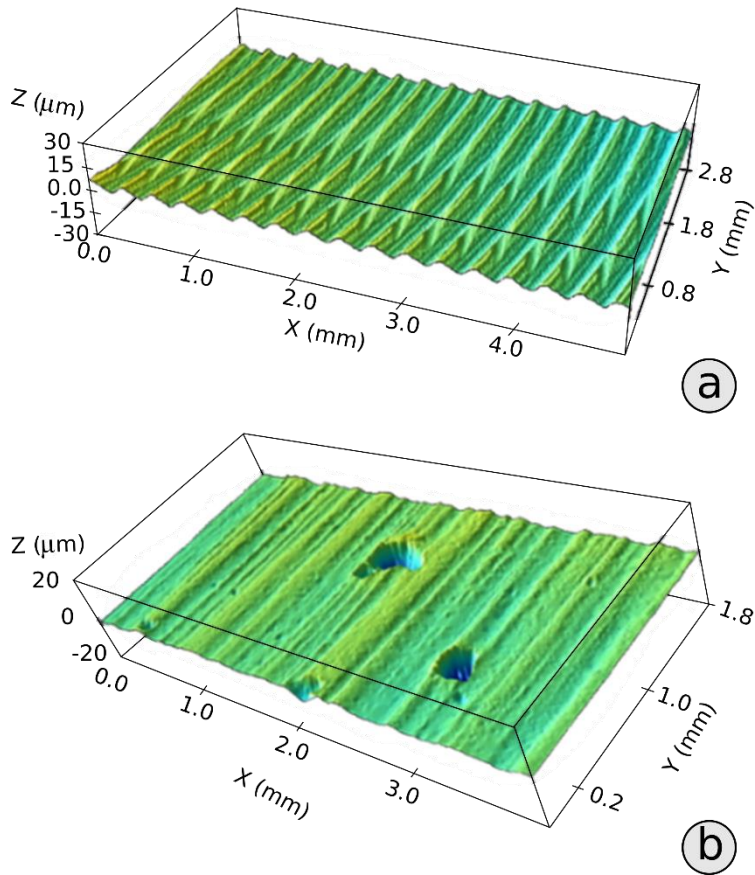


Figure 79 EDS analysis shows the presence of Fe through the characteristic peak at 6.4 keV.

## 7.2 Hydrophobic experimental results

Preliminarily, the response of the coating subjected to the conditions of mechanical degradation was analysed. Through the use of the confocal microscope, the surface topography was assessed on both sides of the silanized samples, the side of the as-received tooled surface (A-WS, Figure 80a), and the side of the rough surface (i.e. not tooled, A-RS Figure 80b)

## Experimental results



*Figure 80 Confocal analysis of a) tooled surface b) as received surface of uncoated specimen*

The difference in roughness between the two surfaces, highlighted with confocal microscopy (figure 81), allowed a different anchoring of the coating to the substrate, and therefore a difference in the hydrophobicity properties, as evidenced by the wettability of the coating (table 18). The tooled surface morphology is clearly constituted by regular distribution of peaks and valleys due to the applied milling procedure. Each peak is characterized by a distance between peak and valley of about  $5 \mu m$ . Along the specimen gauge length, the distance between peak and valley is about  $220 \mu m$ . Instead, the as received surface shows random shaped peaks and valley on the whole profile. Some local surface heterogeneities can be furthermore

## Experimental results

identified. These heterogeneities may be related to local defects or probably to unexpected scratch or punching during handling.

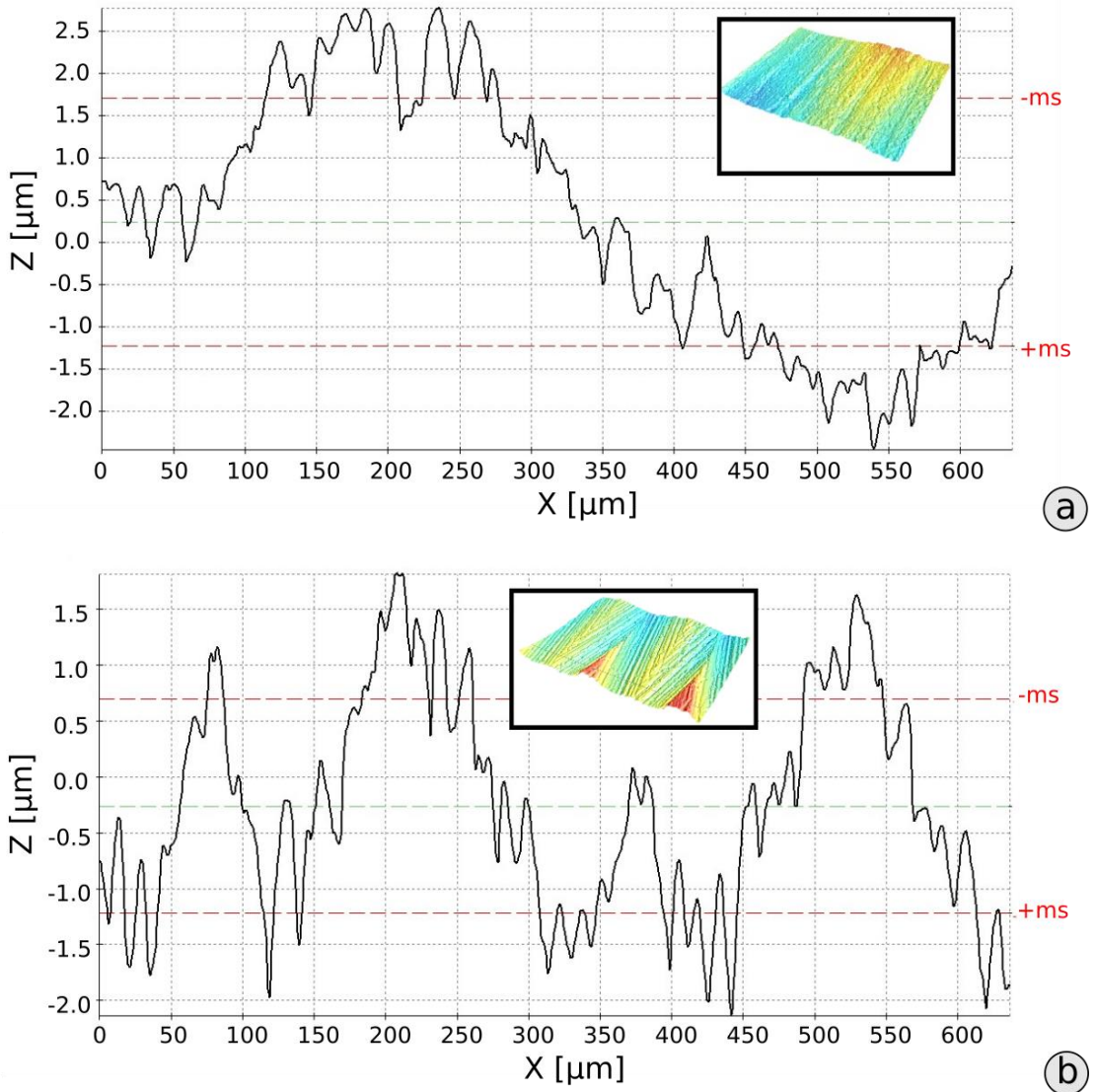


Figure 81 Roughness analyses with confocal microscopy: analysis along x-axis of (a) tooled surface. (b) as received surface of uncoated specimen

## Experimental results

By confocal scans of a large area (5 x 3 mm) of the as-received specimens, the mean value of roughness of as received and tooled side is 1.27  $\mu\text{m}$  and 1.89  $\mu\text{m}$ , respectively. In table 19 the values calculated according ISO 25178 are reported.

*Table 19 Summary of roughness parameters for sample 1*

<b>Height parameters</b>		
	<b>Rough</b>	<b>Tooled</b>
<b>Sq [<math>\mu\text{m}</math>]</b>	1.76	2.32
<b>Ssk [<math>\mu\text{m}</math>]</b>	-2.33	0.05
<b>Sku [<math>\mu\text{m}</math>]</b>	23.5	2.52
<b>Sp [<math>\mu\text{m}</math>]</b>	6.22	7.32
<b>Sv [<math>\mu\text{m}</math>]</b>	21.61	7.43
<b>Sz [<math>\mu\text{m}</math>]</b>	27.83	17.4
<b>Sa [<math>\mu\text{m}</math>]</b>	1.27	1.89

*Table 20 Summary of roughness parameters for sample 2*

<b>Height parameters</b>		
	<b>Rough</b>	<b>Tooled</b>
<b>Sq [<math>\mu\text{m}</math>]</b>	0.80	1.07
<b>Ssk [<math>\mu\text{m}</math>]</b>	-0.03	-0.09
<b>Sku [<math>\mu\text{m}</math>]</b>	1.34	1.78
<b>Sp [<math>\mu\text{m}</math>]</b>	1.84	2.24
<b>Sv [<math>\mu\text{m}</math>]</b>	2.12	2.21
<b>Sz [<math>\mu\text{m}</math>]</b>	3.95	4.45
<b>Sa [<math>\mu\text{m}</math>]</b>	0.75	0.96

## Experimental results

Legenda: Sq = Root mean square height of the surface; Ssk = Skewness of height distribution; Sku = Kurtosis of height distribution; Sp = Maximum height of peaks; Sv = Maximum height of valleys; Sz = Maximum height of the surface; Sa = Arithmetical mean height of the surface.

The skewness, Ssk, indicates the degree of asymmetry of a surface profile. When the Ssk is equal to zero, there is equality between the number of the peaks and the number of valleys indicating that the distribution is symmetrical. However,  $Ssk < 0$  indicates that the profile is mainly characterized by deep valleys, which is the case of the rough surface. After treatment, the Skewness parameter of the surface increases from -2.33 to 0.05 indicating that the distribution of the peaks and valleys on the aluminium surface becomes symmetrical.

In addition, Kurtosis parameter, Sku, measures the peakedness of the roughness and its value is related to the height distribution on the surface. Kurtosis is sensitive to the presence of isolated peaks (or valleys) on the surface. When Sku is equal to 3, it means that the analysed surface is characterized by heights normal distribution. The rough surface is characterized by a very high Kurtosis (23.5), which is due to the presence of local defects. However, the Sku parameter of the tooled surface is quite near to 3 thus the heights are characterized by a normal distribution.

Preliminarily, water contact angle (WCA) measurements on both surface sides of each sample were performed. The results, for a reference sample, are shown in table 21 and 22. Similar behaviour was observed on the other samples.

*Table 21 Contact angle of tooled and “as received” surface (sample 1)*

Water contact angle [°]	
A-WS	A-RS
134.8	123.1

## Experimental results

	136.3	131.3
	132.1	129.4
	136.2	123
	130.1	126.3
	135.2	121.4
	132.3	124.9
<b>Mean</b>	133.5	125.6
<b>Standard Deviation</b>	2.3	3.6

*Table 22 Contact angle of tooled and “as received” surface (sample 2)*

<b>Water contact angle [°]</b>		
	<b>A-WS</b>	<b>A-RS</b>
	130	130,5
	131,1	126,6
	131,3	131,2
	130,4	126,4
	134,3	127,6
<b>Mean</b>	131.4	128.5
<b>Standard Deviation</b>	1.7	2.25

As shown by the sessile drop test results, the coating gives a high degree of hydrophobicity, taking into account the hydrophilic nature of the aluminium alloy. Indeed, the aluminium and its different alloys are characterized by a water contact

## Experimental results

angle lower than  $90^\circ$  [55]–[57]. Thus, the water droplets spread immediately on the raw aluminium surface without bouncing off. After silanization, both tooled and As-received surfaces showed a high anti-wettability with average contact angles of  $133.5^\circ$  and  $125.6^\circ$  respectively. This change of the wetting behaviour of the aluminium surfaces can be attributed to the coupled action of the surface roughness and the surface energy [58]. In fact, the deposition of silane coating on substrate surface induces the decrease of the surface energy and thus the affinity of the surface with water. On the other hand, the contact angles of both tooled and as received aluminium surfaces, after silane coating, are below the super-hydrophobicity threshold of  $150^\circ$ . This latter requires the presence of hierarchical nano/microstructure on the substrate surface, which is not our case [59].

Furthermore, the machined surface has a slight greater degree of hydrophobicity than the 'as received' one, and this value is justified by the greater surface roughness. According to Wenzel and Cassie-Baxter wetting theories, the increase of the surface roughness has a positive effect on the surface hydrophobicity [55], [56].

### 7.2.1 Scratch Damaging

Several scratch tests have been performed to evaluate the wear resistance of the silane coating three different pencil hardness 4H, 5H, 6H, corresponding respectively to the Vickers hardness of 60 HV, 73 HV, 81 HV have been used. Furthermore, in order to assess the scratch resistance of the coating, for each kind of test three different loads, respectively 500 g, 750 g and 1000 g, have been applied.

The scratch tests were carried out both on the tooled side and the 'as received' side. Figure 82 show, as reference the wear track obtained using Pencil 6H with load of 500g on A-WS sample.

## Experimental results

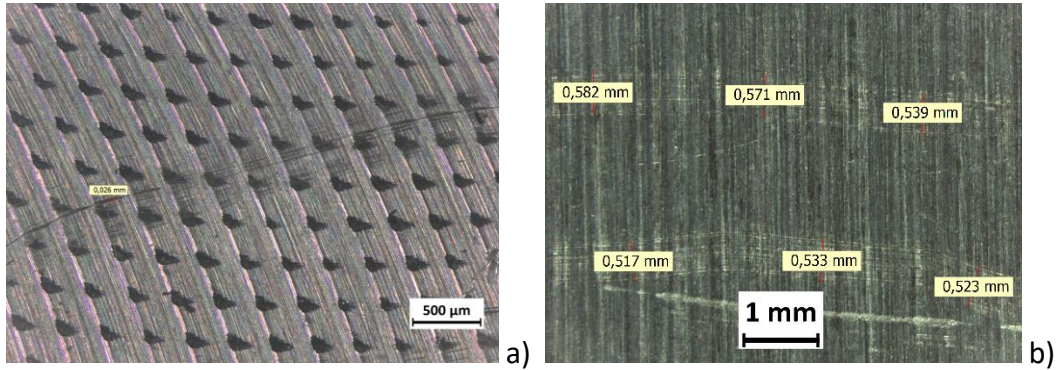


*Figure 82 Optical micrographs a) of wear track obtained using pencil 6H with load of 500g on A-WS sample; b) of wear track obtained using pencil 5H with load of 1000g on A-RS sample*

As shown in the figure 82, the damage caused by the pencil 6H (81 HV), is evidenced as identifiable by the track width (about 26 μm). The surface morphology is affected by the abrasive action induced by the indenter. Scratch rivers are clearly visible indicating a local surface degradation induced by the local mechanical damaging. The local damage of the protective coating due to the scratching action, although it did not affect the mechanical stability of the metallic substrate (there are no evident abrasions or undercoating cracks on the aluminium substrate), it can have a significant effect on the surface properties. Hence, in order to better evaluate whether the mechanical scratch test can affect the surface properties of the coating and its interaction with water, wettability tests were performed on scratched samples at varying indenter hardness and load. The results of the sessile drop tests on distilled water are shown in figure 83.

## Experimental results

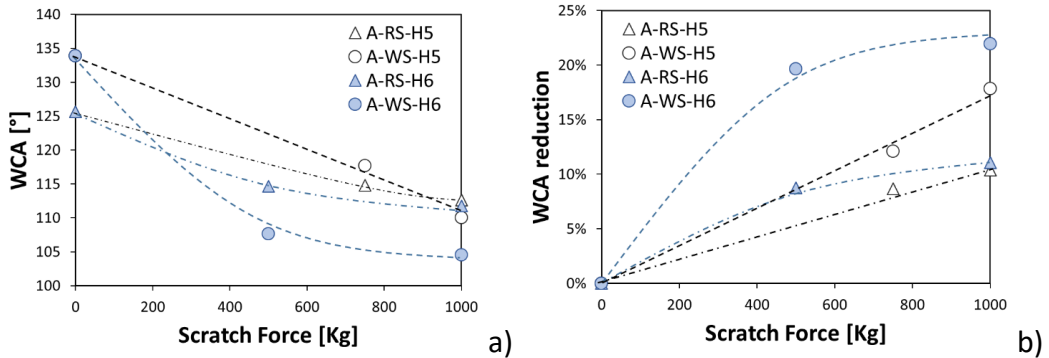


*Figure 83 Evolution at increasing scratching force and varying hardness indenter of water contact angle a) and hydrophobicity reduction (WCA reduction) b) for tooled and as received silanized surfaces.*

A clear decrease of the water contact angles was observed on both tooled and as received surface after the scratch test with 5H pencil. In fact, the tooled surface water contact angle decreased by about 19.4% (from 133.5° to 107.6°) at 500g load and by 22.2% (from 133.5° to 103.8°) at 1000g load. However, the water contact angle on the as received surface decreased by only 14% at 500g load and by 16% at 1000g load. Thus, the tooled surface is more sensitive to the scratch test than the as received one that is probably due to the destroyed roughness because the resistance to abrasion of the rough surface is lower than the smooth one [56]. Similar behaviour was observed when the 6H pencil was used.

Furthermore, better analysing Figure b referred to WCA reduction calculated as percentage of the not scratched to scratched WCA ratio, it is possible arguer further details. The WCA reduction in H6 scratched samples exhibit a degradation plateau at high applied load. Instead on H5 one an almost linear evolution of WCA reduction occurs. This behaviour could be due to the penetration depth that in H6 is relevant also at low force level. That leads to critically damage the silane coating also at intermediate scratching load (500g). The result is a low contact angle (and therefore high WCA reduction) also at medium force level due to a relevant hydrophobic contribute of the aluminium substrate exposed to air after the coating damaging. A

## Experimental results

further increase of scratching force not significantly affects the wettability properties of the surface.

Therefore, the increase of the pencil hardness from 73 Hv to 81 Hv has a slight effect on the wettability results. As expected, increasing the pencil harness a larger reduction in WCA occurs. On the other hand, even after these scratch tests, the prepared aluminium surfaces maintain their hydrophobicity with water contact angles higher than  $90^\circ$ , which means that the silane coating was not totally damaged. The remained silane chains affect the hydrophobic behaviour by shielding the polar groups from interaction with water [57].

### 7.2.2 Tensile Damaging

To evaluate the mechanical behaviour of the silane coating, and in particular the ability to maintain the hydrophobicity characteristic when subjected to elastic and plastic deformation, some tensile tests were carried out. This is particularly useful in order to evaluate the coating surface stability and durability under real operating conditions in which mechanical stresses are usually applied

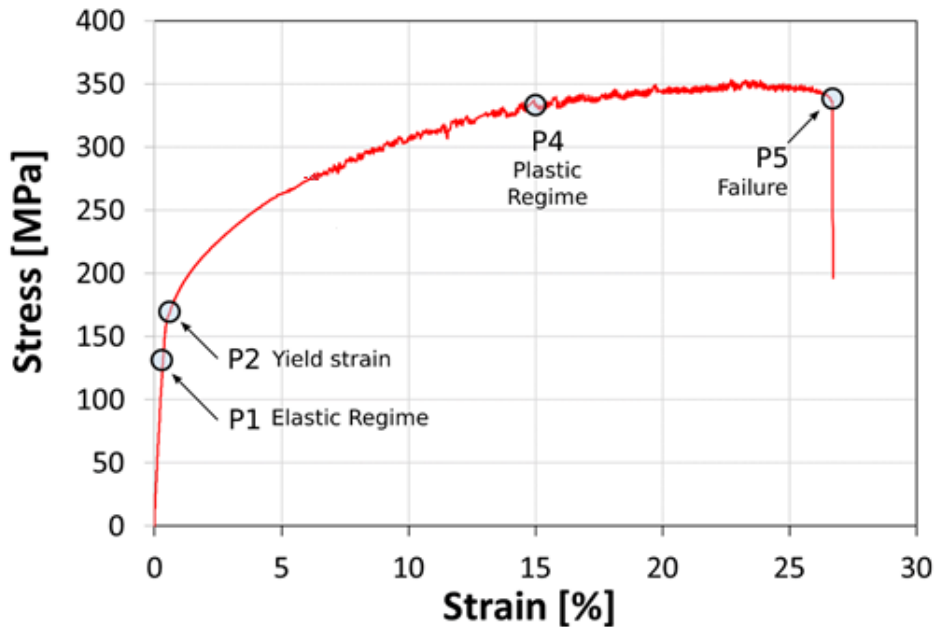


Figure 84 Tensile stress-strain curve of AA5083 aluminium alloy. Markers are referred to reference points identified for wettability measurements

A reference tensile stress-strain curve of AA5083 aluminium alloy is shown in figure 84. The trend highlights that the alloy exhibits a large plastic deformation before its final fracture. Three distinct regions can be identified:

- 1) As expected, at low strain value ( $< 0.6\%$ ) a linear relationship between stress and strain is observed. The material is in a fully elastic regime; the applied strain is still totally recoverable.
- 2) At increasing strain value, a progressive deviation from the linear trend takes place. In particular, in correspondence at a strain equal to  $0.6\%$  (related stress equal to 169.5 MPa), the presence of a knee can be recognized. This point can be identified as a threshold value beyond which an elastic-plastic deformation occurs. This region can be considered stable until a  $\epsilon=6\%$
- 3) Above  $\epsilon=6\%$  a significant increase in curve fluctuations can be observed. This behaviour can be attributed to the increasingly significant necking

## Experimental results

phenomenon. A reduction of the cross section of a dog-bon gauge occurs due to the tensile strain. It manifests the triggering of a marked plastic regime. The slope of the curve gradually decreases, confirming the progressive thinning of the cross-section, until the failure at  $\varepsilon=27.1$  % is reached.

In order to correlate the surface properties modification of the silane coating and the sample deformation, several tensile tests stopped at increasing strains were conducted in order to have samples with strain conditions related to the different regimes found in the stress-strain curve.

The markers located in figure 84 identify these samples. The points were selected in order to identify some representative points of the characteristic curve of the aluminium alloy. In particular:

- P1 is located at  $\varepsilon=0.3$  % and  $\sigma=131$  MPa. It is in the linear region of the stress-strain curve and it identifies the elastic regime;
- P2 is located at  $\varepsilon=0.6$  % and  $\sigma=170$  MPa. It is placed in correspondence of the transition knee toward non-linear behaviour of the curve. It was related to yield strain of the alloy;
- P4 is located at  $\varepsilon=15.0$  % and  $\sigma=333$  MPa. It is located in the markedly plastic regime;
- finally, P5 is referred to sample fracture. It occurred at  $\varepsilon=27.1$  % and  $\sigma=338$  MPa.

For each step, sessile drop tests were performed in as received and tooled surface to evaluate WCA, identified as possible discriminating parameter concerning the superficial coating degradation due to mechanical stress. This approach allows having a useful overview of the coating stability during real service life conditions. Even though a mechanical component generally works under yield point, local high stresses due to working conditions can happen. That is a crucial improvement of knowledge in order to know if the coating can maintain its hydrophobic property also

## Experimental results

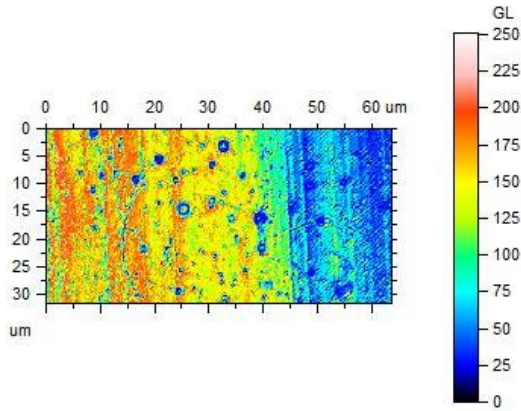
in this critical scenario. The surface characterization at varying strain level can provide the required information to overcome this issue.

Preliminarily, topographic maps of the coated surface were carried out on each specimen by means a co-focal optical microscopy. The comparison for the topological maps for specimens P1 (elastic regime) and P4 (plastic regime), chosen as reference, is reported in figure 85.

The maps exhibit an almost similar morphology. All samples are characterized by some micro-hemispherical voids randomly located in the whole surface. The diameter of these cavities varies in the range 3-15  $\mu\text{m}$ .

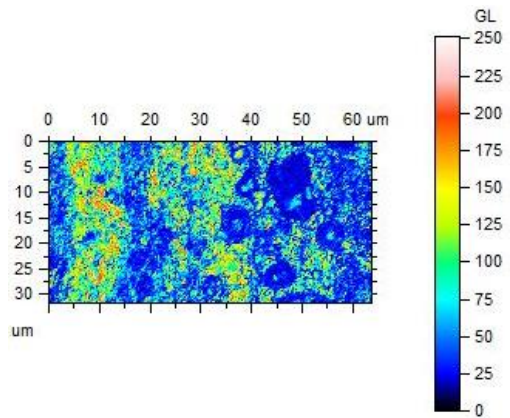
Their origin can be related to the silane coating synthesis process. The hydrophobic protective film was obtained by dip-coating deposition of an ethanol-based silane solution. During the cure process the crosslinking of the silane film took place. At the same time during the early stages of the cure, evaporation of the ethanol occurs. This led to the formation of ethanol in the vapour state which induced the formation of a surface pattern with random hemispherical cavities [58] [59]. If required, in order to avoid this issue, a possible approach could be to apply a soft thermal treatment setting a lower curing temperature, but longer curing time [60] [61].

# Experimental results



ISO 25178		
Height Parameters		
Sq	0.742616	um
Ssk	0.219246	
Sku	1.49761	
Sp	1.44690	um
Sv	1.07380	um
Sz	2.52070	um
<b>Sa</b>	<b>0.680978</b>	<b>um</b>

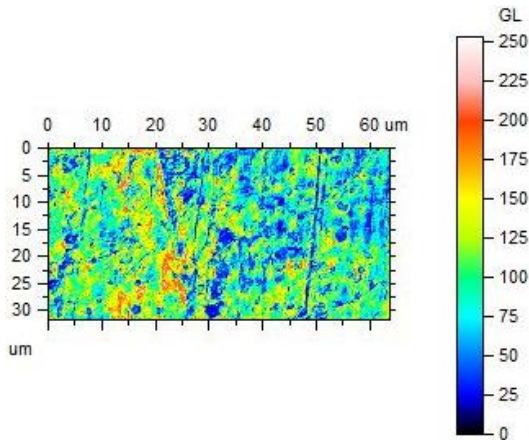
(a)



ISO 25178		
Height Parameters		
Sq	0.913449	um
Ssk	-0.14105	
Sku	1.53481	
Sp	2.05396	um
Sv	1.80299	um
Sz	3.85695	um
<b>Sa</b>	<b>0.824689</b>	<b>um</b>

(b)

## Experimental results



ISO 25178		
Height Parameters		
Sq	1.46280	um
Ssk	-0.416159	
Sku	1.57650	
Sp	2.62911	um
Sv	2.86299	um
Sz	5.49209	um
<b>Sa</b>	<b>1.33473</b>	<b>um</b>

(c)

Figure 85 Confocal microscopy analysis for the A-WS batch: a) not mechanically stressed; b) P1 point sample c) P4 point sample

By analysing the topographies in Figure 85, roughness values were calculated. It was observed that for the same specimen, the roughness becomes twice the initial value at a strain of 15%. It is worth mentioning that the kurtosis remains almost the same value; while an important reduction of skewness is measured, indicating that the surface is characterized by surface micro-cracks that increases with the strain.

The similar morphology, with no relevant discrepancies, observed for all batches clarifies that no superficial macro-defect was originated due mechanical stress. Although, analysing the profiles in more detail, there is a slight increase in roughness, Sa, probably associated with the formation of surface micro-cracks on the silane coating. This contribution becomes sensitive only for the specimen P4,

## Experimental results

deformed until the fully plastic regime is reached. The coating damaging could depress the droplet shape leading to a progressive decrease in the surface hydrophobicity. However, due to the limited resolution of the confocal analysis technique, this discrimination cannot be effectively addressed in order to assess the stress induced degradation of the surface. In order to corroborate these considerations, SEM images of P4 sample (on the tooled side) are reported in figure 86.

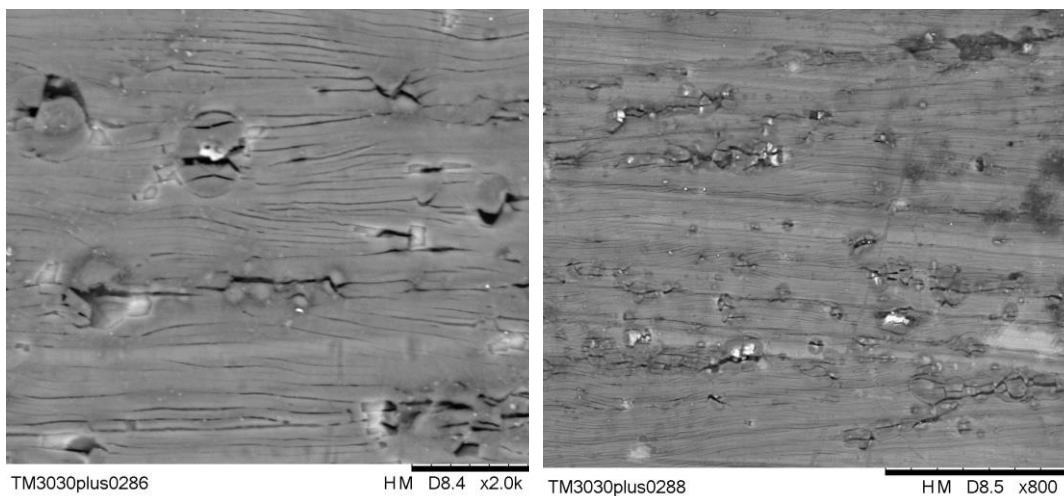


*Figure 86 SEM micrographs of A-WS-P4 sample a) at 2000 x of magnitude b) at 800 x*

To confirm the deterioration of the coating due to tensile stress, the SEM-EDS analysis was shown in figure 86 for P1 and P4 point in A-WS samples, as reference. The surface morphology exhibits several crack rivers due to the induced strain in the gauge length. These cracks are deep as confirmed by EDS line scan analysis (red lines in figure 87) performed on fluorine marker. When the fluoro-alkyl silane film is not damaged the marker index is high, despite in correspondence of the local fractures this index has an abrupt decrease indicating a local detachment/disbanding of the silane layer. In particular, in P4 (figure 87b) a larger and deeper amount of cracks (transversal to the load direction) than in P1 one were observed.

## Experimental results

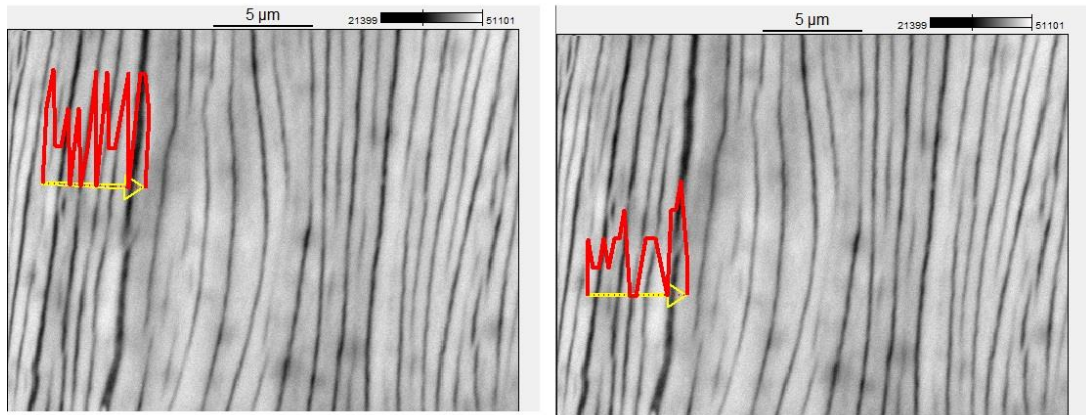


*Figure 87 SEM-EDS of A-WS sample a) elastic regime (P1) b) plastic regime (P4). In red the EDS line scan on fluorine marker.*

This behaviour is critically extended evaluating the silane film degradation on the fracture sample (P5).

In Figure 88 compares the fracture surface at top of the gauge length and in correspondence of the fracture area for the A-WS-P5 sample. The micrographs show cracks on the whole coated surface due to the large deformation applied during the tensile test until the sample fracture.

The surface located on the upper side of the gauge length was affected in a limited way by the applied deformation. Thin and sporadically distributed cracks are visible on the surface. Conversely, the region near the fracture suffered a relevant surface degradation due to a wide necking phenomenon. Consequently, high levels of interlaminar stress have taken place at the coating-metal interface. These favoured the formation of a large number of cracks oriented transversely to the load direction. In particular, far away from the fracture zone of the sample, the cracks have a width of about 2.35  $\mu\text{m}$  (Figure 88a). On the other hand, close to the fracture surface (Figure 88b) there is a considerable increase of cracks with subsequent reduction of the crack width distance (about 0.6 microns).

## Experimental results

Furthermore, large debonded area can be observed. Silane coating was locally detached from the substrate and bare aluminium alloy was exposed and no longer protected by the hydrophobic film.

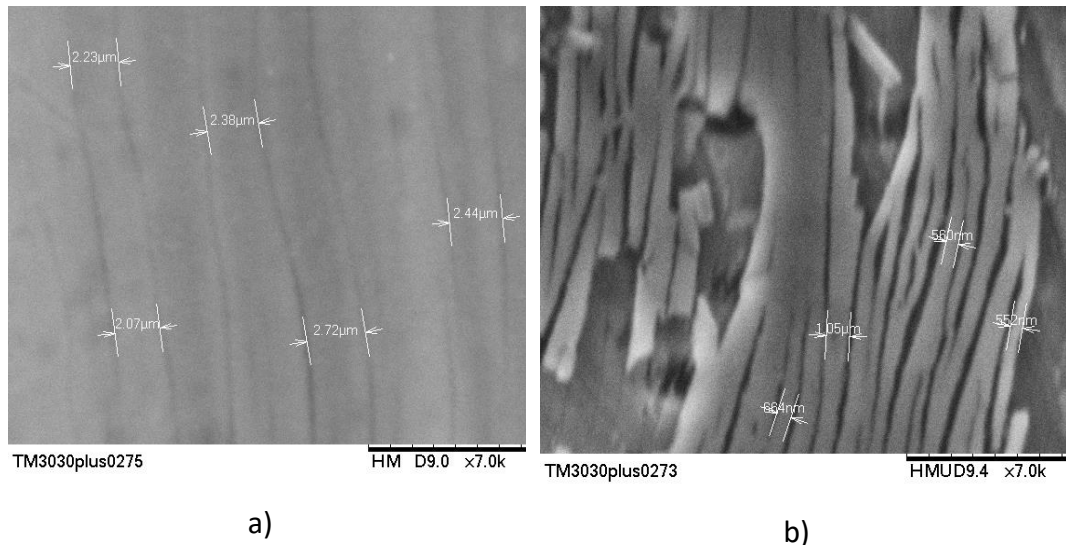


*Figure 88 SEM micrographs on the top of the gauge length a) and on the fracture surface-b) for A-WS-P5 sample*

The morphological surface study, carried out on the specimens at varying strain values, has shown evident degradation phenomena on the superhydrophobic silane coating. The triggering of cracks has already taken place at low deformation levels (P1) and has gradually extended with the increase of the strain (P4) up to entail extensive debonding phenomena near the fracture (P5).

The surface morphological study, carried out on the specimens when the deformation imposed changes, has shown the formation of local damages on the superhydrophobic silane coating. The activation of cracks has already taken place at low deformation levels (P1) and has gradually extended with the increase of the strain (P4) up to entail debonding phenomenon near the fracture (P5).

## Experimental results

A fundamental aspect that must be ascertained is to evaluate how much and in which way local damage in the fluoro-alkyl silane coating affects the surface hydrophobic properties of the samples. On this concern, in order to evaluate whether the hydrophobic properties of the silane coating are preserved even after the mechanical stress cycle contact angle measurements along the gauge length were performed for P1-P5 strain point.

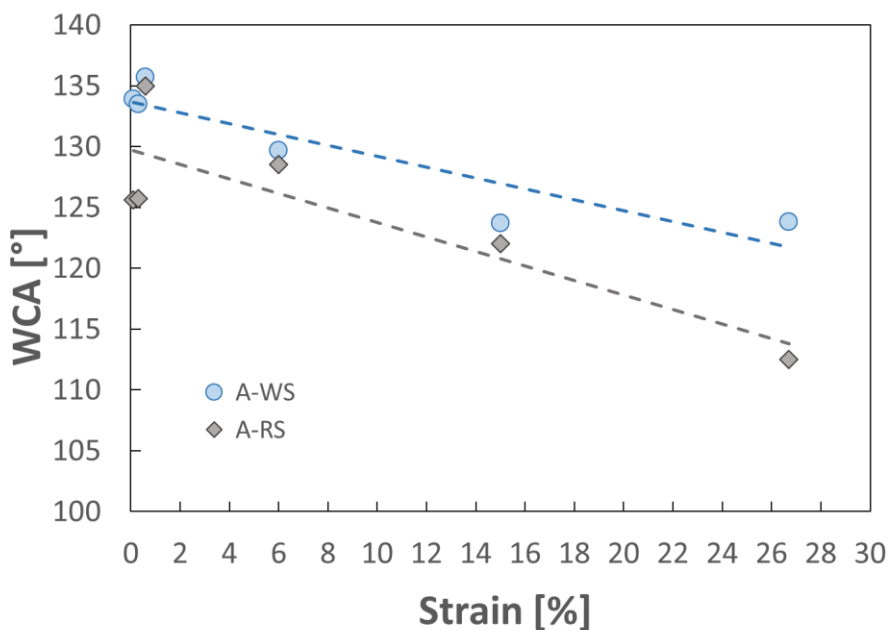


*Figure 89 Evolution of the contact angle at increasing strain level*

Figure 89 shows the average water contact angle (WCA) at varying applied displacement. A clear increase of the contact angle was observed on both types of surfaces at low strain level (0.3 %). This phenomenon is probably due to the fact that the cracks observed on the coating are not deep/large enough to activate an interaction of the underlying aluminium substrate with the water, not implying a detrimental effect on wettability behaviour. The slight increase observed in WCA

## Experimental results

could be ascribed, instead, to the increase in surface micro-roughness induced by the formation of non-passing surface cracks. This, according to Wenzel's theory, involves an increase in the contact angle for the hydrophobic fluorosilane coating. At increasing strain values, the curve trend highlights a progressive decrease in the contact angle, cause of a gradual and relevant coating damaging phenomena. The WCA reduction is more accentuated for A-RS sample where a maximum reduction of about 11% can be observed (from  $125.7^\circ$  to  $112.5^\circ$  for  $\varepsilon=0.0\%$  and  $\varepsilon=27.1\%$ , respectively). Instead A-WS showed a reduction of 8.6% at  $\varepsilon=15$  and 8.6% at  $\varepsilon=27.1$ . This difference in the WCA variation could be due to the mechanical processing carried out on the substrate, which allowed a better adhesion of the fluoro-alkyl silane coating on the aluminum and therefore allowed to maintain a greater WCA when the specimen is subjected to mechanical load.

A sort of plateau can be revealed for the tooled specimens at very high strains. This behaviour can be attributed to the regularity on the surface reached also for the striations due to the tensile load. At low magnitude (see figure 86b,) it can be highlight that also the striations have the same shape of the waviness surface due to the tooling, giving a sort of zig-zag path.

## Conclusion

The second and final part of the PhD thesis concerned the study of nano-structured coatings to be applied in the hydraulic field to increase the efficiency of axial piston pumps and motors.

As for the texture, the results are very promising. By using a low economic impact technique such as surface laser texturing it is possible to decrease the friction coefficient of a surface, and at the same time increase the oleophobicity and therefore improve lubrication especially in starved lubrication conditions. The study was carried out on a lead-bronze alloy which, thanks to the lubricating characteristics of lead, maintains a low friction coefficient. Three types of specimens were tested, varying the geometric characteristics of the dimples, i.e. diameter (class B), density (class C) and depth (class D). It has been demonstrated that by decreasing the diameter of the dimples, the CoF also decreased, as well as increasing the depth of the dimples the CoF increases. On the other hand, increasing the surface density of the dimples increases the CoF. The lowest value of the friction CoF was obtained for sample C5, with an average value equal to 0,01. The results obtained show that the friction coefficient has a low value also for the other types of specimens, which demonstrates how the alloy used has high anti-friction properties, due to the presence of lead which acts as a solid lubricant.

The future challenge is to eliminate lead from the bronze alloy, due to its toxicity, and to use the texture to keep the friction coefficient low. To do this, a future study plans to test free lead bronze samples on which the surface texture has been made.

As regards the use of coatings with characteristics of high hydrophobicity such as fluoro-alkyl silane, a criticality already demonstrated in other studies has been highlighted [50]. In particular, this type of coating has excellent ability to reduce the friction coefficient and improve lubrication, however it is a coating characterized by

## Conclusion

fragility and subjected to mechanical loads it undergoes deteriorating and losing its peculiar characteristics in a short time.

aluminium Samples with tooled and as received surfaces were tested. When the specimens were subjected to scratch test, the silanized specimen with tooled surface showed a greater reduction in WCA, due to the increased sensitivity of the machined surface to abrasion.

When the specimens were subjected to tensile load, the as received specimen showed a greater reduction in WCA, compared to the tooled one. This shows that the fluoro-alkyl silane coating when subjected to mechanical tensile tests partially maintains its hydrophobic behaviour due to the stronger anchoring to the substrate. However, the results showed that, even when the surface to be silanized has been tooled, a clear improvement in the durability of the silane coating is not obtained. This result compromises the use of these coatings in the hydraulic field.

An interesting future study can be based on the combined action of the texture and the superoleophobic coating in order to guarantee the properties of oleo-phobicity to the dimples (avoiding the trap effect on the oil), and guaranteeing greater durability to the superoleophobic coating which does not come into direct contact with the wearing surface.

## References

- [1] B. Carl, M. Ivantysynova, and K. Williams, “Comparison of operational characteristics in power split continuously variable transmissions,” *SAE Tech. Pap.*, no. 724, pp. 776–790, 2006.
- [2] A. MacOr and A. Rossetti, “Optimization of hydro-mechanical power split transmissions,” *Mech. Mach. Theory*, vol. 46, no. 12, pp. 1901–1919, 2011.
- [3] S. S. Volpe, G. Carbone, M. Napolitano, and E. Sedoni, “Design optimization of input and output coupled power split infinitely variable transmissions,” *J. Mech. Des. Trans. ASME*, vol. 131, no. 11, pp. 1110021–11100211, 2009.
- [4] S. Ahn, J. Choi, S. Kim, J. Lee, C. Choi, and H. Kim, “Development of an integrated engine-hydro-mechanical transmission control algorithm for a tractor,” *Adv. Mech. Eng.*, vol. 7, no. 7, pp. 1–18, 2015.
- [5] J. H. Kress, “Vehicles — Classification and Theory of Operation,” pp. 2282–2306, 2015.
- [6] “Comparison between Input Coupled and Output Coupled Power-split Configurations in Hybrid Vehicles,” *IFPE Conf. Proc.*, pp. 243–252, 2011.
- [7] A. Rossetti and A. MacOr, “Multi-objective optimization of hydro-mechanical power split transmissions,” *Mech. Mach. Theory*, vol. 62, pp. 112–128, 2013.
- [8] R. Kumar, M. Ivantysynova, and K. Williams, “Study of energetic characteristics in power split drives for on highway trucks and wheel loaders,” *SAE Tech. Pap.*, no. 724, 2007.
- [9] “[https://www.meccanicanews.com/2016/12/02/trasmissioni-idrostatiche/-/](https://www.meccanicanews.com/2016/12/02/trasmissioni-idrostatiche/)”
- [10] M. Martelli and L. G. Zarotti, “Hydrostatic transmission with a traction control,” *22nd Int. Symp. Autom. Robot. Constr. ISARC 2005*, 2005.
- [11] J. Ivantysyn and M. Ivantysynova, *Hydrostatic pumps and motors:*

## References

- principles, design, performance, modelling, analysis, control and testing.*  
Tech Books International, 2003.
- [12] M. F. Gao and J. Bin Hu, “Kinematic Analysis of Planetary Gear Trains Based on Topology,” *J. Mech. Des. Trans. ASME*, vol. 140, no. 1, 2018.
- [13] M. Scamperle, “Sviluppo di un modello previsionale del rumore di unitÃ CVT idrauliche ed applicazione al caso di una trasmissione idromeccanica dual-stage per autobus urbano,” 2013.
- [14] G. Costa and N. Sepehri, *Hydrostatic transmissions and actuators: operation, modelling and applications.* John Wiley & Sons, 2015.
- [15] F. Liu, W. Wu, J. Hu, and S. Yuan, “Design of multi-range hydro-mechanical transmission using modular method,” *Mech. Syst. Signal Process.*, vol. 126, pp. 1–20, 2019.
- [16] S. I. Mistry and G. E. Sparks, “Infinitely Variable Transmission ( IVT ) of John Deere 7000 TEN Series Tractors Dr . Sanjay I . Mistry and Gregory E . Sparks , P . E . Electro-Hydraulic Control Systems John Deere Product Engineering Center Waterloo , Iowa 50704,” 2016.
- [17] D. Haensel, P. E. D. Herrmann, U. Blumenthal, and U. Luning, “United States Patent (19),” no. 19, 1991.
- [18] K. Pettersson and P. Krus, “Design optimization of complex hydromechanical transmissions,” *J. Mech. Des. Trans. ASME*, vol. 135, no. 9, pp. 1–9, 2013.
- [19] L. V. Larsson, “FPMC2015-9583 MODE SHIFTING IN HYBRID HYDROMECHANICAL TRANSMISSIONS,” pp. 1–13, 2016.
- [20] M. A. Hannan, F. A. Azidin, and A. Mohamed, “Hybrid electric vehicles and their challenges: A review,” *Renew. Sustain. Energy Rev.*, vol. 29, pp. 135–150, 2014.
- [21] L. Pugi, M. Pagliai, A. Nocentini, G. Lutzemberger, and A. Pretto, “Design of a hydraulic servo-actuation fed by a regenerative braking system,” *Appl.*

## References

- Energy*, vol. 187, pp. 96–115, 2017.
- [22] B. Surampudi, A. Nedungadi, G. Ostrowski, A. Montemayor, and H. Gruenewald, “Design and control considerations for a series heavy duty hybrid hydraulic vehicle,” *SAE Tech. Pap.*, vol. 4970, 2009.
- [23] T. Lin, Q. Wang, B. Hu, and W. Gong, “Research on the energy regeneration systems for hybrid hydraulic excavators,” *Autom. Constr.*, vol. 19, no. 8, pp. 1016–1026, 2010.
- [24] J. Gong *et al.*, “Power control strategy and performance evaluation of a novel electro-hydraulic energy-saving system,” *Appl. Energy*, vol. 233–234, no. September 2018, pp. 724–734, 2019.
- [25] B. Fahimi, A. Emadi, and R. B. Sepe, “A switched reluctance machine-based starter/alternator for more electric cars,” *IEEE Trans. Energy Convers.*, vol. 19, no. 1, pp. 116–124, 2004.
- [26] M. S. H. Hänninen, M. S. J. Juhala, J. Kajaste, and M. Pietola, “Hydraulic Energy Recovery System Utilizing a Thermally Regenerative Hydraulic Accumulator Implemented to a Reach Truck,” 2016.
- [27] S. Wicki and E. G. Hansen, “Clean energy storage technology in the making: An innovation systems perspective on flywheel energy storage,” *J. Clean. Prod.*, vol. 162, pp. 1118–1134, 2017.
- [28] P. Banerjee and M. Ivantysynova, “Development of a Torque-Based Control Strategy for a Mode-Switching Hydraulic Hybrid Passenger Vehicle,” *SAE Tech. Pap.*, vol. 2018-April, pp. 1–14, 2018.
- [29] A. Krauss and M. Ivantysynova, “Power split transmissions versus hydrostatic multiple motor concepts - A comparative analysis,” *SAE Tech. Pap.*, no. 724, 2004.
- [30] I. Monika, M. Ivantysynova, I. N. Us, B. A. Carl, M. I. Us, and K. Richard, “(19) United States (12),” vol. 1, no. 19, 2008.
- [31] J. ZHANG, Q. CHAO, and B. XU, “Analysis of the cylinder block tilting

## References

- inertia moment and its effect on the performance of high-speed electro-hydrostatic actuator pumps of aircraft,” *Chinese J. Aeronaut.*, vol. 31, no. 1, pp. 169–177, 2018.
- [32] Y.-S. Hong, S.-Y. Lee, S.-H. Kim, and H.-S. Lim, “Improvement of the low-speed friction characteristics of a hydraulic piston pump by PVD-coating of TiN,” *J. Mech. Sci. Technol.*, vol. 20, no. 3, pp. 358–365, 2006.
- [33] A. M. Korsunsky, A. R. Torosyan, and K. Kim, “Development and characterization of low friction coatings for protection against fretting wear in aerospace components,” *Thin Solid Films*, vol. 516, no. 16, pp. 5690–5699, 2008.
- [34] M. Raimondo, F. Veronesi, G. Boveri, G. Guarini, A. Motta, and R. Zanoni, “Superhydrophobic properties induced by sol-gel routes on copper surfaces,” *Appl. Surf. Sci.*, vol. 422, pp. 1022–1029, 2017.
- [35] J. Thomson, R. Zavadil, M. Sahoo, A. Dadouche, W. Dmochowski, and M. Conlon, “Development of a lead-free bearing material for aerospace applications,” *Int. J. Met.*, vol. 4, no. 1, pp. 19–30, 2010.
- [36] D. D’Andrea, G. Epasto, A. Bonanno, E. Guglielmino, and G. Benazzi, “Failure analysis of anti-friction coating for cylinder blocks in axial piston pumps,” *Eng. Fail. Anal.*, vol. 104, pp. 126–138, 2019.
- [37] M. Kallio *et al.*, “Tribological Behavior of Bronze Alloys with Solid Lubricants,” *Key Eng. Mater.*, vol. 527, pp. 205–210, Nov. 2012.
- [38] W. Grabon, W. Koszela, P. Pawlus, and S. Ochwat, “Improving tribological behaviour of piston ring-cylinder liner frictional pair by liner surface texturing,” *Tribol. Int.*, vol. 61, pp. 102–108, 2013.
- [39] P. Achten, “Dynamic high-frequency behaviour of the swash plate in a variable displacement axial piston pump,” *Proc. Inst. Mech. Eng. Part I J. Syst. Control Eng.*, vol. 227, no. 6, pp. 529–540, 2013.
- [40] S. L. Nie, G. H. Huang, and Y. P. Li, “Tribological study on hydrostatic

## References

- slipper bearing with annular orifice damper for water hydraulic axial piston motor,” *Tribol. Int.*, vol. 39, no. 11, pp. 1342–1354, 2006.
- [41] D. Hast, R. Findeisen, and S. Streif, “Detection and isolation of parametric faults in hydraulic pumps using a set-based approach and quantitative-qualitative fault specifications,” *Control Eng. Pract.*, vol. 40, pp. 61–70, 2015.
- [42] J. Ou, W. Hu, S. Liu, M. Xue, F. Wang, and W. Li, “Superoleophobic textured copper surfaces fabricated by chemical etching/oxidation and surface fluorination,” *ACS Appl. Mater. Interfaces*, vol. 5, no. 20, pp. 10035–10041, 2013.
- [43] Y. S. Hong and Y. H. Doh, “Analysis on the friction losses of a bent-axis type hydraulic piston pump,” *KSME Int. J.*, vol. 18, no. 9, pp. 1668–1679, 2004.
- [44] U. Pettersson and S. Jacobson, “Textured surfaces for improved lubrication at high pressure and low sliding speed of roller/piston in hydraulic motors,” *Tribol. Int.*, vol. 40, no. 2 SPEC. ISS., pp. 355–359, 2007.
- [45] A. Kovalchenko, O. Ajayi, A. Erdemir, G. Fenske, and I. Etsion, “The effect of laser texturing of steel surfaces and speed-load parameters on the transition of lubrication regime from boundary to hydrodynamic,” *Tribol. Trans.*, vol. 47, no. 2, pp. 299–307, 2004.
- [46] E. Lotus, “Superfici Nanostrutturate e Nanotribologia,” pp. 1–12, 2013.
- [47] A. V. Rao, S. S. Lathe, S. A. Mahadik, and C. Kappenstein, “Mechanically stable and corrosion resistant superhydrophobic sol-gel coatings on copper substrate,” *Appl. Surf. Sci.*, vol. 257, no. 13, pp. 5772–5776, 2011.
- [48] M. Raimondo, M. Blosi, A. Caldarelli, G. Guarini, and F. Veronesi, “Wetting behavior and remarkable durability of amphiphobic aluminum alloys surfaces in a wide range of environmental conditions,” *Chem. Eng. J.*, vol. 258, pp. 101–109, 2014.

## References

- [49] R. G. C. da Silva, M. R. S. Vieira, M. I. C. Malta, C. H. da Silva, S. H. de Oliveira, and S. L. U. Filho, "Effect of initial surface treatment on obtaining a superhydrophobic surface on 5052 aluminum alloy with enhanced anticorrosion properties," *Surf. Coatings Technol.*, vol. 369, no. September 2018, pp. 311–322, 2019.
- [50] G. Rizzo *et al.*, "Axial piston pumps slippers with nanocoated surfaces to reduce friction," *Int. J. Fluid Power*, vol. 16, no. 1, pp. 1–10, 2015.
- [51] R. Sun, J. Zhao, Z. Li, J. Mo, Y. Pan, and D. Luo, "Preparation of mechanically durable superhydrophobic aluminum surface by sandblasting and chemical modification," *Prog. Org. Coatings*, vol. 133, no. April, pp. 77–84, 2019.
- [52] X. Zhang, D. Zhi, W. Zhu, S. Sathasivam, and I. P. Parkin, "Facile fabrication of durable superhydrophobic SiO<sub>2</sub>/polyurethane composite sponge for continuous separation of oil from water," *RSC Adv.*, vol. 7, no. 19, pp. 11362–11366, 2017.
- [53] V. A. C. Haanappel, H. D. van Corbach, T. Fransen, and P. J. Gellings, "Cracking and delamination of metal organic vapour and deposited alumina and silica films," *Mater. Sci. Eng. A*, vol. 167, no. 1–2, pp. 179–185, 1993.
- [54] P. W. Shum, Z. F. Zhou, and K. Y. Li, "Investigation of the tribological properties of the different textured DLC coatings under reciprocating lubricated conditions," *Tribol. Int.*, vol. 65, pp. 259–264, 2013.
- [55] L. Calabrese, A. Khaskhoussi, S. Patane, and E. Proverbio, "Assessment of Super-Hydrophobic Textured Coatings on AA6082 Aluminum Alloy," *Coatings*, vol. 9, no. 6, p. 352, May 2019.
- [56] L. Wu, X. Guo, and J. Zhang, "Abrasive resistant coatings - A review," *Lubricants*, vol. 2, no. 2, pp. 66–89, 2014.
- [57] B. Przybyszewski *et al.*, "Hydrophobic and Icephobic Behaviour of Polyurethane-Based Nanocomposite Coatings," *Coatings*, vol. 9, no. 811,

## References

- pp. 1–12, 2019.
- [58] H. Uchiyama, “Evaporation-driven self-organization of sol-gel dip-coating films,” *J. Ceram. Soc. Japan*, vol. 123, no. 1438, pp. 457–464, 2015.
- [59] G. Gong, J. Wang, H. Nagasawa, M. Kanezashi, T. Yoshioka, and T. Tsuru, “Sol-gel spin coating process to fabricate a new type of uniform and thin organosilica coating on polysulfone film,” *Mater. Lett.*, vol. 109, pp. 130–133, 2013.
- [60] L. Calabrese *et al.*, “Development and characterization of silane-zeolite adsorbent coatings for adsorption heat pump applications,” *Appl. Therm. Eng.*, vol. 116, pp. 364–371, 2017.
- [61] L. Calabrese, L. Bonaccorsi, A. Capri, and E. Proverbio, “Effect of silane matrix composition on performances of zeolite composite coatings,” *Prog. Org. Coatings*, vol. 101, pp. 100–110, 2016.